Compressive Behavior of Kinking Nonlinear Elastic Solids

- Ti_3SiC_2, Graphite, Mica and BN

A Thesis

Submitted to the Faculty

Of

Drexel University

By

Tiejun Zhen

in partial fulfillment of the

requirements for the degree

of

Doctor of Philosophy

April 2004

Dedication

To my parents who always believed that I could achieve everything I wished for.

Thank you.

.

Acknowledgments

The author expresses his heartfelt gratitude to his advisor **Dr. Michel Barsoum** for his help, strong support, encouragement, and enthusiasm related to my work, great teaching, friendly advice and his faith in me. Thus, I can simply say: **THANK YOU**.

I consider myself lucky and honored for having an opportunity to collaborate with a lot of wonderful people during my work on PhD Thesis. Among all of them, I would like specially to tanks:

- **Dr. Surya Kalidindi**, Drexel University, for helping me to interpret experimental results, inspiriting discussions, great suggestions and for his time and interest in reviewing this thesis and participating in my defense committee;
- **Dr. Yury Gogosi and Dr. Roger Doherty**, Drexel University, for their time and interest in reviewing this thesis and participating in my defense committee;
- **Dr. Miladin Rodovic,** from Oak Ridge National laboratory, Oak Ridge, TN for helping me to interpret experimental results, inspiriting discussions, great suggestions and interest in reviewing this thesis and participating in my defense committee;
- **Mr. David Von Rohr** from Drexel University, for his great help with microscopy
- **Mr. Mark Shiber** from Drexel University, for doing the great job in machining the testing samples:
- **Mrs. Judy Trechtman**, **Mrs. Dorilona Rose and Mrs. Artheis Staten** from Drexel University, for their great help in solving everyday problems, friendly advice and support;

- All **Faculty members of the Materials Engineering Department**, Drexel University;
- My fellow **graduate students in the Materials Engineering Department** at Drexel University for making this work an enjoyable and unforgettable experience. Sincere thanks are due to **Mr. Ganguly and Mr. Gupta** for their help to allow me to use their samples.

Finally, I would like to thank my parents **Shude Zhen** and **Shihua Li** and my brother **Lijun Zhen**, for their comprehension, help and unselfish support. Without their help, this work would not have been possible.

Philadelphia Tiejun Zhen

April 25, 2004

Table of Contents

List of Tables

List of Figures

Abstract

Compressive behavior of kinking nonlinear elastic solids
-Ti_3SiC_2, graphite, mica and BN

Tiejun Zhen
Michel Barsoum, Ph.D.
Surya Kalidindi, Ph.D.

Dislocation-based deformation in crystalline solids is almost always plastic. Once dislocations are generated they entangle and render the process irreversible. In our recent work we show that this does not apply to a new class of materials, best characterized as kinking nonlinear elastic (KNE) solids. KNE solids include the MAX phases, mica, graphite, boron nitride, so called nonlinear mesoscopic elastic (NME) solids discussed in geological literature and most probably ice. The MAX phases are a new class of layered machinable ternary carbides and nitrides, with the chemical formula $M_{n+1}AX_n$, where M is an early transition metal, A is an A-group element (mostly IIIA and IVA) and X is C or N.

The compressive loading-unloading stress-strain curves of KNE solids in the elastic regime outline nonlinear, fully reversible, reproducible, rate-independent, closed hysteresis loops whose shape and extent of energy dissipated are strongly influenced by grain size with the energy dissipated being significantly larger in the coarse-grained material. This unique property is attributed to the formation and annihilation of incipient kink bands (IKBs), defined to be thin plates of sheared material bounded by opposite walls of dislocations. As long as the dislocation walls remain attached, the response is fully reversible. Furthermore, because the

dislocations are confined to the basal planes work hardening does not occur and the dislocations can move reversibly over relatively large distances. This kind of dislocation motion renders KNE solids potentially high damping material. The loss factor for Ti_3SiC_2, a prime member of KNE solids, is higher than most woods, and comparable to polypropylene and nylon.

At higher temperatures or stress, since the IKB dissociate and coalesce to form regular irreversible kink bands. The close hystesis loops are open, the response is strain-rate dependent, and cyclic hardening is observed even at 1200 ^{o}C

1. Introduction

In general when a solid is subjected to a stress below its elastic limit, it deforms elastically; the strain is proportional to stress and disappears when the stress is removed. This property was first proposed by Hooke in the 17th century and is now well known as Hooke's law. However Coulomb at the end of 18th century and then Weber at the beginning of 19th century noticed that deformation is not instantaneous when stress is applied, but depends on time. The time-dependent deformation was termed anelastic deformation. This behavior occurs in all materials, but in general the strain which depended on time is not very significant, so that, to a first approximation, most solids can be considered to be linear elastic. However, depending upon microstructure, temperature, stress, time, etc., some materials can present a significant anelastic deformation.

Anelastic phenomena are important factors in fatigue and fracture behavior. A materials' ability to absorb, and thus not transmit vibration, or noise, is related to its damping capacity. Mechanical vibrations in engineering structures can create severe problems. Thus the ramifications of developing high damping materials will not be inconsequential in applications and fields as diverse as precision machine tools, quiet, vibration free machinery and transportation equipment, industrial robots, the performance of electronic and MEMS devices, the wobble of disc drives or low density armor, among others.

In a sense the damping has been observed by everyone who has measured the stress-strain curves of graphite which exhibit the well-known hysteresis loops. Early studies of the hysteresis behavior of graphite were made by Curry et al [1] in 1955 and Davidson et al [2] in 1958. Figure 1 shows such kind of hysteresis loops of stress-strain curves in tension and compression reported by Losty and Orchard [3]. Similar behavior was also reported on so called nonlinear mesoscopic elastic (NME) solids discussed in the geological literature [4-9] and Ti_3SiC_2 in tensile tests [10]. However, they were never linked and the hystersis mechanism remained elusive.

In our recent work [11-14], we have encountered a new class of materials that exhibit extensive slip, but on a limited number of easy glide slip systems. This new class of material, including the MAX phases, mica, graphite, boron nitride, NME solids and most probably ice, can be classified as kinking nonlinear elastic (KNE) solids. The MAX phases are a new class of layered machinable ternary carbides and nitrides, with the chemical formula $M_{n+1}AX_n$, where M is an early transition metal, A is an A-group element (mostly IIIA and IVA) and X is C or N. Ti_3SiC_2 is a prime example of the MAX phases, and its properties have been extensively studied by our group [10-12, 32-41]. We prefer to label this class of solids as KNE solids to emphasize the fact that kinking, a mechanism reported first by Orowan in single crystals of Cd loaded parallel to the basal planes [15], is the physical origin of the hysteretic, nonlinear elastic, behavior exhibited by these solids.

In the following part a brief review of what was known of the mechanical properties of graphite, NME solids and Ti_3SiC_2, three typical KNE solids, will be presented and the author believes this will be helpful for the reader to understand this work.

1.1 Background

1.1.1 Graphite

The normal structure of graphite is hexagonal with c/a ≈ 2.73 (c = 6.708 Å and a = 2.456 Å). Graphite is a technologically important material that has been intensely studied for over 100 years [16]. Elastically, thermally and plastically, graphite is a strongly anisotropic solid; an anisotropy that stems from the very strong covalent bonding within the basal planes, and the weak Van der Waals forces between them. At 1060 GPa, the elastic modulus along the basal planes (c_{11}) is one of the highest known. In contrast, at 36.5 GPa, the modulus along the c-axis (c_{33}) is significantly lower.

It is well known that basal plane in graphite is the principal shear plane [16]. Freise and Kelly [17] reported that the only mode of deformation of graphite single crystals at room temperature is by the motion of dislocation in the basal plane. It is

well-established that these dislocations can form tilt or twist boundaries. And this kind of boundary is essentially composed by dislocations on different slip plane [17].

It is also well-known that the critical resolved shear stress of the basal dislocation is exceedingly low [16]. Thus the classical elastic theory is only strictly true in polycrystalline graphite for very small strains, since the apparent elastic constants are strain dependent. The theory of the effect of dislocation on the elastic moduli has been considered by many workers beginning with Eshelby [18], Friedel [19] and Mott [20], but they are too simple to be completely satisfactory. Also a number of authors have noted that pre-stressing alters the Young's modulus measured at small strains [16].

As for the stress-strain response of polycrystalline carbons and graphites, increasing the perfection of the material make stress-strain curves become increasingly non-linear. The initial stress-strain relationship is not reversible; a permanent set is observed which increases with stress (Fig. 1). Cyclic loading produces hysteresis loops in both tensile and compressive tests (Fig. 1). The hysteresis increases with the degree of perfection of the graphite [16].

Kelly [21] and Reynolds [22] suggested that studies of the damping could lead to an increased understanding of the mechanisms involved in the mechanical properties of graphite. The experimental data on the damping of polycrystalline graphites is fairly well-established. The more perfect the materials, the higher the

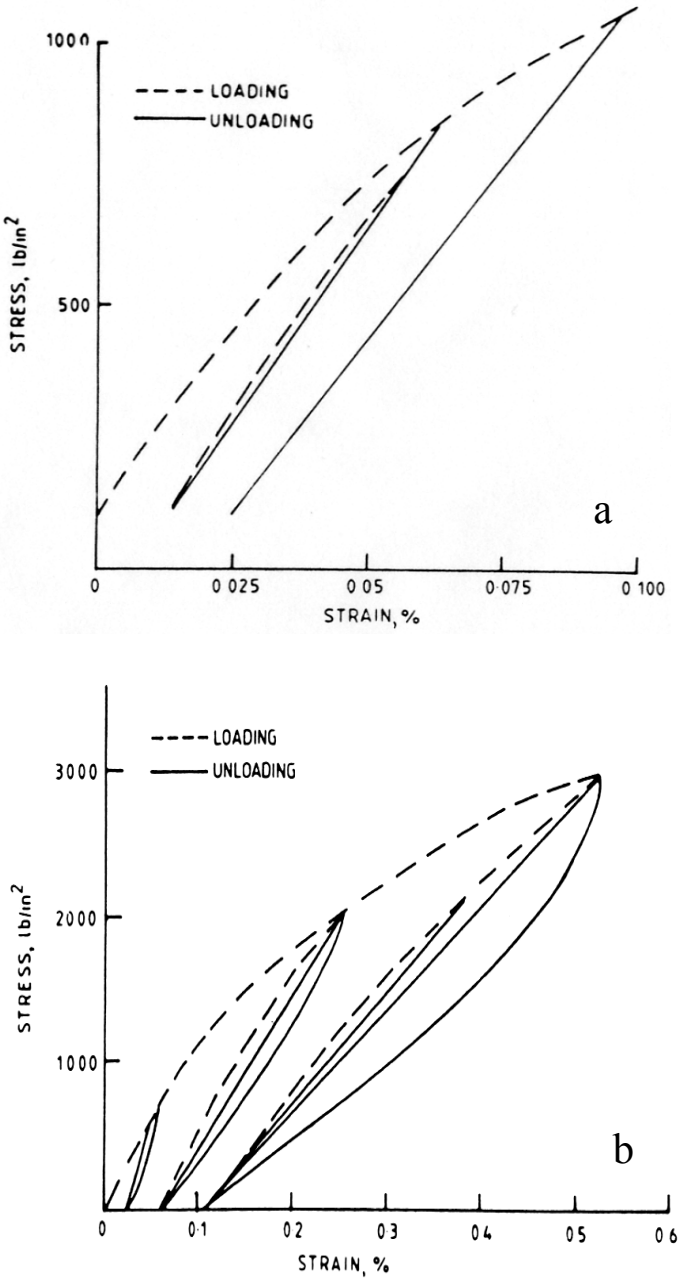

Fig. 1 Stress-strain diagrams for graphite. a). Tension. b). Compression [3].

damping. This indicates the source of damping is from material itself not from the impurity of the materials. The damping is also strain and stress amplitude dependent. The modulus showed the inverse behavior, falling as the damping increased. There is wide agreement that the damping is due to dislocation processes. However, as in the case of the dislocation effects on the Young's modulus of well graphitized samples, the magnitudes are large compared to those in metals [16].

The data for the commercial graphites and the pitch bonded natural graphite show a consistent pattern for Q^{-1}. The height of the peak is apparently related to the crystallite size and quality of the graphite [16].

A number of attempts have been made to describe the stress-strain curves of graphite, based on phenomenological models or simple theories of deformation. The observation of hysteresis loops in graphite crystals associated only with the basal shear mode have led many authors, i.e. Jenkin[23, 24], Woolley[25] and Hesketh[26], to associate the hysteresis of polycrystalline graphite with basal slip and or cracking.

However, the forms chosen were essentially empirical. In other words to date, despite roughly 100 years of study, the stress-strain curves of polycrystalline graphite are not understood.

1.1.2 Nonlinear mesoscopic elastic (NME) solids

Many materials near Earth's surface are believed to be nonlinear mesoscopic elastic (NME) solids that exhibit nonlinear elastic behavior, hysteresis and discrete memory [4-6]. Figure 2 shows a stress-strain curve with a complex loading-unloading history of Berea sandstone [4], a typical NME solid. It clearly shows the nonlinear elastic behavior, hysteresis and discrete memory behavior.

Based on reversible tensile Griffith cracks, Holcomb [6] proposed a model to explain the memory behavior shown by dilatant rock. This model can predict a variety of phenomena, many of which have observed. But a property that is not predicted is the healing which occurs when unloading is stopped and the load is held constant.

The in situ deformation of muscovite and biotite in transmission electron microscopy (TEM) showed only basal slip was activated in either micas [27]. Also it has long been established that kink bands (KBs) play an important role in the deformation of geologic materials [28-31]. However, because the response of NME solids is fully reversible and the KBs will cause permanent deformation, the two were never linked.

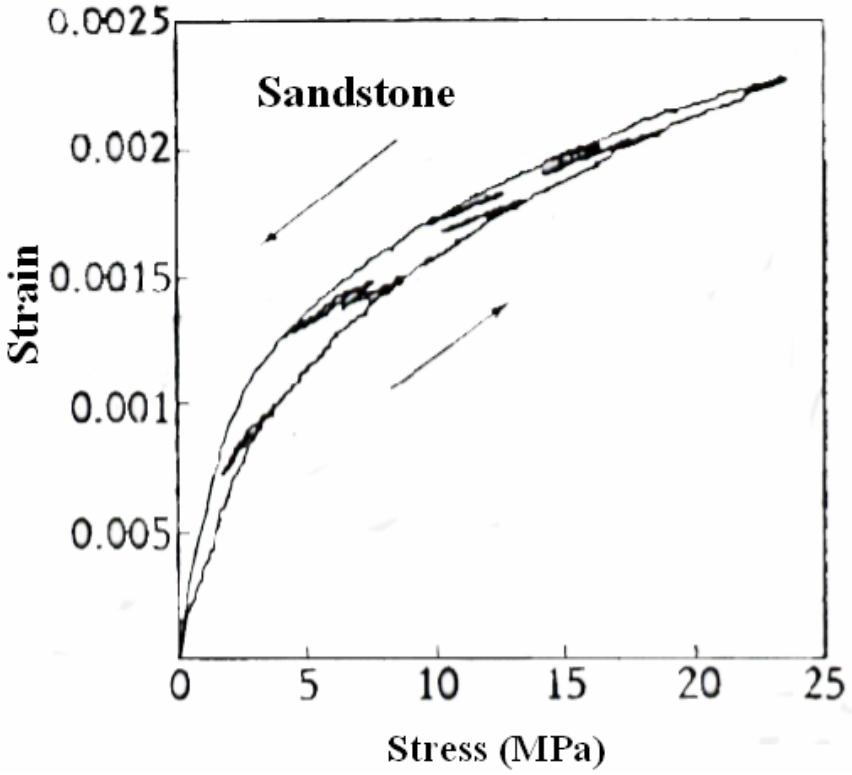

Fig. 2 The strain as a function of the applied stress for Berea sandstone [4].

Most recently Guyer [4] proposed a phenomenological model, namely the Preisach-Mayergoyz space (P-M space) model, to explain the hysteresis and memory effects shown by NME solids. But there is no real simulation results reported based on the P-M model to date. It was also suggested by Guyer that the unique feature of NME solids was due to the contacts between grains – the bond system – constitute a set of effective elastic elements that control the elastic behavior of NME solids. The grains themselves were assumed act as rigid units. However the mechanism of the hysteresis is elusive.

1.1.3 Ti_3SiC_2

Since Ti_3SiC_2 was synthesized as a fully dense, single-phase bulk material, it has been established that this ternary carbide exhibits an unusual combination of properties [32-42], such as high specific stiffness [40] with ease of machinability [34]; exceptional damage tolerance; good thermal shock resistance [34,38], as well as good oxidation [38] and fatigue resistances [32]. At room temperature, favorably oriented microstructures exhibit ductile behavior [38].

The mechanical response of Ti_3SiC_2 and by extension the other $M_{n+1}AX_n$ phases [43] (where M is a transition metal, A is an A group element and X is carbon and/or nitrogen) can be traced to the following three facts: i) Basal slip, and only

basal slip, is operative at all temperatures [36, 38]. No other dislocations but perfect, mixed basal plane dislocations are observed by TEM [35, 36, 38]. ii) Because of their high c/a ratios, twinning is unlikely, and has never been observed. Instead, deformation occurs by a combination of glide and formation of kink bands and delaminations within individual grains [35-38]. iii) Because they are confined to the basal planes, the dislocations arrange themselves either in arrays (pileups) on the same slip plane, or in walls (low or high angle grain boundaries) normal to the arrays [35,36]. Thus, at no time there are five independent slip systems required for ductility operative [44, 45].

Li et al. [46] were the first to report on the non-linear response of Ti_3SiC_2, in bending at room temperature; an observation they ascribed to a combination of microcracking and deformation. The effect was small and the hysteresis loops obtained were open. Radovic et al. [10] cycled fine-grained Ti_3SiC_2 samples in tension and were the first to report closed hysteresis loops in the narrow stress range between 120 and 200 MPa (Fig. 3)

1.2 Objectives and thesis outline

The ultimate goal of the study is to understand the mechanical response and the physical origin of the nonlinear, hysteretic response exhibited by KNE solids. We also present our efforts to develop a theoretical framework to model and understand

both the microscale and macroscale aspects of the mechanical behavior of KNE solids in general and Ti_3SiC_2 in particular.

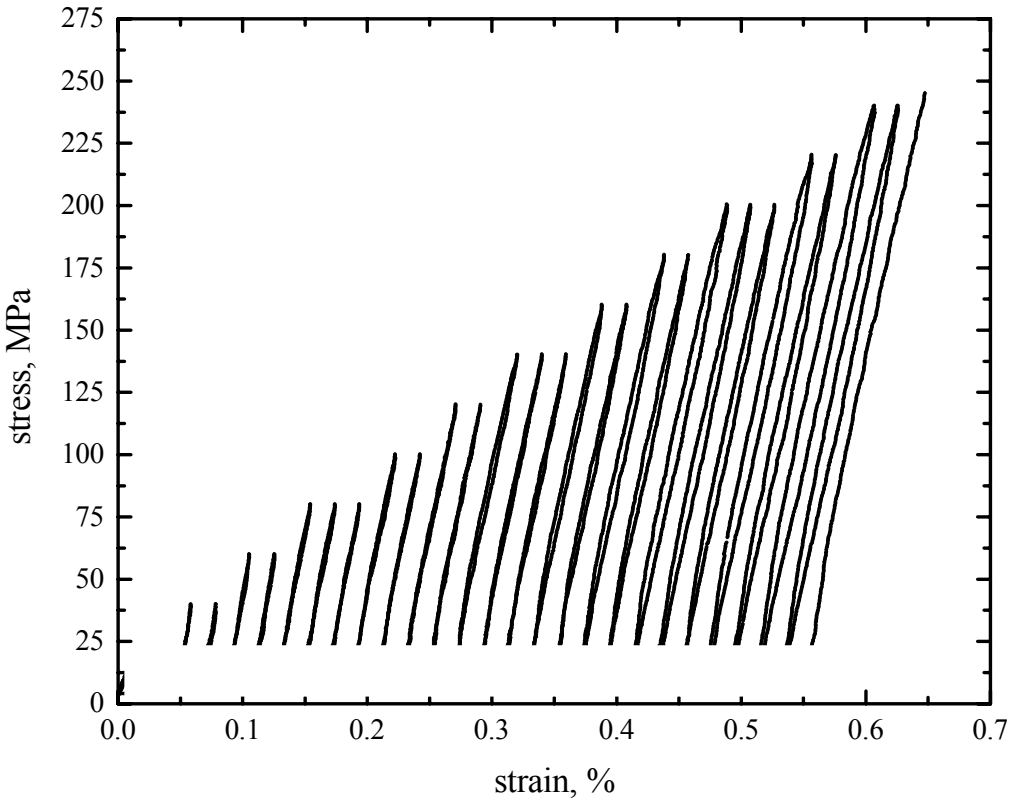

Fig.3 Room temperature stress-strain curves obtained from cyclic loading-unloading tests for FG microstructure at a constant rate of 0.67 MPa/s for increasing stress amplitude [10].

This thesis is a collection of published (chapter 2) [11], or prepared for publication (chapters 3, 4 and 5) [70, 71, 72] papers. The chapters are organized more chronologically than thematically. The author believes that such an order will help the reader to learn gradually about the mechanical properties of KNE solids as he did during his work.

In chapter 2 we discuss our recent work on the compressive behavior of KNE solids at room temperature and present our efforts to develop a theoretical framework to model and understand both the microscale and macroscale aspects of the mechanical behavior of KNE solids. The results obtained from high temperature compressive creep and stress relaxation tests carried out on fine and coarse grained Ti_3SiC_2, a prime example of the KNE solids, are presented and discussed in more detail in chapters 3. Chapter 4 gives more detailed information on the effect of temperature, strain rate and grain size on the compressive response of Ti_3SiC_2. In chapter 5 we report the temperature dependent of the elastic constants of Ti_3SiC_2 and Ti_2AlC by resonance ultrasound spectroscopy (RUS) and compare with those results obtained by mechanical methods [10, 11, and 77]. Another important property, the ultrasonic attenuation, is also investigated as a function of temperature and deformation history.

2. Compressive Behavior of Kinking Nonlinear Elastic Solids at Room Temperature

2.1 Introduction

Slip by dislocation motion is the prevalent micro-mechanism of plastic deformation in virtually all of the crystalline materials. It is widely recognized that crystalline materials that exhibit a large multiplicity of easy glide slip systems (for example, face-centred and body-centred cubic metals) demonstrate significant ductility, and that dislocation activity in these materials is irreversible, that is, it is not possible, in general, to return the material to its initial microstructural state. It is also well known that materials that exhibit limited amounts of slip are generally brittle (for example, ceramics), which hinders their use in a number of engineering applications. Most known crystalline materials fall into one of the two categories described above.

In our recent work [11-14], we have shown that the MAX phases, mica, graphite, and most probably ice, can be classified as kinking nonlinear elastic (KNE) solids. The MAX phases are a new class of layered machinable ternary carbides and nitrides, with the chemical formula $M_{n+1}AX_n$, where M is an early transition metal, A is an A-group element (mostly IIIA and IVA) and X is C or N. Ti_3SiC_2 is a prime example of the MAX phases, and its properties have been extensively studied by our group [10-14, 32-43]. We also believe that many of the so called nonlinear

mesoscopic elastic (NME) solids discussed in geological literature [4-9] are also in fact KNE solids [13]. All KNE solids deform primarily by the kinking, or the formation of kink bands. Kinking, a mechanism reported first by Orowan in single crystals of Cd loaded parallel to the basal planes [47], is the physical origin of the hysteretic, nonlinear elastic, behavior exhibited by these solids.

The loading-unloading stress-strain curves of KNE solids in the elastic regime outline nonlinear, fully reversible, reproducible, rate-independent, closed hysteresis loops whose shape and extent of energy dissipated are strongly influenced by grain size with the energy dissipated being significantly larger in the coarse-grained material. In Fig. 4 we show a schematic complex but typical loading-unloading stress-strain response of a KNE solid (see Fig. 21b for similar experimental results), in which the stress is reversed five times in the course of the measurement. The response is highly nonlinear and hysteretic. The intermediate loading-unloading cycles of stress produce two small, interior hysteresis loops inside the larger, exterior hysteresis. The interior loops in Fig. 4 seem to suggest that the material remembers the stress-strain condition prior to a local excursion. For example, when the stress-strain trajectory reaches the point A and a partial unloading-loading excursion is taken, the material remembers this point and returns to this exact same point, and then continues along the original stress-strain trajectory. This phenomenon has been referred to as discrete memory [4, 5 and 6] or as endpoint memory in studies on magnetism [4]. In prior studies [11-14], we have attributed these unique characteristics of the mechanical response of KNE solids to the formation and

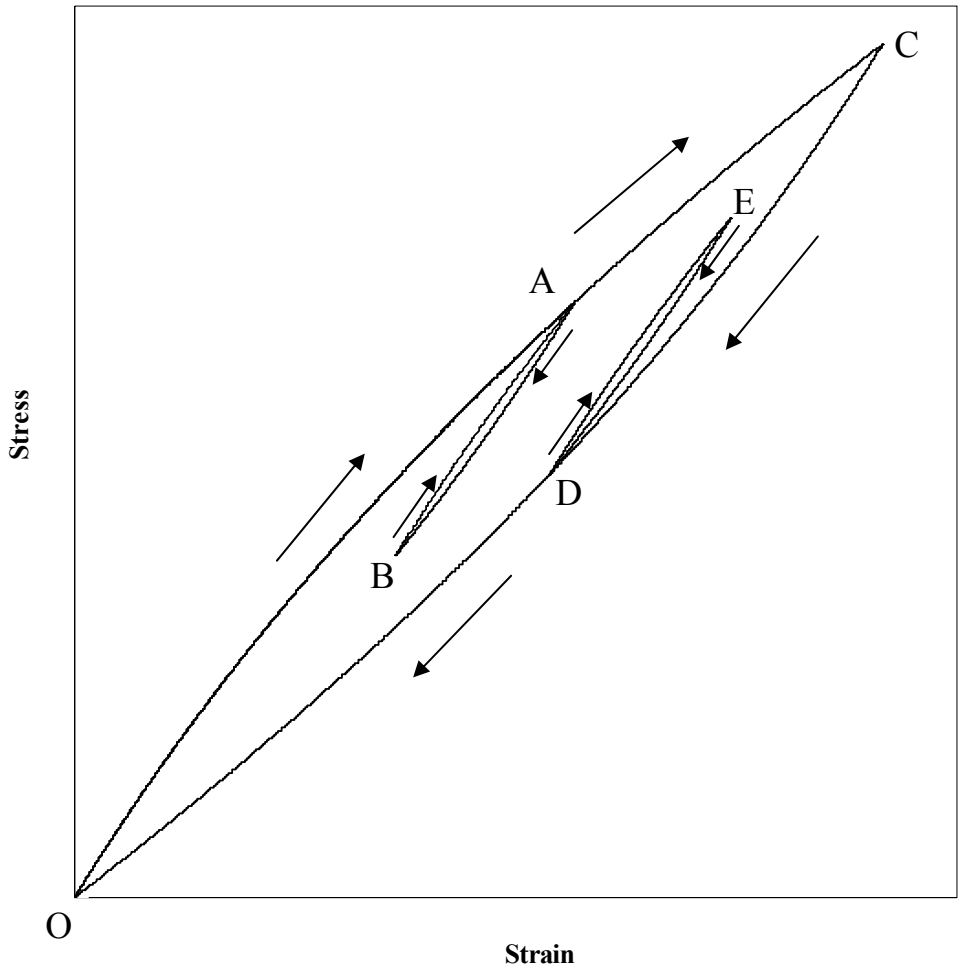

Fig. 4 Schematic diagram of a complex loading-unloading stress-strain response of KNE solid. The arrows in the figure represent the loading direction.

annihilation of incipient kink bands (IKB, discussed in more detail later). Incipient and regular kink bands have also been held responsible for the fully reversible and hardening behavior of KNE solids indented with a spherical indenter at the nano-length scales [12-14].

It is strongly believed that the unique characteristics of the mechanical behavior of KNE solids reported in here can be attributed largely to the following known facts about this material: i) Basal slip, and only basal slip, is operative at all temperatures[36, 38]. ii) Because they are confined to the basal planes, dislocations arrange themselves either in arrays (pileups) on the same slip plane, or in walls (tilt and twist boundaries) normal to the arrays [35-38]. Dislocation interactions, other than orthogonal, are difficult and unlikely to occur. Hence dislocations can move back and forth reversibly and extensively. iii) Because of their high c/a ratios, twinning is unlikely, and has never been observed. Instead, deformation occurs by a combination of glide and the formation of kink bands within individual grains [35, 36].

Kinking is distinct from slip or twinning in that it requires the generation of a succession of, more or less, regularly spaced dislocation *pairs* on many parallel slip planes [36, 38]. Frank and Stroh [48], modeled kinks as thin infinite elliptic cylinders (with axes 2α and 2β such that $2\alpha >> 2\beta$, Fig. 5a), whose sides are comprised of two dislocation walls of opposite sign, with Burgers vector **b** and spacing D. The precise mechanisms responsible for nucleation of kinks have not yet been identified.

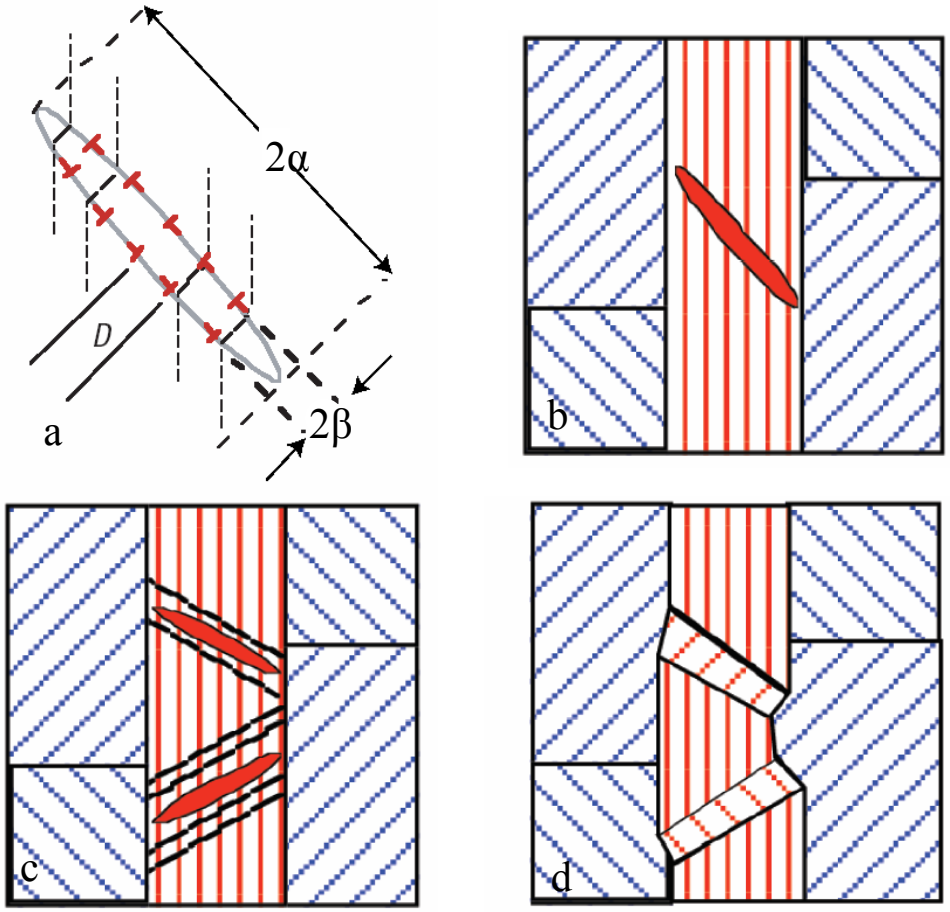

Fig. 5 Schematic description of the formation of a kink-band. a) A thin elliptical sub-critical kink nucleus if formed with $2\alpha >> 2\beta$. The boundaries are comprised of dislocation walls (shown in red) of opposite sign, and a uniform spacing of D. b) Formation of an IKB in hard (red) grains adjacent to soft (blue) grains. The lines in the grains denote basal planes. c) Multiple pile-ups and kink bands in a large grain. Dashed lines denote walls that have separated from the source and are moving away from it. This only happens at higher temperatures and/or high stresses. d) Same as (c) after removal of stress, emphasizing formation of internal grain boundaries (dark lines) leading to kink bands.

It is believed that once the kinks nucleate they grow athermally until they meet the grain boundaries (interior grains) or free surface (exterior grains). At the grain boundaries, the opposite walls of the kink are held together giving the kink a lenticular shape (Fig. 5b). At high stress or high temperatures, the dislocation walls bounding the kink separate (Fig. 5c), and coalescence of several such walls eventually produces a kink band (Fig. 5d) that have been documented extensively in the literature [35-41, 47-49]. To avoid confusion, the term incipient kink band (IKB) is used in here to denote a kink band for which the dislocation walls remain *attached* at its ends, i.e. one that remains lenticular in shape (Fig. 5a). It would, of course, be annihilated when the load is removed. Thus, by definition, IKBs are fully reversible.

In this chapter, we report our recent work on the compressive behavior of KNE solids at room temperature and present our efforts to develop a theoretical framework to model and understand both the microscale and macroscale aspects of the mechanical behavior of KNE solids. At the microscale, building on the theory proposed by Frank and Stroh [48], we examine two different approaches to computing the volume fraction of the material transformed to IKBs, and examine if the estimated values from these different approaches are reasonable. Also, based on the proposed IKB model, the deformation contributed by the IKBs is estimated and compared with the experimental value. We then used the experimentally observed trends for the evolution of the volume fraction of IKBs to propose a phenomenological description for macroscale constitutive modeling. Using such a description, we present a new constitutive model that focuses on capturing reliably

the nonlinear, fully reversible, hysteretic, rate-independent, and discrete memory aspects of the macroscale behavior of KNE solids. In this first development, we have only dealt with the one-dimensional description of the constitutive response.

2.2 Experimental Procedure

The procedure for fabricating fine-grained (FG) and coarse-grained (CG) Ti_3SiC_2 samples can be found elsewhere [40]. Briefly, the specimens were produced by reactive hot isostatic pressing (HIPing) a stoichiometric powder mixtures of titanium (-325 mesh, 99.5 %, Alfa Aesar, Ward Hill, MA), silicon carbide (- 400 mesh, 99.5 %, Atlantic Engineering Equipment, Bergenfield, NJ) and graphite (- 300 mesh, 99 %, Alfa Aesar, Ward Hill, MA). HIPing at 1400 °C at a pressure of 40 MPa for 8 hours resulted in a fine-grained (FG) microstructure; HIPing at 1600 °C , 40 MPa for 8 hours resulted in a coarse-grained , CG, microstructure.

For reasons that are not entirely clear we were not able to fabricate fully dense, single phases samples of Ti_3GeC_2 by HIPing. Instead, coarse-grained, CG samples of Ti_3GeC_2 were prepared by hot pressing. Roughly of the stoichiometric mixture of Ti, Ge and C powders were ball milled for about 40 min; poured and wrapped with BN presprayed graphite foils. The latter were placed in a graphite die in the hot press, which was heated at a rate of 100 ºC/min. to 900 °C, held there for 3 h after which a pressure of ~ 45 MPa was applied and heating was resumed at the

same rate to 1600 º C and held at temperature for 6 h, before furnace cooling. These samples were further annealed at 1600 ºC for 48 h resulted in CG microstructure. The FG Ti_3GeC_2 was made by the same procedure except held at 1600^oC for 8 h without further annealing [50, special thanks to Adrish to allow the author to use his sample].

For Ti_3SiC_2 and Ti_3GeC_2, tests were performed using cylindrical shaped specimens (9.7 mm in diameter and 31 mm in height), with a gauge length of 25 mm. They were electro-discharge machined (EDM) and tested with no further surface preparation.

In addition a graphite block (Grade ISO-63, Toyo Tanso USA, Troutdale, OR) with a particle size of 5 μm, a density of 1.83 Mg/m^3 and a compressive strength of 181 MPa was machined into cylinders 9.7 mm in diameter and 31 mm high. Maycor™ (Ceramic Productions Inc, Palisades Park, NJ) block with ≈ 55 vol.% mica was machined to small cylinders (12.7 mm in diameter; 31 mm in height). A hot-pressed boron nitride rod (Grade BO. Accuratus Ceramic Corporation, Washington, NJ) with a compressive strength of ≈ 186 MPa along the hot-pressing direction was machined to cylinder shaped samples (16 mm in diameter, 32 mm height) for compressive testing.

All the tests were performed in air using a hydraulic MTS 810 testing machine, which was supplied with a controller (Microconsoler 458.20) that allowed tests to be run in displacement or load control mode. In all tests, a preload

corresponding to a stress of ≈ 1 ~ 2 MPa was applied to keep the sample aligned. All the cyclic loading-unloading tests were performed by using load-control mode. Strains were measured by a capacitance MTS extensometer, with 5 % capacity; the force was measured using a load cell with 100 kN capacity.

2.3 Results

Typical compressive loading-unloading stress-strain curves of Al_3O_2, T2024 (Al alloy), FG and CG Ti_3SiC_2 are shown in Fig. 6. The results presented in Fig. 4 unequivocally demonstrate:

i. Unlike the linear elastic response of Al_3O_2 or T2024, the loading-unloading stress-strain curves Ti_3SiC_2 are nonlinear behavior. Closed, fully reversible hysteresis loops are observed for both the FG and CG microstructures.
ii. The shape and extent of energy dissipated are strongly influenced by grain size with the energy dissipated being significantly larger in the coarse-grained material.

Figure 7 shows the cyclic compressive stress-strain curves of FG and CG grained Ti_3GeC_2 cylinder. Here again we observed microstructure dependent, nonlinear and closed hysteresis loops. It should be noted here that the reproducibility

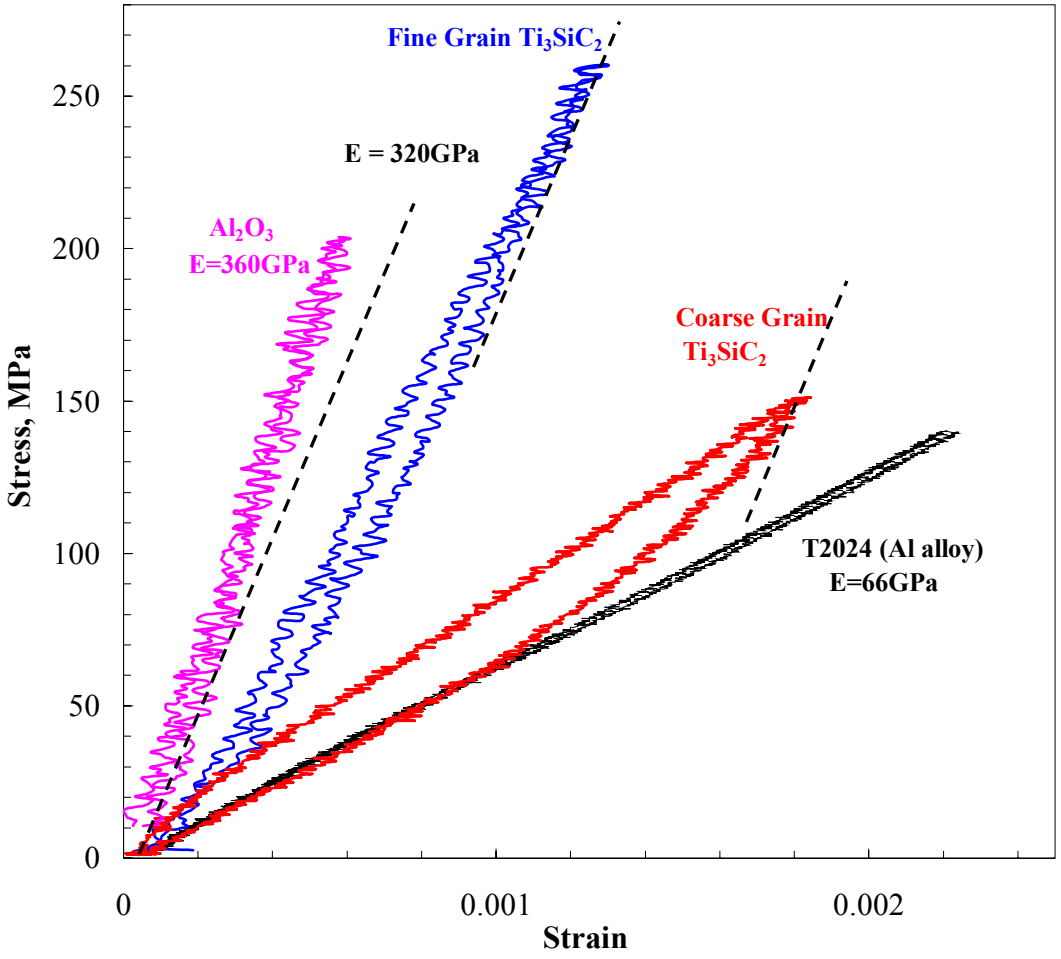

Fig. 6 Stress-strain curves for fine and coarse-grained Ti_3SiC_2, Al_2O_3 and Al. The dashed lines are linear elastic response expected from Ti_3SiC_2 had kinking not occurred. E denotes Young's modulus [72, 73].

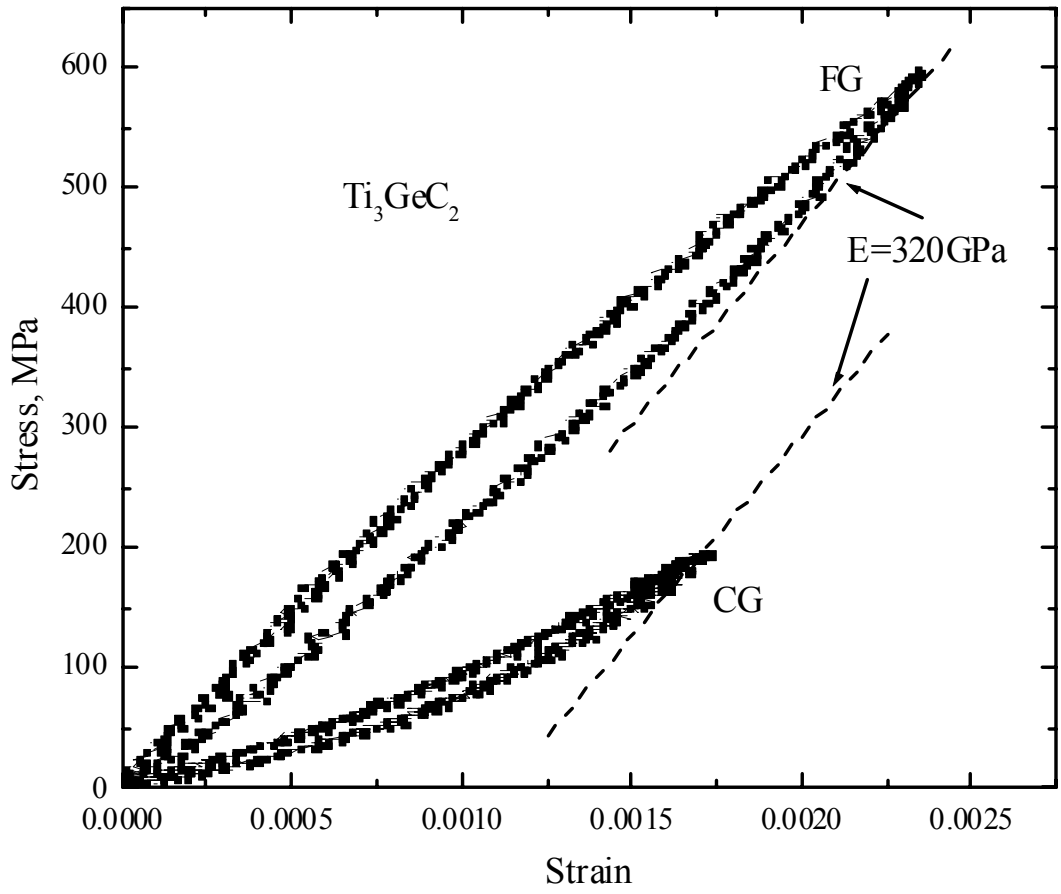

Fig. 7 Stress-strain curves for fine and coarse-grained Ti_3GeC_2. Each cycle represents 3 consecutive cycles for each microstructure. The dashed lines are linear elastic response expected from Ti_3GeC_2 had kinking not occurred. E denotes Young's modulus.

is noteworthy, three cycles for each microstructure are depicted in Fig. 7. Also the initial unloading slopes of stress-strain curves of both microstructures are close to 320 GPa, the theoretical Young's modulus obtained by ultrasound method (see Fig. 5).

The stress-strain curves of four successive cycles, each to a higher stress level from 36 to 75 MPa, obtained on macroscopic polycrystalline graphite are shown in Fig. 8. Clearly, there is a single loading curve and the hysteresis loops appear to be fully reversible. When loaded to a stress of 85 MPa, however, the first loop is open, but subsequent cycles to the same stress level are fully reversible (Fig. 9a), with a reproducibility that is again noteworthy. The continuous cyclic tests at 56 MPa after the 85 MPa cycle (Fig. 9a) are show in Fig. 9b. There are three cycles shown here and the loading-unloading rate of each cycle differs from the others by a factor of ten. The inset of Fig. 9b shows the stress-strain history of the tests. It clearly shows the response is independent of strain rate in the 10^{-5} to 10^{-3} s^{-1} range.

The mechanical response of BN carried out with increasing cyclic stresses is shown in Fig. 10a. There are three cycles in each stress level. These results clearly show that the first cycle is open, indicating the plastic deformation during the first loading cycle at each stress level. This behavior is more obvious at higher stress levels, i.e. the plastic deformation of first cycle at 150 MPa is more than twice than that of 50 MPa cycle's. The following loops at each stress level appear to be closed. Figure 10b shows the stress-strain curves of continuous cyclic tests at 150 MPa after

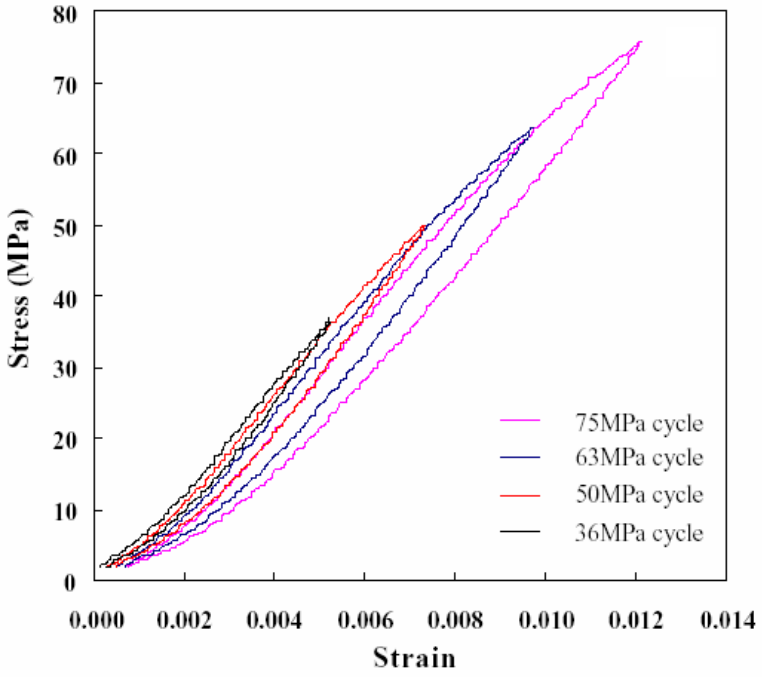

Fig. 8 Compressive cyclic loading-unloading stress-strain curves of polycrystalline graphite as successively increase the stresses from 36 MPa up to 75 MPa at room temperature.

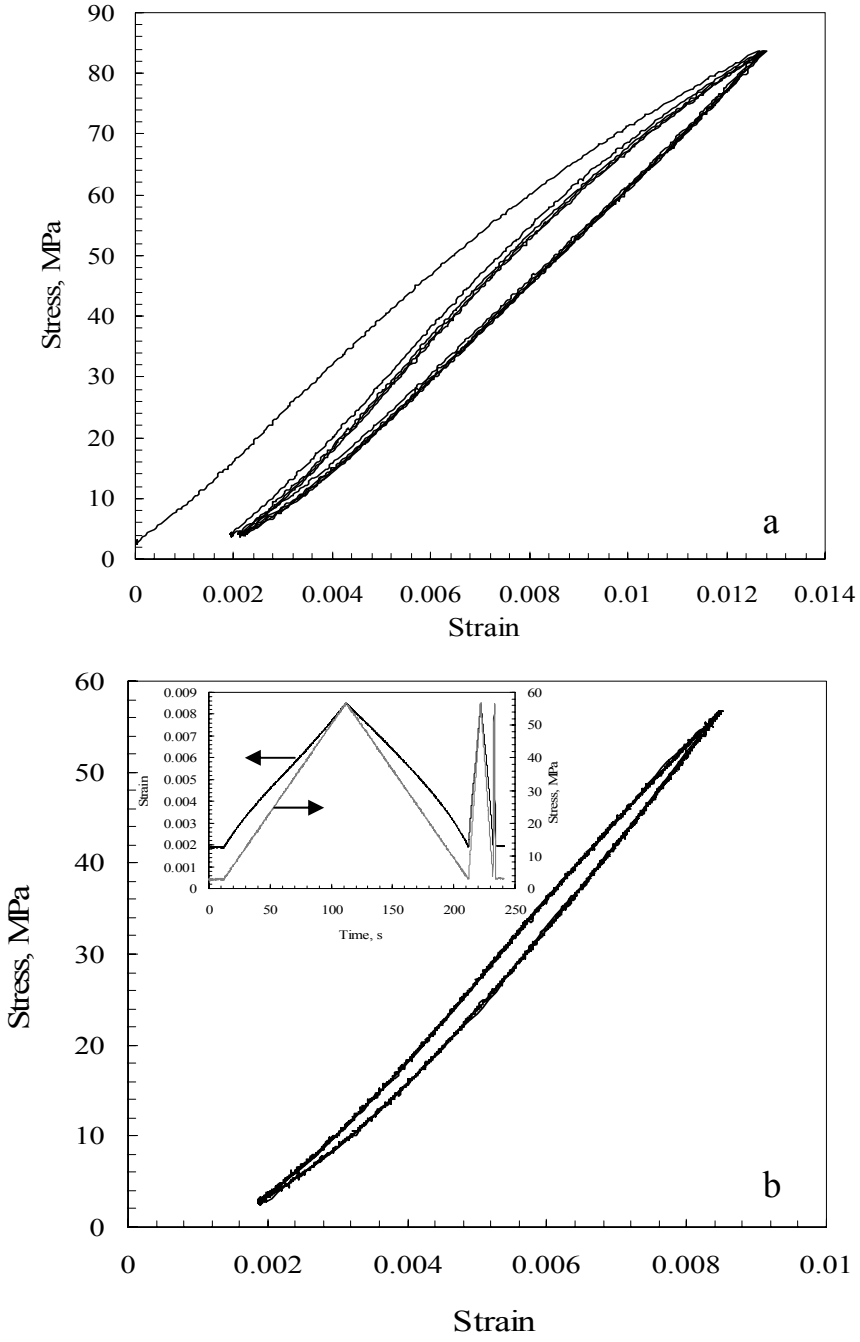

Fig. 9 Compressive cyclic loading-unloading stress-strain curves of polycrystalline graphite at room temperature. a) Cyclic test at 85 MPa. b) Continuous cyclic test at 56 MPa after (a).

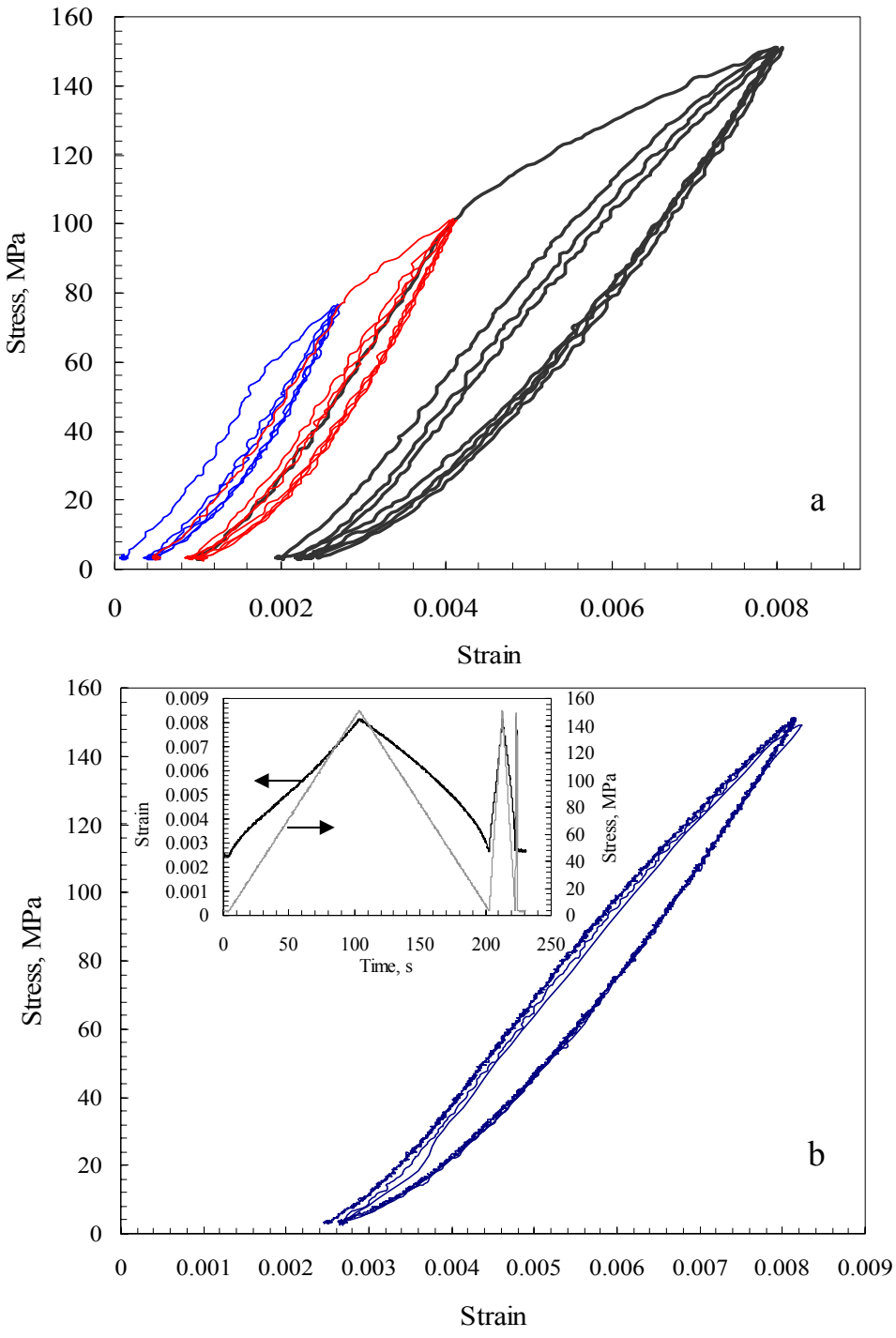

Fig. 10 Compressive cyclic loading-unloading stress-strain curves of hot-pressed BN at room temperature. a) Successively higher stresses from 75 MPa up to 150 MPa. b) Cyclic test at 150 MPa.

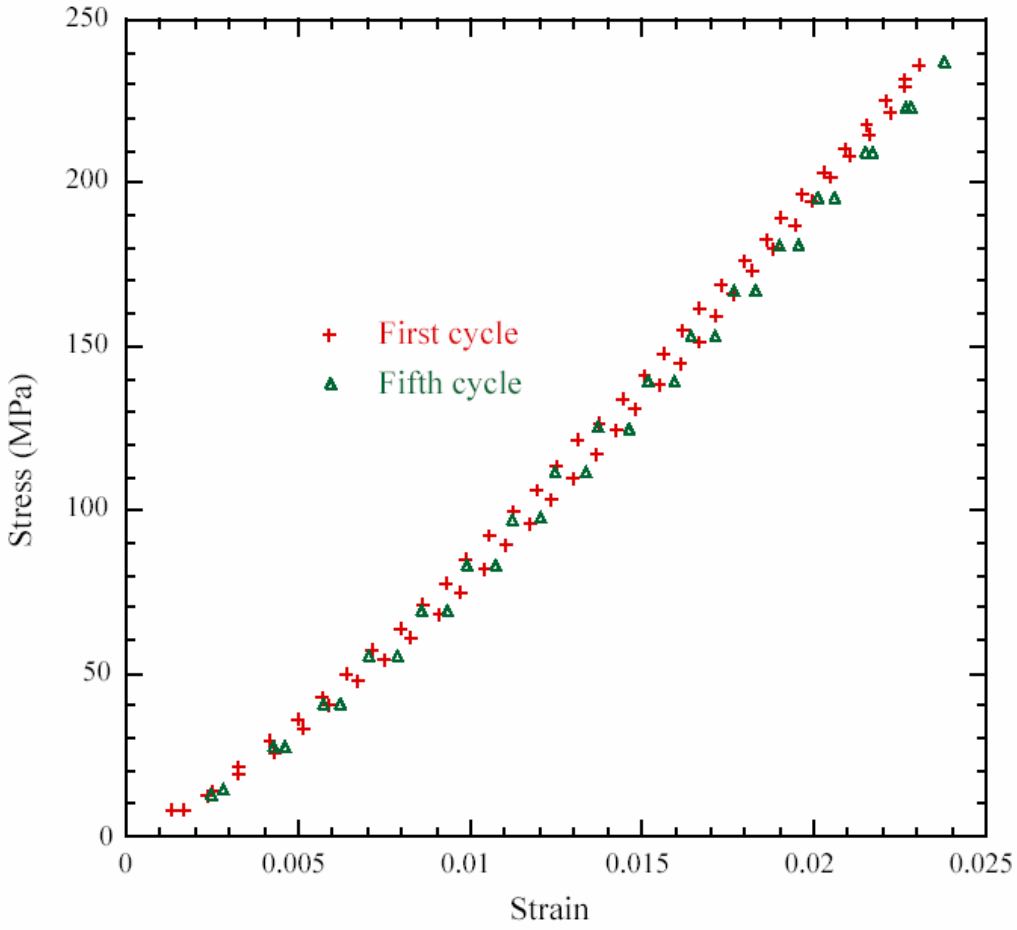

Fig. 11 Stress-strain curves obtained by compressing Maycor™

cyclic tests as shown in Fig. 10a. There are three cycles shown here and the loading-unloading rate of each cycle differs with the others by a factor of ten (inset of Fig. 10b). It clearly shows the compressive response of BN is also independent of strain rate in the 10^{-5} to 10^{-3} s^{-1} range.

Figure 11 shows the compressive loading-unloading stress-strain curves of a bulk mica-containing glass-ceramics, Maycor™. In this figure, only the first and fifth cycles are shown. Clearly, and similar to Ti_3SiC_2 and graphite, this response is neither elastic nor plastic, but non-linear elastic.

The above results clearly show that regardless of their type of bonding, Ti_3SiC_2, Ti_3GeC_2, graphite, mica and BN all exhibit nonlinear, reproducible, and closed stress-strain hysteresis loops when loaded in compression. In the rest of this section we will focus on the compressive response of Ti_3SiC_2 on stress and strain rates. Also high stress cyclic test results are presented.

When FG Ti_3SiC_2 samples were compressed cyclically with progressively higher stresses up to a maximum stress of 1 GPa all loading curves were identical (Fig. 12a). As important, and despite the fact that the deformation was fully reversible up to 1 GPa, the response was non-linear. The time dependencies of the stresses and strains recorded during cycling twice to 1 GPa clearly show them to be identical (Fig. 12b). Here the unloading rates were 10 times the loading rates.

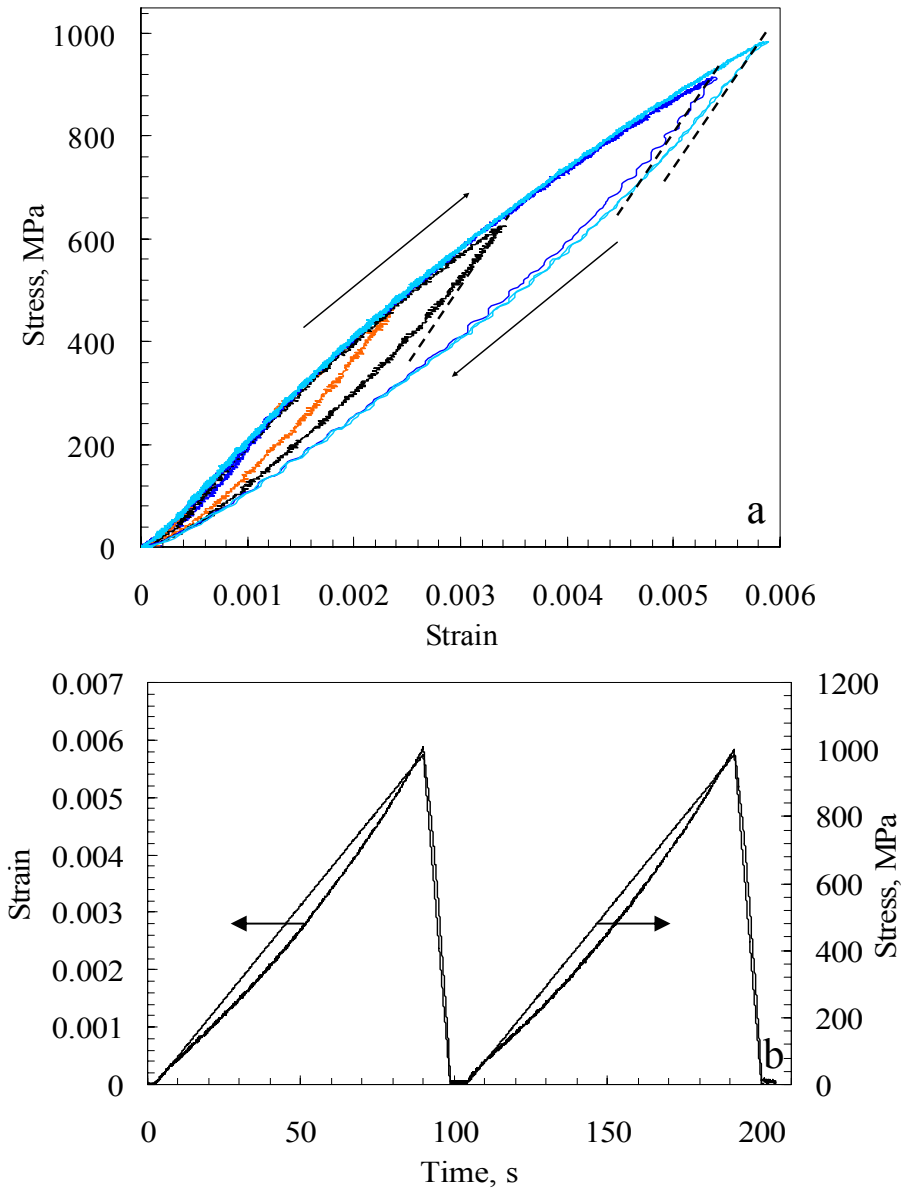

Fig. 12 a) Room temperature loading-unloading stress-strain curves for fine grain Ti_3SiC_2 at 260, 465, 625, 915 and 985 MPa in compression. All the tests have the same loading and unloading rate, except for the unloading rate of 915 and 985MPa, unloading rate was ten times faster than loading rate. The dashed lines represent Young's modulus = 320 GPa. The arrows mean loading direction. b). the stress-strain vs. time curve for the 985 MPa curve as shown in (a).

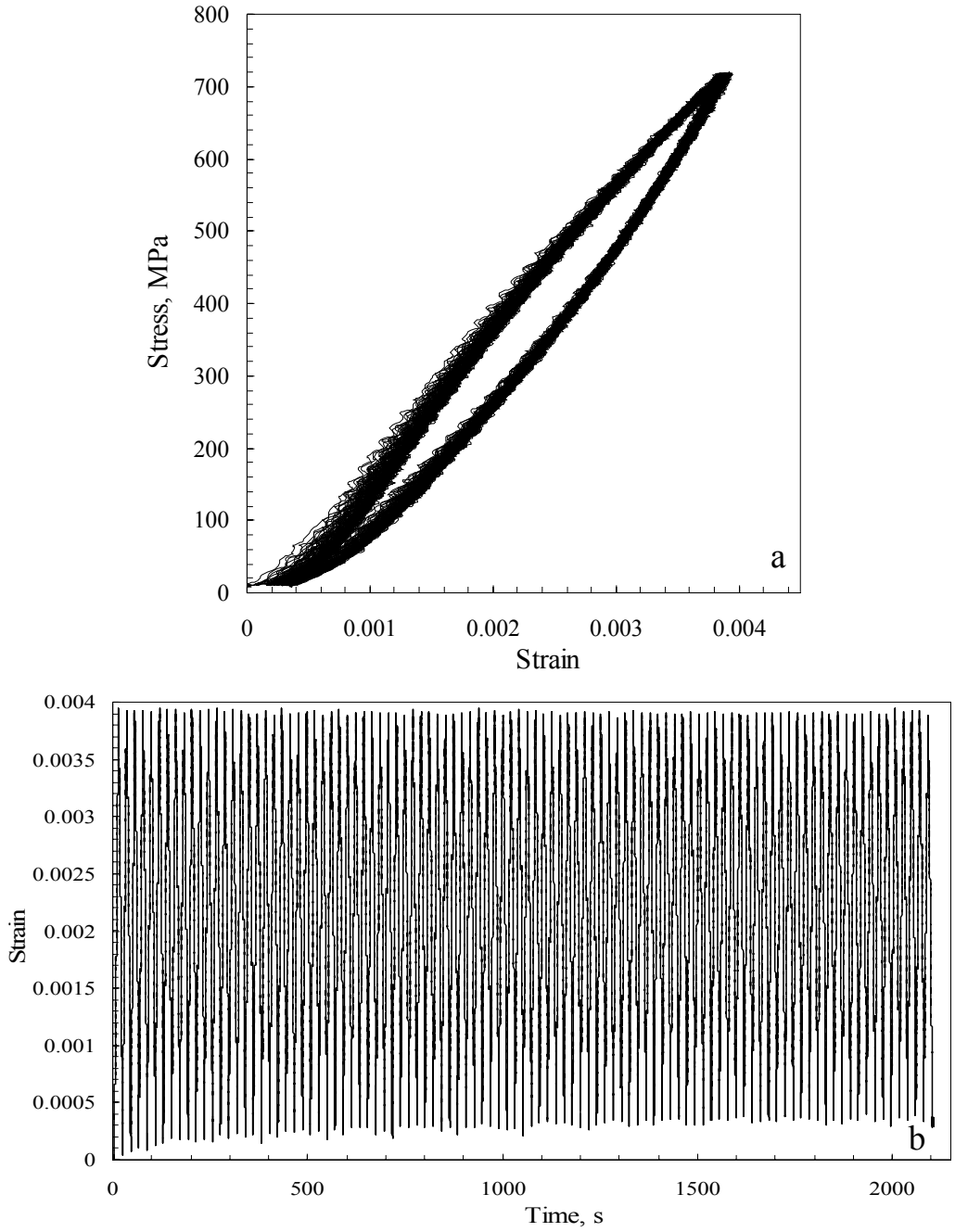

Fig. 13 Room temperature cyclic tests for fine grain Ti_3SiC_2 in compression. a) Stress-strain curves of 100 cycles at 718 MPa. b) Strain-time curve of 100 cycles up to 718 MPa.

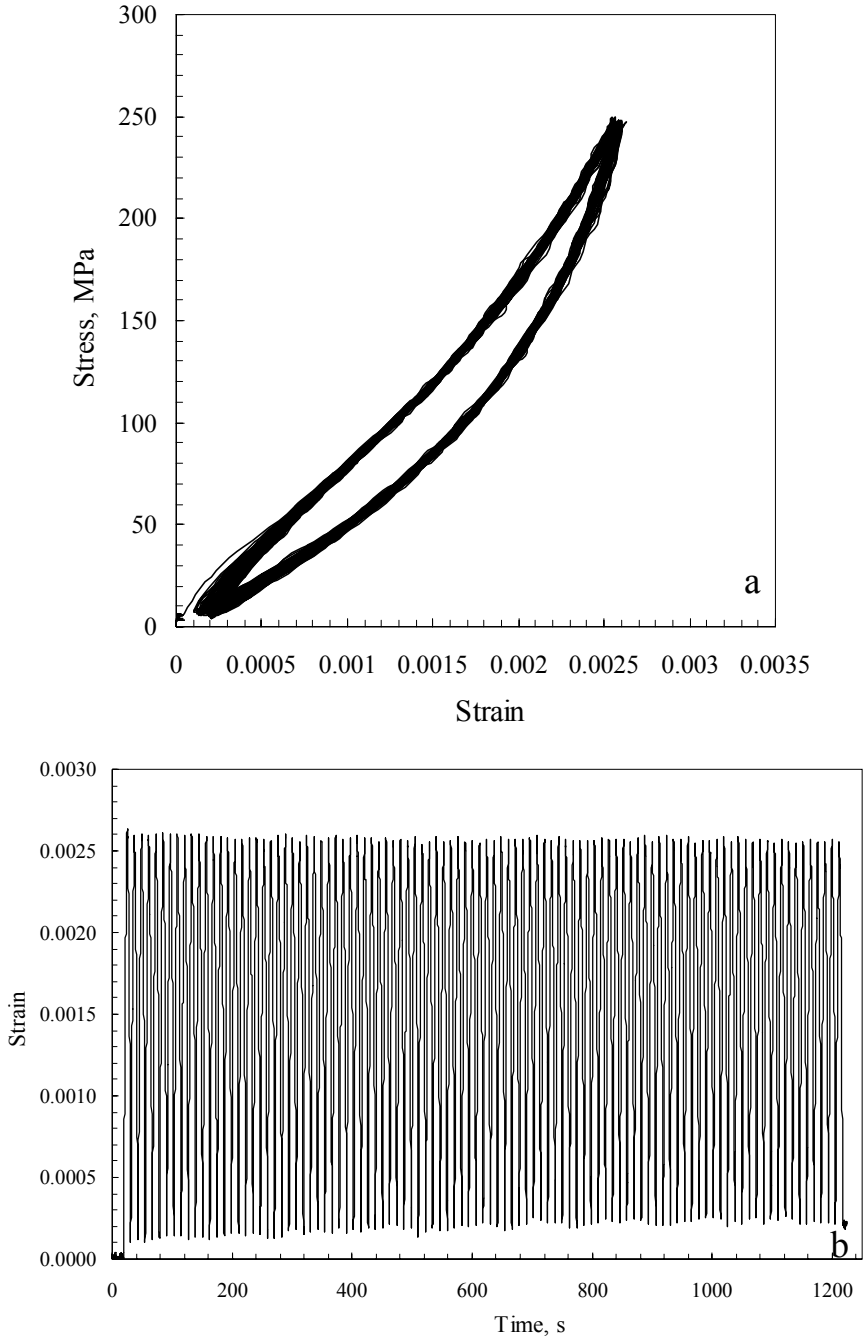

Fig. 14 Room temperature cyclic tests for coarse-grained Ti_3SiC_2 in compression. a) Stress-strain curves of 100 cycles at 250 MPa. b) Strain-time curve of 100 cycles up to 250 MPa.

The full reversibility of the deformation was also not a function of the number of cycles, at least up to 100 cycles. When a FG Ti_3SiC_2 sample was cycled 100 times to 718 MPa (Fig.13) and a CG Ti_3SiC_2 sample was cycled 100 times at 250 MPa (Fig. 14), there were no discernable differences between the first and the last loops (Figs. 13b and 14b).

In order to investigate the strain rate effect on the mechanical response of Ti_3SiC_2, two different tests were carried out on different microstructures. Figure 15 plots the stress-strain curves of three cycles that differed from each other by a factor of 10 each in the loading and unloading rates for CG Ti_3SiC_2. The reproducibility is noteworthy. It clearly shows the response is independent of strain rate at least in the 10^{-5} to 10^{-3} s^{-1} range. To further explore this important aspect, a FG sample was loaded to 600 MPa; unloaded to 450 MPa, held at that stress for one minute before further unloading to 250 MPa and held there for one minute. The corresponding dependencies of strain and stress on time clearly show the samples do *not* creep at room temperature (Fig. 16a). Consequently, during unloading there is only one unloading trajectory (Fig. 16b).

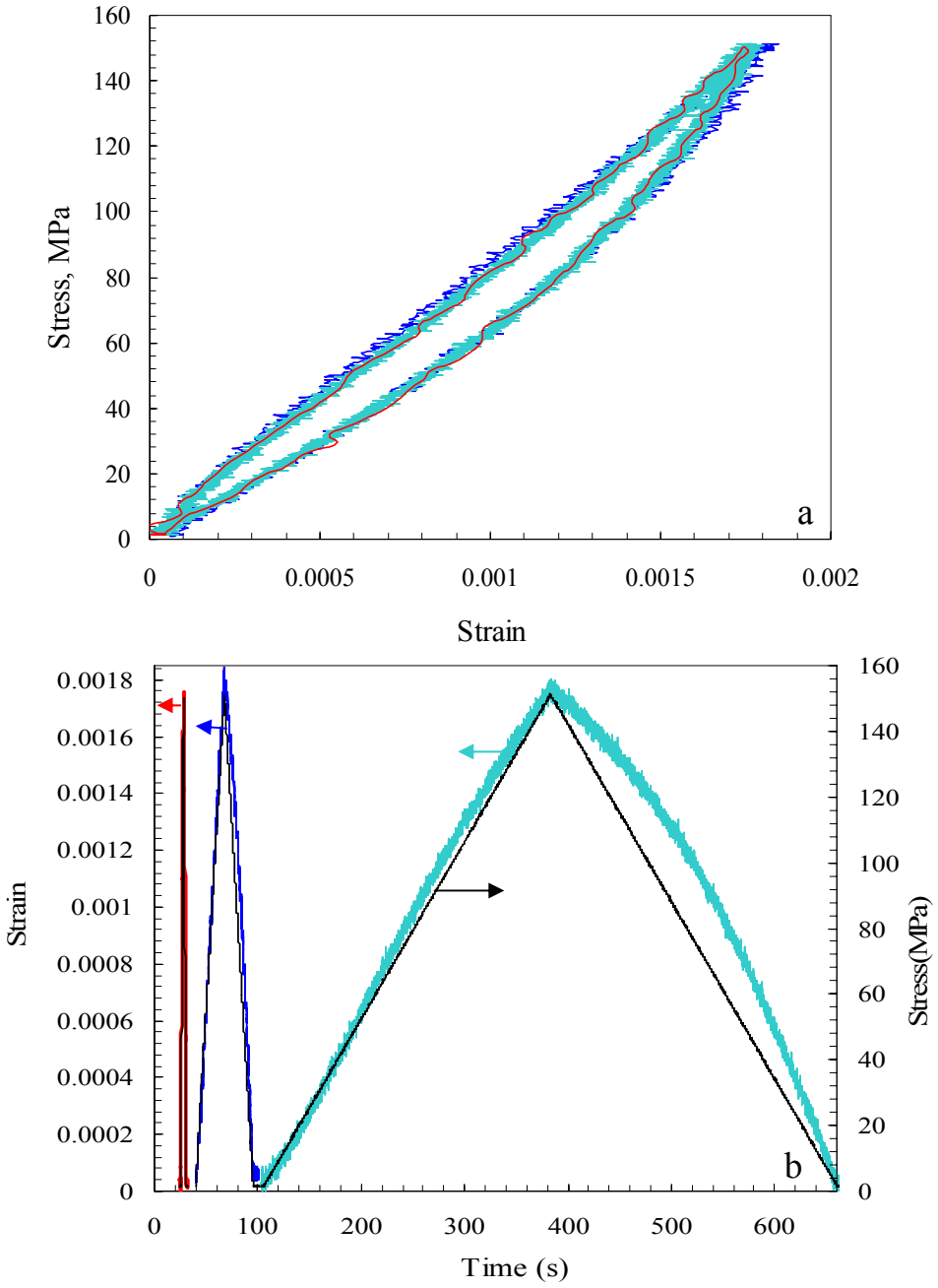

Fig. 15 Room temperature rate effect of coarse grain Ti_3SiC_2 in compression. a). Stress-strain curves of three loading-unloading cycles, each differing from the others by a factor of ten in loading-unloading rate. b). Stress-strain vs. time of three loading-unloading cycles showed in (a).

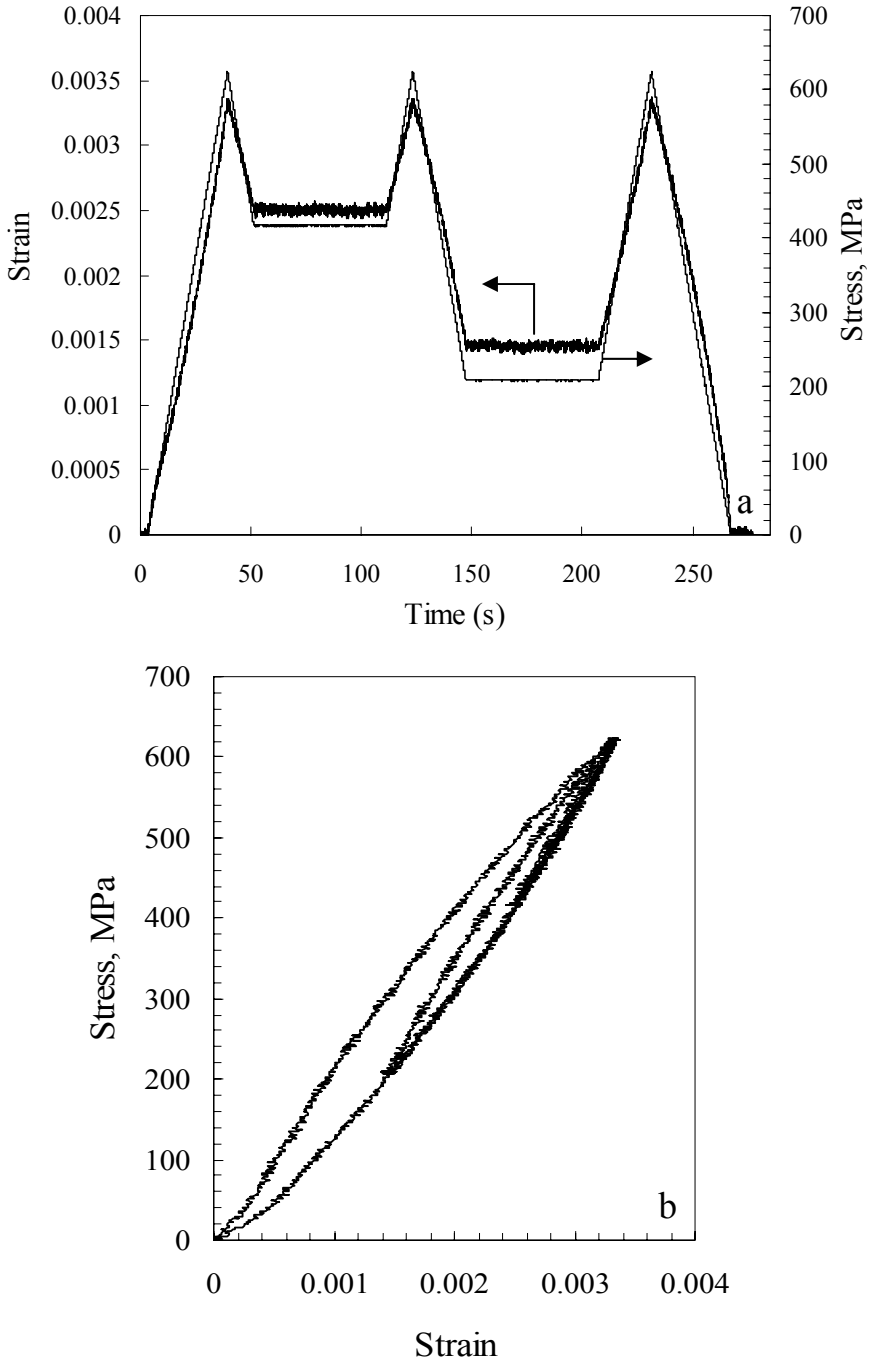

Fig. 16. Room temperature stress dip test for fine grain Ti_3SiC_2 in compression. a) Strain-stress vs. time curve of the stress dip test. b) Stress-strain curve of the stress dip test.

2.4 Discussion

The area enclosed by the hysteresis loop reflects the energy dissipated per unit volume per cycle, W_d. A log-log plot of W_d vs. maximum loading stress, σ, of Ti_3SiC_2, graphite and mica in simple compression is shown in Figs. 17a and 17b. Also plotted are the corresponding values for Ti_3SiC_2 and graphite, obtained from nanoindentation experiments [12-14]. From these results it is clear that for both Ti_3SiC_2 and graphite, the W_d is proportional to σ^2 over *six* orders of magnitude. As important, the excellent agreement between the values of W_d obtained from bulk samples, and those obtained from the nanoindentation experiments[11,14] for both Ti_3SiC_2 and graphite, is gratifying and indicates that the underlying physics at both length scales is the same.

Note that the W_d values for the bulk mica-containing glass-ceramics (Fig. 17a) fall in between those of Ti_3SiC_2 and graphite (Fig. 17a). Unfortunately these results cannot be directly compared to the nanoindentation ones because the bulk samples were not natural mica, but rather a synthetic glass-ceramic in which fluorphlogopite-based elongated grains are embedded in an amorphous matrix [51]. The purpose of this experiment was to unequivocally show that, like many geologic rocks, mica-containing materials behave in a non-linear elastic manner.

The most compelling evidence, however, that the same mechanisms are operative in all three quite different compounds is shown in Fig. 17b. In this plot,

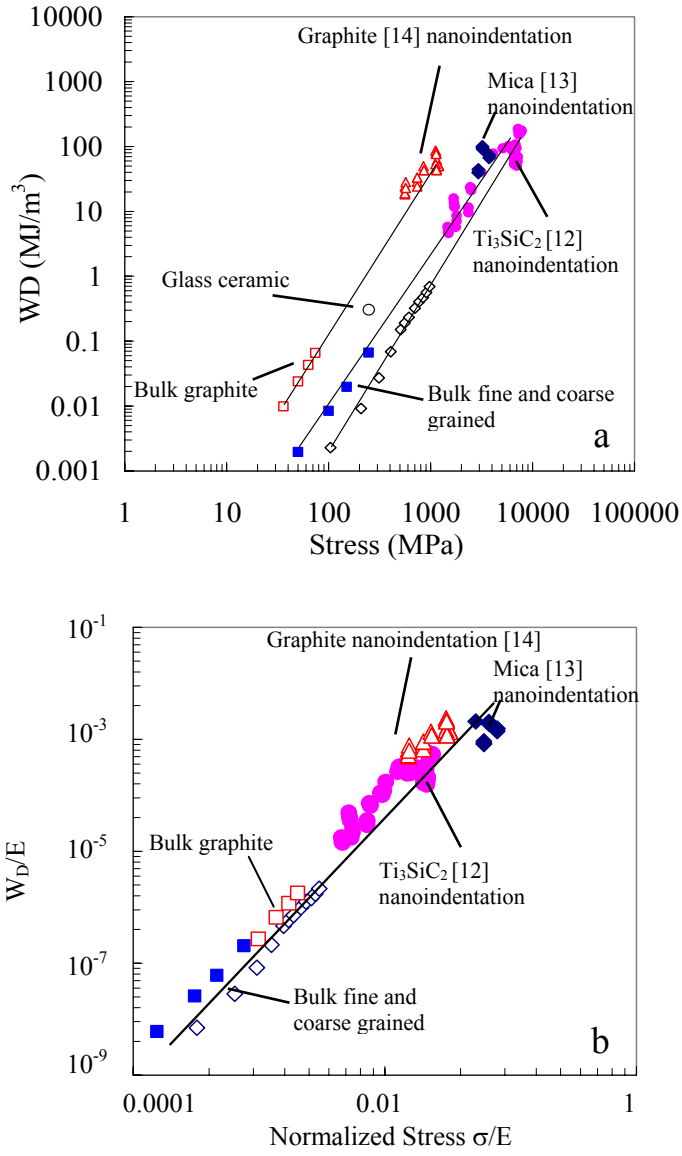

Fig. 17 a) Log-log plot of energy dissipated per cycle, W_D, versus maximum stress applied, σ, for Ti_3SiC_2, graphite and mica. For the former two, the data was obtained either by compressing bulk cylinders (lower left) or from fully reversible nanoindentation work [12-14]. The results for the Maycor™ are in between those of Ti_3SiC_2 and graphite. b) Same as a, but both axes are normalized by either the Young's moduli (bulk) or the stiffnesses along the c-axes, i.e. c33. For mica, c33 is 61 GPa.

Table1. Summary of the elastic constants used for normalizing the axes in Fig. 17b.

	Ti_3SiC_2		Graphite		Mica	
	Bulk	C_{33}	Bulk	C_{33}	Bulk	C_{33}
Elastic constant, GPa	325	325	36.5	36.5	61	61

both axes are normalized by the appropriate elastic stiffness along the indentation axis (Table 1). Based on the resulting *universal* curve it is fair to conclude that the same kinking-based mechanisms are operative in all three solids.

Generally speaking, in crystalline solids, three processes could possibly explain our results [52, 53]: point defect, dislocation and/or grain boundary relaxations. (Phase transformations, twinning, domain relaxations are not germane here. Furthermore as discussed later, microcracking is also not an option). The following facts preclude point defects and grains boundaries as possible sources. First, the weak dependence of W_d on temperature, at least up to ≈ 900 °C (see Ch. 4). Second, the fact that W_d is *larger* in the coarse-grained (CG) material than the fine-grained (FG) material is compelling, unambiguous evidence that grain boundaries are *not* the source; the grain boundary area is higher in the FG samples. Third, is the full reversibility of the process and its insensitivity to strain rate (Figs. 12, 13, 14, 15 and 16).

The hysteresis loss in room temperature tests (Fig. 17a) must thus be related to the reversible motion of dislocations, a well-established phenomenon in the

metallurgical literature [52-55], although it has only been documented thus far at much lower (orders of magnitude) stress and strain levels. For instance, in simple compression experiments on Zn single crystals, Roberts and Brown [54] report strains of $\approx 4 \times 10^{-5}$ at stresses of ≈ 0.25 MPa, for W_d of ≈ 3 J/m^3. Our corresponding values of FG Ti_3SiC_2 are 0.006, 1 GPa and $W_d \approx 0.7$ MJ/m^3. The energy dissipated in the fully reversible hysteresis loops in our work is roughly 6 orders of magnitude higher than those previously reported for crystalline materials. Note also that the energy dissipated corresponds to roughly 25% of the overall mechanical energy in each cycle!

It is hypothesized that the large, fully reversible, hysteresis loops observed in this work can be attributed to reversible formation and annihilation of incipient kink bands (IKBs) described below. This strong assertion is based largely on the results presented herein, and some of the theoretical results presented by Frank and Stroh [48]. In the following part we present our efforts to develop a theoretical framework to model and understand both the microscale and macroscale aspects of the mechanical behavior of KNE solids.

2.4.1 Considerations at the Microscale

Frank and Stroh [48] proposed a model in which pairs of dislocations of opposite sign nucleate and grow as a thin elliptical subcritical kink with dimensions,

2α and 2β, such that $2\alpha >> 2\beta$ (Fig. 5a). The precise mechanism responsible for kink nucleation has not yet been identified. However, from energy considerations, they conclude that beyond a critical kinking angle, γ_c, given by

$$\gamma_c \approx \frac{3\sqrt{3}(1-\nu)}{2G}\tau_{loc} \tag{1}$$

where τ_{loc} is the local stress needed to form a dislocation pair, and G and ν are the shear modulus and Poisson's ratio, respectively. A subcritical kink-nucleus can grow by producing new dislocation pairs at its edges; it can in any case also shrink by annihilation of dislocation pairs. Assuming that $\tau_{loc} \approx G/30$ and $\nu = 0.2$ [35], yields $\gamma_c \approx 4°$. Further, Frank and Stroh [48] show that the remote stress, τ_c, needed to render a subcritical kink nucleus unstable and grow athermally depends on α, and is given by:

$$\tau_c \geq \sqrt{\frac{2bG^2\gamma_c \ln(1/\gamma_c)}{\alpha\pi^2(1-\nu)^2}} \tag{2}$$

The width of the band, β, is given by:

$$\beta \approx \frac{\alpha(1-\nu)\tau_c}{G\gamma_c} \tag{3}$$

Equation 2 suggests that the stress for kinking decreases with increasing α. In reality, α is constrained by the size of the individual grain (or crystal) in which the kink is being produced. Therefore, once a kink nucleus is formed and the condition for unstable growth is met (Eq. 2), the kink will grow rapidly until it meets a grain

boundary, at this juncture it remains undissociated and is referred to as an incipient kink band or IKB.

Mechanistically, or phenomenologically the response to stress of an individual grain in which an IKB forms is shown in Fig. 18; it will only kink when the applied

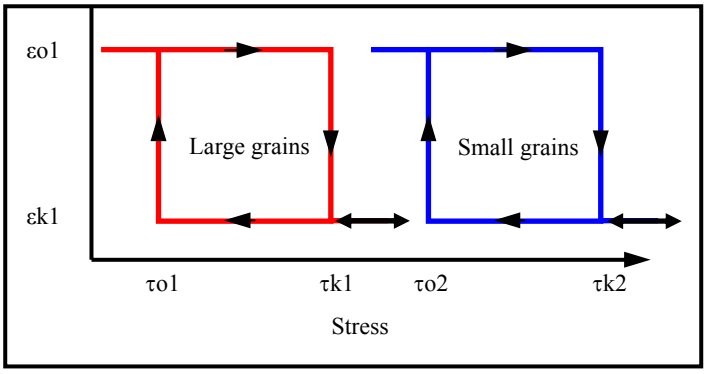

Fig. 18 Schematic description of the mechanical response of IKB-based, microstructure dependent, hysteretic elements in a loading-unloading sequence.

shear stress $\tau_{ki} > \tau_c$ given by Eq. 2. Once it kinks, the domain or grain shrinks by a strain ε_{ki}. When the stress is reduced the friction associated with the dislocation lines will ensure that an IKB disappears at a stress $\tau_o < \tau_{ki}$ (Fig. 18). Since τ depends on

2α, finer-grained samples will form IKBs at higher stresses than coarse-grained samples. IKB's are thus key microstructure dependent *hysteretic* element.

Since our goal is to produce constitutive models for KNE solids, it is important to first identify the appropriate microstructural state variables. For KNE solids, we believe that the volume fraction of material transformed to IKBs, V_{IKB}, is an ideal microstructural state variable. Although, in principal this variable can be defined at the individual crystal level (i.e. it can vary from crystal to crystal depending on grain size and orientation), in this first foray into establishing a constitutive model for KNE solids, we have taken it to reflect the average value for the entire polycrystal.

The total strain, ε, on the sample can be additively decomposed into a linear elastic strain and a kinking strain as

$$\varepsilon = \frac{\sigma}{E} + \varepsilon_{IKB} \tag{4}$$

where σ/E represents the linear elastic component (E denotes the Young's Modulus of the material) and ε_{IKB} represents the strain produced by kinking in IKBs. Since the strain produced by kinking is localized in the IKBs, we can express the following relationship between the overall strain contributed to the sample by kinking and the actual shear strain in the IKBs:

$$V_{IKB} = k\frac{\varepsilon_{IKB}}{\gamma_c} \tag{5}$$

where k represents a factor that relates the shear strain in the individual IKB at the single crystal level to the macroscale uniaxial strain, ε. The factor k would depend on various microstructural parameters that would control the orientations of the IKBs with respect to the loading axis, e.g. the crystallographic texture in the sample. In this first modeling effort, since this type of detailed information is currently unavailable, we simply note here that the value of k is expected to be of the order of one. Combining equations (4) and (5) yields:

$$V_{IKB} = \frac{k}{\gamma_c}\left(\varepsilon - \frac{\sigma}{E}\right) \tag{6}$$

Information on the evolution of the volume fraction of material transformed to IKBs was extracted from the measured stress-strain curves in simple compression on FG Ti_3SiC_2 (Fig. 19a), CG Ti_3SiC_2 (Fig. 19b) and graphite (Fig. 19c) using equation (6). The results are plotted in Fig. 19a, 19b and 19c and also tabulated in Tables 2 and 3. Here k was taken to be equal to one.

Alternatively, one should be able to estimate the volume fraction of material transformed into IKBs from the stored kinking nonlinear elastic energy, i.e. the total stored strain energy during loading minus the energy attributed to linear elastic strain energy arising from stretching of atomic bonds (Fig. 20). To establish such a relation,

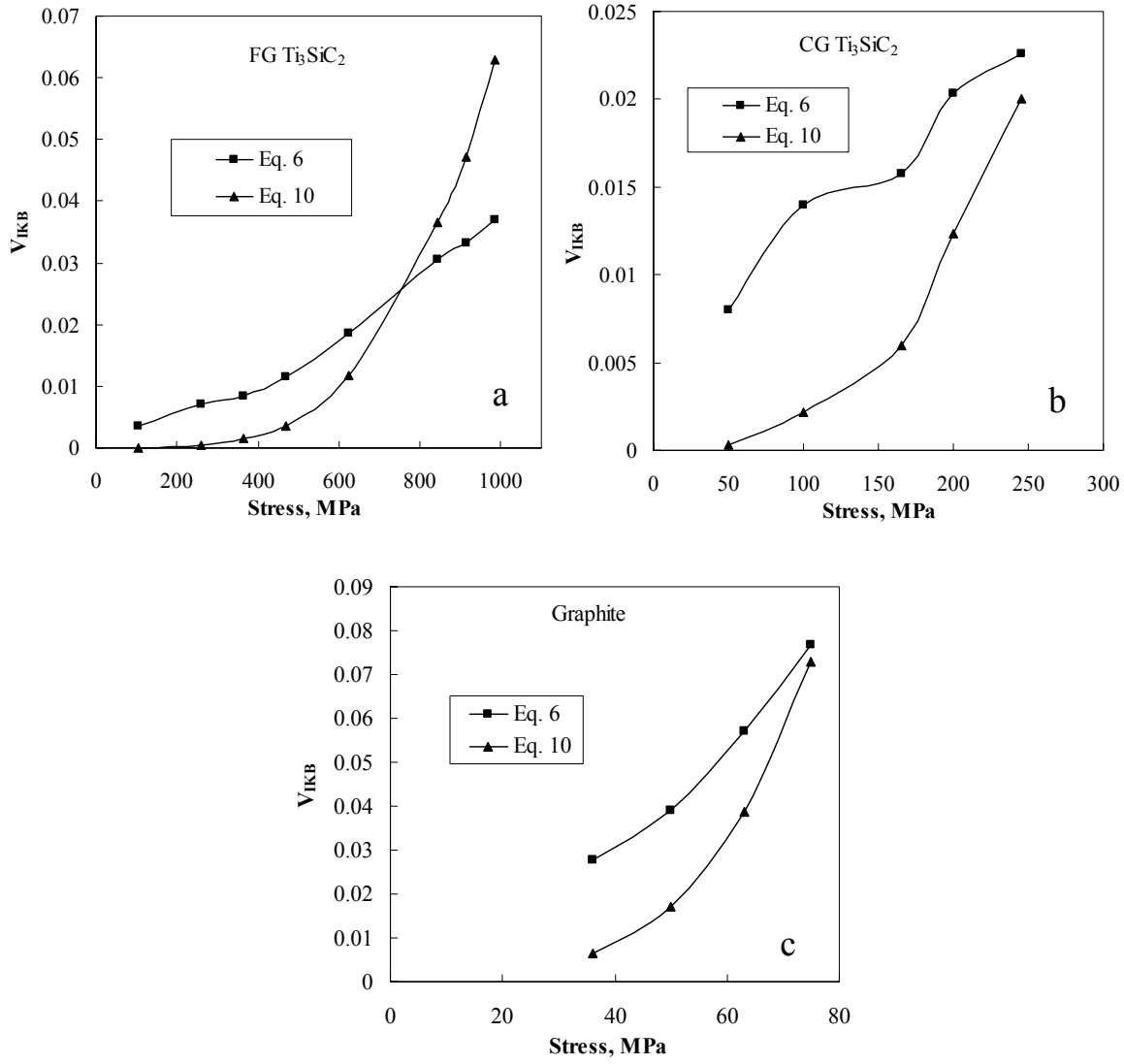

Fig. 19 The evolution of the volume fraction of IKB, V_{IKB}, as a function of the applied stress, computed by two different methods for three different materials. (a) FG Ti_3SiC_2. (b) CG Ti_3SiC_2. (c) Graphite.

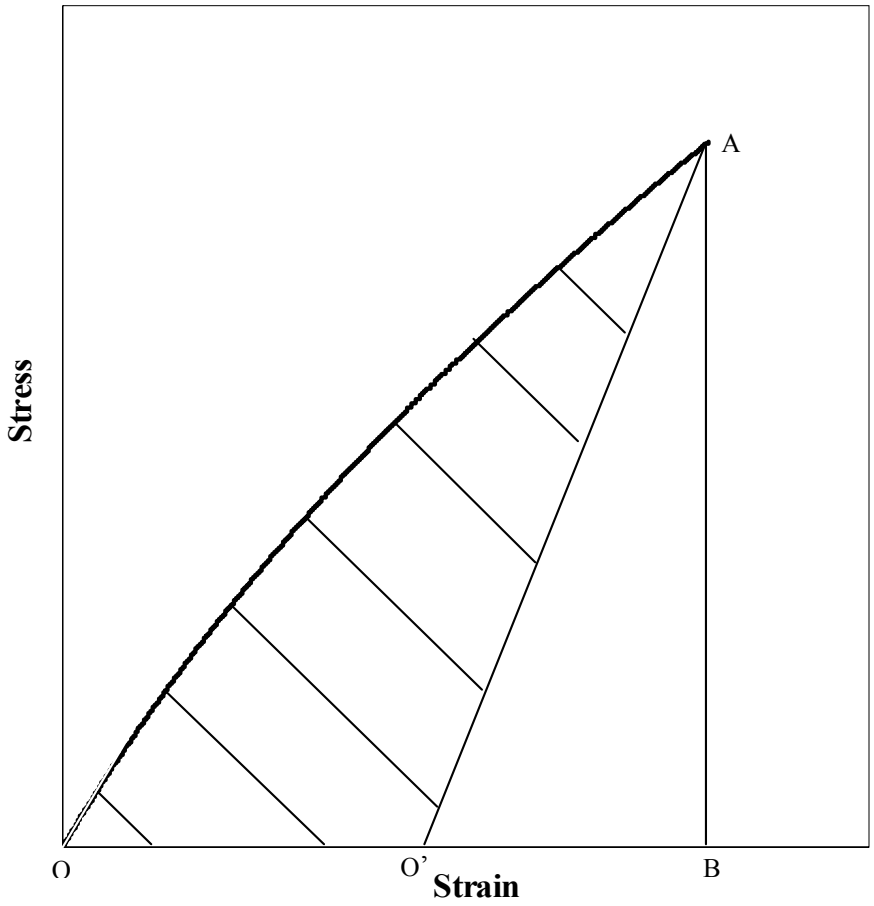

Fig. 20 Schematic description for the computation of the stored kinking nonlinear elastic energy U in Eq. (7). Here the slope of O'A is the theoretical Young's modulus and the area of OAB represents stored theoretical linear elastic strain energy. The area of OAB represents the total stored energy during loading. Thus U can be represented by area of OAO'.

Table 2. Summary of the estimated V_{IKB} from Eqn. (6) and (10) for FG and CG Ti_3SiC_2. These were obtained using $\gamma_c = 0.07$, $\nu = 0.2$, $b = 1.54$ Å and $D = 22$ Å, and $G = c_{44} = 142$ GPa [28]. σ in the table is the applied stress and τ is shear stress, assuming $\tau = \sigma / 2$. 2α is taken to be the average width of the grains as determined experimentally [57, 58]. 2β was from Eq. 3. See text for how to obtain N_k, U and V_{IKB}

σ (MPa)	τ (MPa)	2α (μm)	2β (μm)	N_k $(m)^{-3}$	U (kJ/m^3)	V_{IKB} [Eq.10]	V_{IKB} [Eq. 6]
Coarse-grained Ti_3SiC_2							
100	50	36	0.07	$3.7x10^{15}$	47	0.002	0.014
200	100	36	0.15	$5.2x10^{15}$	134	0.012	0.021
245	123	36	0.18	$5.6x10^{15}$	177	0.020	0.023
Fine-grained Ti_3SiC_2							
365	183	3	0.022	0.35×10^{18}	112	0.0016	0.009
625	313	3	0.037	0.9×10^{18}	487	0.012	0.019
915	458	3	0.055	1.7×10^{18}	1,330	0.047	0.033
985	500	3	0.059	2.0×10^{18}	1,650	0.063	0.037

Table 3. Summary of the estimated V_{IKB} from Eqs. (6) and (10) for graphite. These were obtained using $\gamma_c = 0.06$, $\nu = 0.3$, **b** = 1.42 Å and D = 23 Å, c_{44} = 4.5 GPa [16]. σ applied normal stress and τ is shear stress, assuming $\tau = \sigma / 2$. 2α is obtained from the peak broadening of X-ray results [79]. 2β is from Eq. 3. See text for how to obtain N_k, U and V_{IKB}

σ (MPa)	τ (MPa)	2α† (μm)	2β (μm)	N_k $(m)^{-3}$	U (kJ/m^3)	V_{IKB} [Eq.10]	V_{IKB} [Eq. 6]
36	18	0.023	0.005	$3.2x10^{20}$	48	0.0066	0.038
50	25	0.023	0.007	$4.4x10^{20}$	91	0.017	0.039
63	31.5	0.023	0.009	$6.2x10^{20}$	161	0.039	0.055
75	37.5	0.023	0.01	$8.3x10^{20}$	256	0.073	0.075

we express the stored kinking nonlinear elastic energy per unit volume during the loading as:

$$U \approx \frac{Gb^2}{2} \pi 2\beta N_o = \pi\beta N_o G b^2 \tag{7}$$

where N_o is the number of dislocation loops per unit volume, and b is the magnitude of the Burger's vector. The number of IKBs per unit volume, N_k, can be related to N_o as:

$$N_k = \frac{D}{2\alpha} N_0 \tag{8}$$

where D is the spacing of the loops in the IKB and 2α is the length of the IKB (Fig. 5a). Furthermore, it is assumed that to a first approximation, we may idealize the shape of the IKB as a cylinder with diameter 2β and height 2α. The volume fraction of material transformed to IKB can then be related to N_k as:

$$V_{IKB} = 2\pi\alpha\beta^2 N_k \tag{9}$$

Combining Eqs. (7) to (9) yields the desired expression to compute the volume fraction of IKBs from U, which in turn is obtained from the measured stress-strain curves. In other words:

$$V_{IKB} \approx \frac{2\beta D}{Gb^2} U \tag{10}$$

The values of the V_{IKB} of Ti_3SiC_2 and graphite estimated using equation (10) are also presented in Figs. 19a, 19b and 19c and summarized in Tables 2 and 3 along with the results from Eq. 6. It is seen that the estimates from equations Eqs. 6 and 10 are quite consistent with each other, especially noting that these are order of magnitude estimates. The agreement in Figs. 19a, 19b and 19c has to be considered excellent, considering the many simplifying assumptions made in deriving Eqs. 6 and 10. It is particularly noteworthy that these results are consistent over the entire range in the grain sizes (three orders of magnitude) in the materials considered here and the very different bonding in each solid.

A striking feature of the results shown in Figs. 19a, 19b and 19c is that a universal trend for the evolution of the V_{IKB} as a function of the imposed stress, σ, appears to emerge from all the plots. In general it is seen that at low σ's, V_{IKB} is low and increases slowly with increasing stress. At moderately high σ's the V_{IKB} increases sharply with stress, and is by reflected a marked increase in the slope of the curves shown in Figs. 19a, 19b and 19c. The transition between these two regimes appears to be a strong function of microstructural features such as the grain size in the sample.

Finally, at large stress levels, there has to be a decrease in the slope of these curves such V_{IKB} asymptotes to some value. This feature is not yet discernable in the plots shown in Figs. 19a, 19b and 19c, but is clearly expected because V_{IKB} can not keep increasing for ever with increasing stress levels. This is expected because with the production of IKBs, the effective grain size in the sample reduces and this in turn makes it harder to produce additional IKBs in the grain (according to Eq. 2). Note that the volume fraction of IKBs in the samples tested here is still quite low, only about 5-10% even in the highly loaded samples. Further increasing the imposed stresses on the samples, results in premature fracture or failure of the samples, and therefore it is not possible to extend experimentally the curves shown in Figs. 19a, 19b and 19c to higher stress levels. However, much higher stresses can have been achieved under spherical indenters [12-14].

2.4.2 Macroscale Constitutive Model

The microscale considerations described above form a basis on which we now build a macroscale constitutive model of KNE solids. In this first modeling study, we focus on a simple one-dimensional description of the stress-strain relations, while aiming to capture the rate-independent, fully reversible, discrete memory, hysteretic aspects of the mechanical behavior of these solids in complex loading-unloading histories (Fig. 21a).

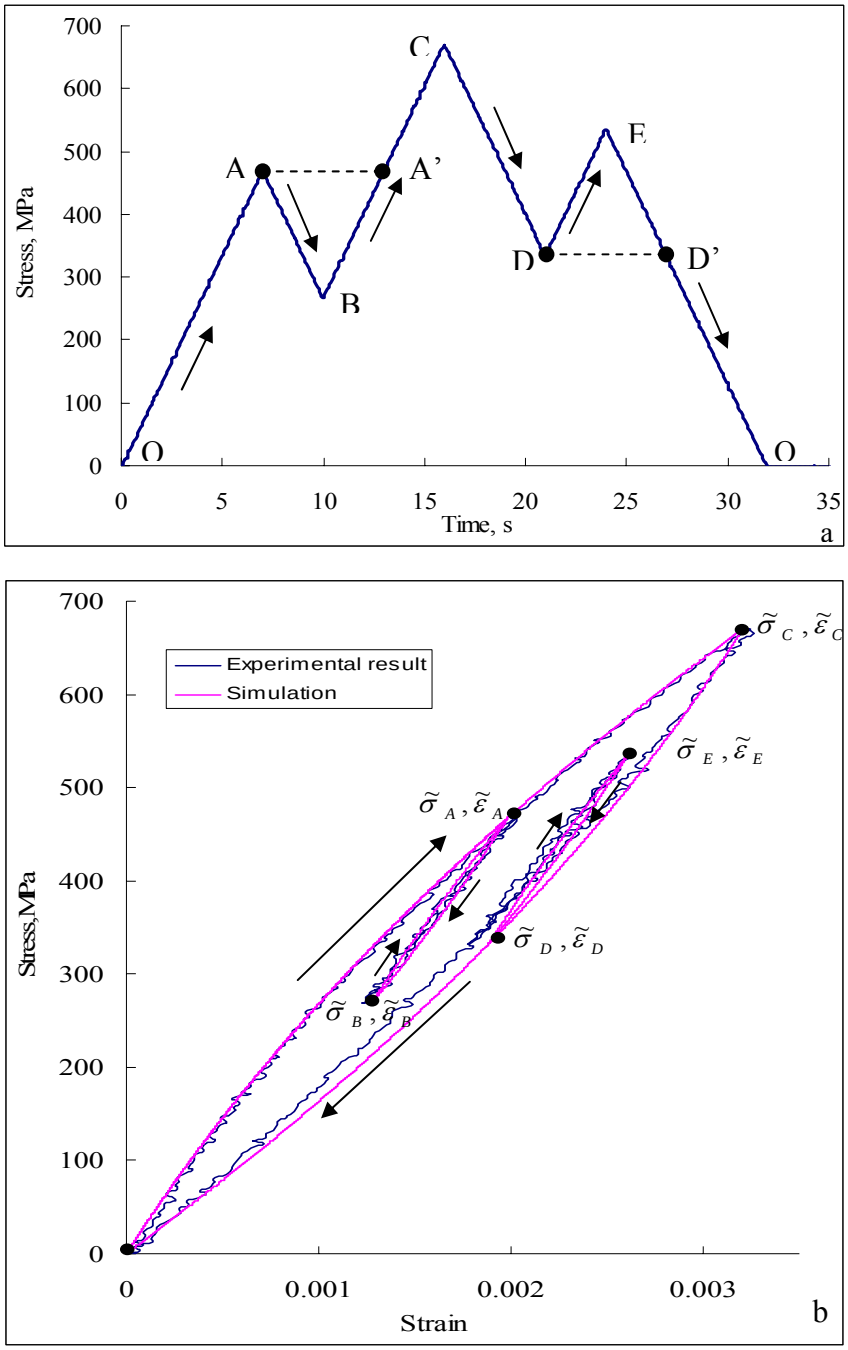

Fig. 21 Stress-strain response of fine-grained Ti_3SiC_2 in a complex loading-unloading condition. (a) Comparison of the stress-strain curves from the experiments and the model predictions. (b) The stress history provided as input to the model for the predictions shown in (a).

We start by recasting equation (4) as a constitutive equation for stress as:

$$\sigma = E\left(\varepsilon_{total} - \varepsilon_{IKB}\right) \tag{11}$$

Noting that the reversible kinking strain scales directly with the volume fraction of IKBs (Eq. 5), we expect to formulate an expression for ε_{IKB} as a function of the stress (as suggested by the various plots in Figs. 19a, 19b and 19c). However, our goal is to formulate an expression that will work for various loading and unloading segments in a complex loading-unloading cycle. To this end, we introduce a new stress parameter called effective stress, denoted by σ^*, which essentially captures the driving force for kinking or de-kinking (annihilation of existing IKBs). In the first loading of a virgin material (from an annealed condition), the effective stress would simply be the imposed stress. However, with complex loading histories, the effective stress will be defined as the difference of the stress and a stress memory variable (arising from discrete memory characteristics of KNE solids), and this will be discussed in detail later. We propose the following phenomenological expression for the relationship between kinking strain and the effective stress driving kinking:

$$\varepsilon_{IKB} = f(\sigma^*) = \varepsilon_{\max}\left(1 - e^{-\left(\frac{\sigma^*}{\sigma_o}\right)^M}\right) \tag{12}$$

where $\varepsilon_{\max}$ is the maximum axial strain that can be obtained through IKBs; as we discussed earlier it is given as γ_c/k corresponding to the theoretical limit when the IKB volume fraction reaches one. σ_0, and M are parameters that can be extracted from experimental data. The functional dependence embodied in Eq. 12 is shown in Fig. 22, and exhibits all of the desired features described at the end of the last section.

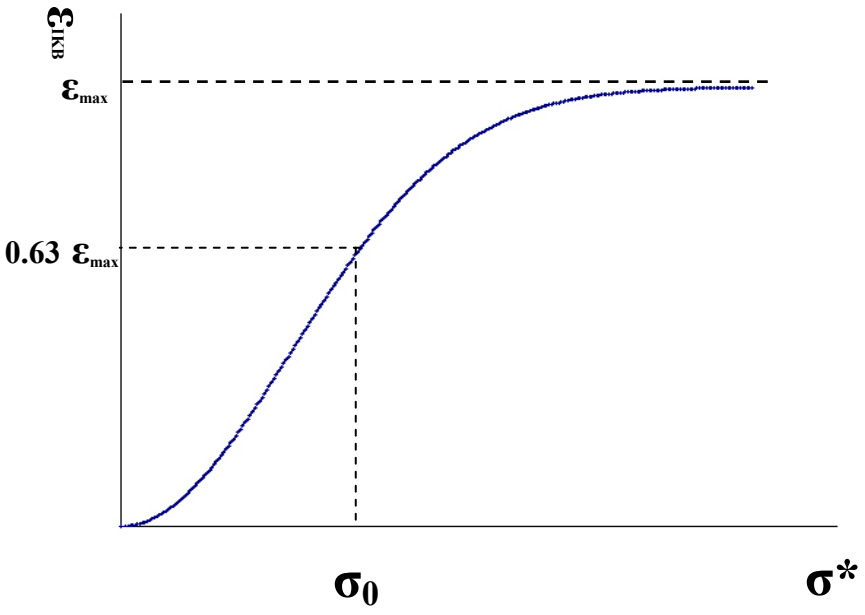

Fig. 22 The kinking related strain ε_{IKB} as a function of effective stress, σ^*. It shows that kinking is not favored at extremely low stress levels and at very high stress levels. Kinking reaches a saturation condition at high stress level.

σ_0 is a material constant that reflects the stress when the strain contributed by the IKB corresponds to about 63% of ε_{max}. In general, σ_0 is expected to be strongly influenced by the microstructure, especially the average grain size in the sample. The parameter M is a material constant that depends on microstructure, especially the orientation and grain distribution of crystals in the sample. Like shape parameter in Weibull distribution, M controls the formation rate of IKB as function of effective stress, σ^*. For randomly oriented polycrystal KNE solids, due to the high anisotropy in their plastic properties at the single crystal level and less of 5 independent slip systems, different grains have different local stress fields, at certain effective stress level, some grains may easily form IKBs (preferred orientation), some may not (hard orientation). The evolution of IKBs as function of effective stress in randomly oriented polycrystal material will follow the statistic rule. For materials with wide distribution of grain sizes and lattice orientations, this parameter is expected to take low numerical values.

To complete the model, we need to establish the relationship between the effective stress, σ^*, for kinking or de-kinking and the imposed stress, σ,. In a complex loading-unloading sequence, KNE solids exhibit discrete memory behavior, i.e. they remember the previous stress reversal points. We introduce the following dynamic lists of state variables to remember the discrete memory points. Let L = $\{(\sigma_k^l, \varepsilon_k^l)$; k = 0, 1, 2, ..., N$\}$ represent the relevant loading-unloading reversal points in the loading history of the sample, and UL = $\{(\sigma_k^{ul}, \varepsilon_k^{ul})$; k = 0, 1, 2, ..., M$\}$ denote

the unloading-loading reversal points. Note that these are dynamic lists, i.e. the elements of these lists change during deformation of the material. These lists have the following attributes:

1. For a virgin material (no loading history), both these lists have single elements (0,0). These lists will always contain this element. For example, when we start the loading sequence shown in Fig. 21a, the lists are initialized with (0, 0), as shown in Table 4 .
2. An element will be added to the appropriate list with every stress reversal. For example, if the sample is being subjected to a loading stress segment and experiences an unloading stress segment, then the stress and the strain at the point of stress reversal are added to the list L. Furthermore, the newly added element becomes the first element of the list. Therefore in the loading cycle shown in Fig. 21a, when the stress history experiences a reversal at point A, the element (σ_A, ε_A) is added to list L. Similarly, when there is a stress reversal at point B, the element (σ_B, ε_B) is added to list U (Table 4), because this stress reversal is from unloading to loading. The lists are similarly evolved at points C, D, and E.
3. In any intermediate loading or unloading segment of a complex loading sequence, one is likely to encounter the same stress and strain condition that corresponds to a previously established memory point. For example, in going from point B to point C, we will encounter point A (labeled as A' in Fig. 21a). In such a situation, we modify the lists by removing the first elements of both

lists L and UL. For example, when we reach the point A, the element (σ_A, ε_A) is removed from list L and the element (σ_B, ε_B) is removed from list U (see Table 4). This is because these memory points have no consequence on the subsequent behavior of the material. A similar evolution of the lists occurs at D' (i.e. we go through point D a second time in going from point E to O).

4. With the memory lists in place, the strain corresponding to any imposed stress is simply given by

$$\begin{aligned} &\text{In a loading stress segment :} && \varepsilon_{IKB} = \varepsilon_1^{ul} + f(\sigma - \sigma_1^{ul}) \\ &\text{In an unloading stress segment :} && \varepsilon_{IKB} = \varepsilon_1^{l} - f(\sigma_1^{l} - \sigma) \end{aligned} \qquad (13)$$

Where $(\sigma_k^{ul}, \varepsilon_k^{ul})$ is the first element of the list UL and $(\sigma_k^{l}, \varepsilon_k^{l})$ is the first element of the list L.

Figures 21b, 23a and 23b show a comparison of the experimental data with the corresponding predictions from the model described above for fine-grained Ti_3SiC_2 and graphite. It is seen that the simple model described here captures quite well the mechanical response of KNE solids in complex loading histories. It is noteworthy that the model has only three parameters, of which two are estimated from microscale considerations of the kinking theory, and only one is a curve-fitting parameter. Also, the curve-fitting parameter is established from the monotonic loading response on the material, and it is seen that there is no need to introduce any new parameters in the model to capture the behavior of the KNE solids during unloading or any complex loading-unloading sequence.

Table 4. The evolution of the discrete memory lists in the complex loading history shown in Fig. 21b.

Loading segment	**L**	**UL**
O- A	{(0,0)}	{(0,0)}
A - B	$\{(\sigma_A, \varepsilon_A), (0,0)\}$	{(0,0)}
B – A’	$\{(\sigma_A, \varepsilon_A), (0,0)\}$	$\{(\sigma_B, \varepsilon_B), (0,0)\}$
A’- C	{(0,0)}	{(0,0)}
C - D	$\{(\sigma_C, \varepsilon_C), (0,0)\}$	{(0,0)}
D - E	$\{(\sigma_C, \varepsilon_C), (0,0)\}$	$\{(\sigma_D, \varepsilon_D)\ (0,0)\}$
E – D’	$\{(\sigma_E, \varepsilon_E),\ (\sigma_C, \varepsilon_C), (0,0)\}$	$\{(\sigma_D, \varepsilon_D)\ (0,0)\}$
D’–O	$\{(\sigma_C, \varepsilon_C), (0,0)\}$	{(0,0)}

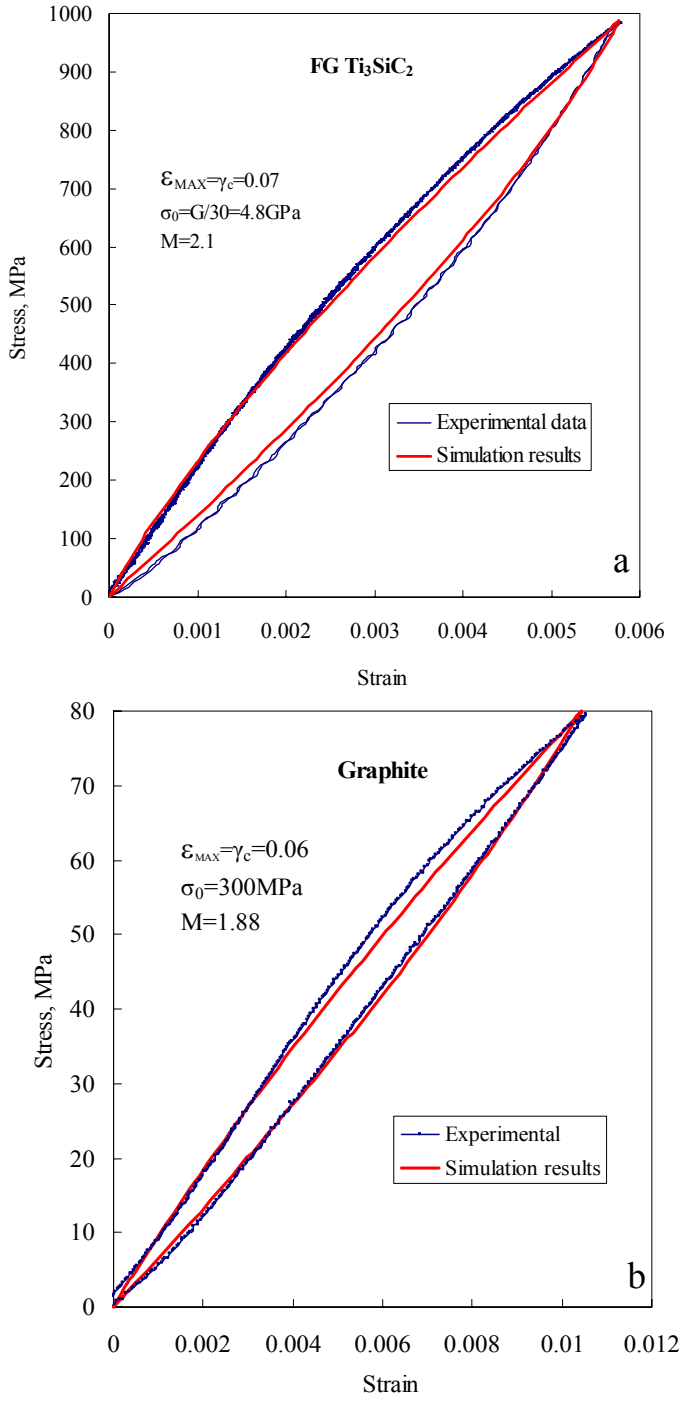

Fig.23 The comparison of simulation results and experimental data in compression for. (a). FG Ti_3SiC_2 at 1 GPa. (b). Graphite at 80 MPa.

2.5 Summary and Conclusions

In this chapter we present our recent work on the room temperature compressive behavior of KNE solids. A kinking-based model that explains the response of polycrystalline KNE samples to mechanical stress. The model also can account for many aspects of the deformation. The key to the model is the identification of a fully reversible hysteretic element – labeled incipient kink bands - comprised of near parallel dislocation walls that are strongly attractive. As long as the stress level is insufficient to sunder the IKBs the mechanical response is characterized by fully reversible hysteretic loops.

The microscale considerations based on the Frank and Stroh theory of kinking provide reasonable predictions for the volume fraction of the material transformed to IKBs in three different KNE solids. These estimates were obtained using two completely different strategies. The fact that these estimates were consistent with each other significantly strengthens our assertion that the nonlinear, fully reversible, rate-independent, hysteretic, and shape-memory characteristics of KNE solids are indeed attributable to the formation and annihilation of incipient kink bands.

It has also been demonstrated that the elastic response of KNE solids can be captured by a simple phenomenological description that contains only three

parameters. Of these three parameters, the values of two can be established from microscale considerations of the theory of kinking, and only one needs to be established using the measured stress-strain response in monotonic loading. Once these parameters are established, however, the model can provide reliable predictions of the stress-strain response of the KNE solids in any complex loading history comprising arbitrary loading and unloading segments.

Because the dislocations are confined to the basal planes, they do not entangle, and thus can move reversibly over relatively large distances. This feature results in the dissipation of substantial amounts of energy per cycle and accounts for the stress dependent of energy dissipation. The proposed mechanism is valid over a wide range of stresses as seen from the work dissipated vs. stress plots that show very good agreement over more than 4 orders of magnitude, between nanoindentations and simple compression experiments.

3. Compressive Creep of Fine and Coarse-Grained Ti_3SiC_2 in Air in the 1100 to 1300 °C Temperature Range

3.1 Introduction

Since Ti_3SiC_2 was synthesized as a fully dense, single-phase bulk material, it has been established that this ternary carbide exhibits an unusual combination of properties [32-42], such as high specific stiffness [40] with ease of machinability [34]; exceptional damage tolerance; good thermal shock [34,38], as well as good oxidation [38] and fatigue resistances [32]. At room temperature, favorably oriented microstructures exhibit ductile behavior [38].

The mechanical response of Ti_3SiC_2 and by extension the other $M_{n+1}AX_n$ phases [43] (where M is a transition metal, A is an A group element and X is carbon and/or nitrogen) can be traced to the following three facts: i) Basal slip, and only basal slip, is operative at all temperatures [36, 38]. No other dislocations but perfect, mixed basal plane dislocations are observed by TEM [35, 36, 38]. ii) Because of their high c/a ratios, twinning is unlikely, and has never been observed. Instead, deformation occurs by a combination of glide and formation of kink bands and delaminations within individual grains [35-38]. iii) Because they are confined to the basal planes, the dislocations arrange themselves either in arrays (pileups) on the same slip plane, or in walls (low or high angle grain boundaries) normal to the arrays

[35, 36]. Thus, at no time are the five independent slip systems required for ductility operative [44, 45].

One of the major consequences of this plastic anisotropy is the development of large internal stresses in grains that are not well oriented to the applied stress – so called hard grains. In that respect the response of Ti_3SiC_2 to stress is comparable to that of ice [56]. Both solids fail in a brittle manner if loaded rapidly; if loaded slowly, however, they can be quite plastic. In both materials, the mechanical response is dictated by a competition between the rate at which the internal stresses accumulate and the rate at which they can be relaxed.

Tensile creep tests performed on FG and CG Ti_3SiC_2 microstructures in the 1000 - 1200 ^{o}C temperature range exhibit primary, secondary and tertiary creep regimes [57, 58]. During the short primary creep stage, the deformation rate decreases rapidly. This is followed by a secondary creep regime in which the creep rate, although not truly reaching a constant level, does not change significantly over a wide range. This secondary or minimum creep rate, $\dot{\varepsilon}_{\min}$, is thermally activated and can be described by:

$$\dot{\varepsilon}_{\min} = \dot{\varepsilon}_0 A \left(\frac{\sigma}{\sigma_0} \right)^n \exp\left(-\frac{Q}{RT} \right) \tag{14}$$

where A, n and Q are, respectively, an independent dimensionless constant, stress exponent, and activation energy. $\dot{\varepsilon}_0$ and σ_0 define the units used and are, respectively, 1 s^{-1} and 1 MPa. The activation energy in tension is independent of grain size and equal to ≈ 450 kJ/mol; n is 1.5 and 2 for the FG and CG microstructures, respectively [57, 58].

Tensile creep occurs by a combination of plastic deformation and damage accumulation. Plastic deformation is the dominant mechanism during the primary and secondary creep regimes. Tensile creep results and those obtained from tensile stress relaxation tests are in good agreement with each other suggesting that the same atomic mechanism is responsible for the plastic deformation in all cases [57, 58]. Furthermore, the results of strain-transient dip tests [57, 58] provide strong evidence for the presence of large internal stresses during tensile creep. These stresses are responsible for considerable recoverable strains upon unloading, and are believed to be responsible for the initiation of intergranular microcracks and the acceleration of creep during the tertiary regime.

In chapter 2 we reported that macroscopic polycrystalline Ti_3SiC_2 cylinders can be compressed, at room temperature, to stresses up to 1 GPa, and fully recover upon the removal of the load [11]. This phenomenon was attributed to the fully reversible formation and annihilation of incipient kink bands, IKBs, defined as near parallel dislocation walls of opposite polarity that remain attached, and are thus

attracted to each other. Removal of the load allows the walls to collapse and the IKB to be totally eliminated.

More germane to this work, however, and discussed in more detail in Ch. 4, was that at temperatures higher than 1000 °C the walls bounding the IKBs become parallel and their mutual attraction is weakened or eliminated, and upon the removal of the load, part of the deformation becomes plastic or irreversible . Furthermore, once the walls separate some distance, other IKBs can nucleate within the area between the now parallel detached walls. Once detached, the walls are mobile until they encounter an obstacle, such as a grain boundary or another wall. The coalescence of walls from the same or adjacent sources results in kink boundaries. In other words, large grains are broken into smaller ones, which result in grain size refinement and consequently in cyclic hardening at temperature (see Ch. 4).

Although significant progress has been achieved in understanding the mechanical behavior of Ti_3SiC_2 as a function of temperature and grain size, as far as we aware, there are no reports on its creep response to compressive loads. The purpose of this chapter is to report on that aspect of its deformation in air as a function of grain size, temperature and stress.

3.2 Experimental Procedure

The processing details can be found elsewhere [40]. Briefly, the specimens were produced by reactive hot isostatic pressing (HIPing) a stoichiometric powder mixtures of titanium (-325 mesh, 99.5%, Alfa Aesar, Ward Hill, MA), silicon carbide (- 400 mesh, 99.5%, Atlantic Engineering Equipment, Bergenfield, NJ) and graphite (- 300 mesh, 99%, Alfa Aesar, Ward Hill, MA). HIPing at 1450 °C at a pressure of 40 MPa for 4 h resulted in a fine-grained, FG, microstructure; HIPing at 1600 °C , 40 MPa for 6 h resulted in a coarse-grained, CG, microstructure. The sintered Ti_3SiC_2 samples were obtained from 3-ONE-2 LLC, Voorhees, NJ.

Tests were performed using cylindrical shaped specimens (9.8 mm in diameter and 30 mm in height) with a gauge length of 25 mm. Samples were electro-discharge machined and tested with no further surface preparation. Compressive creep and relaxation tests were performed in air using a hydraulic testing machine (MTS 810, Minneapolis, MN), supplied with a controller (Microconsoler 458.20, MTS, Minneapolis, MN) that allowed tests to be run either in displacement or load control mode. In all tests, a preload that corresponded to a stress, σ, of 1 ~ 2 MPa was applied to keep the samples aligned. Strains were measured by a capacitance high-temperature MTS extensometer, with 5% capacity; the force was measured by using a 100 KN load cell (MTS, Minneapolis, MN).

The creep tests were performed at 1200 and 1300 °C using constant loads that corresponded to stresses that ranged from 25 to 100 MPa. All samples were heated to the testing temperature and held at that temperature for about 30 minutes before the load was applied. Most were run up to a certain strain level, that never exceeded ≈ 4% strain, before aborting the runs by unloading the samples.

The stress relaxation tests, SRT, were performed at 1100, 1200 and 1300°C. The load was applied at a constant cross-head displacement (CHD) rate up to the desired load, at which time, the cross-head motion was abruptly stopped and the stresses and strains were monitored as a function of time. The instantaneous strain rate changes during the test were obtained by differentiation of the strain vs. time curves; those values were then matched with the stress level being monitored at the same time.

After the completion of the creep tests, the surfaces that were parallel to the applied load were ground and polished for optical microscopy (OM) and field emission scanning electron microscopic (FESEM) analysis. To expose the grains, some polished samples were etched using a 1:1:1 by volume $HF:HNO_3:H_2O$ solution.

3.3 Results

The CG microstructure consisted of large plate-like grains 50-200 μm in diameter and 5-20 μm thick [57, 58]. These in turn were surrounded by areas in which the grains were much smaller. The FG microstructure consisted of equiaxed grains 3-5 μm in diameter [57, 58]. Both FG and CG samples contained ≈ 2 vol. % SiC and TiC spherical inclusions that were homogeneously distributed through the sample; their size did not exceed ≈ 2 μm in diameter.

Typical compressive creep curves (creep strain, ε, vs. time, t) of CG and FG samples tested at 1300 °C and 68 MPa are shown in Fig. 24a. It clearly shows at 1300°C and 68 MPa, the FG sample is much more deformation resistant than its CG counterpart. Also the initial strain of FG Ti_3SiC_2 is smaller than CG Ti_3SiC_2 (inset in Fig. 24a). The strain rate, $\dot{\varepsilon}$, versus t curves for the same set of data are plotted in Fig. 24b. Three stages are distinguishable:

a) An initial transient regime in which $\dot{\varepsilon}$ gradually decreases with t (inset in Fig. 24b).

b) A secondary creep regime in which $\dot{\varepsilon}$ is more or less constant with time. Since this region corresponds to the minimum creep rate, $\dot{\varepsilon}_{min}$, it will henceforth be referred as the minimum creep rate region. The values of $\dot{\varepsilon}_{min}$ were calculated from

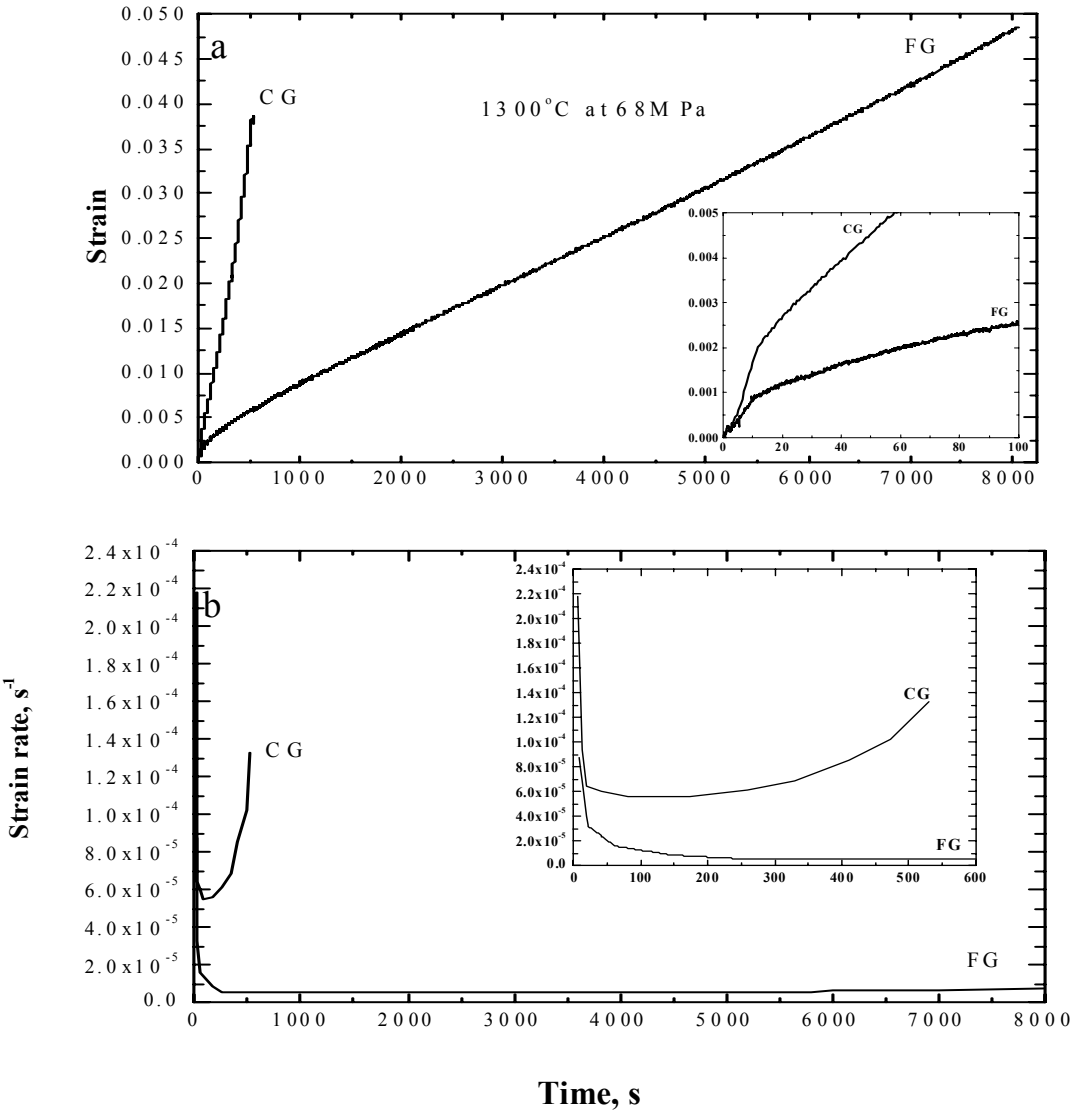

Fig. 24 Compressive creep curves of FG and CG Ti_3SiC_2 at 1300 °C and 68 MPa. a) compressive strain and b) strain rate of FG and CG samples tested at 1300 ◦C. (b) is obtained by differentiation of curves shown in (a). Insets are enlargements of the initial parts of plots shown in (a) and (b).

the slopes of the best fitting straight lines to the creep curves at the beginning of this regime.

c) A tertiary creep regime in which $\dot{\varepsilon}$ increases until failure.

Log-log plots of $\dot{\varepsilon}_{min}$ versus σ as a function of temperature, T, for the FG and CG samples are shown in Figs. 25 and 26, respectively. These results clearly show a transition in compressive creep behavior at around 70 MPa. This phenomenon is more obvious in FG than in CG Ti_3SiC_2. Also included on Fig. 25 are the compressive SRT results of sintered Ti_3SiC_2 and the tensile creep results of Radovic et al. [57, 58]. Clearly, there is magnitude difference of $\dot{\varepsilon}_{min}$ between sintered Ti_3SiC_2 and HIPed Ti_3SiC_2. This is also true between the tensile and compressive results.

A bilinear regression analyses (with 95 % confidence boundaries) was carried out on the logarithmic form of Eq. 14 for both FG and CG Ti_3SiC_2. The analyses was carried out assuming there have two regimes, high stress regime (σ's >70 MPa) and low stress regime (σ's < 70 MPa). Results in the values are shown in Table 5 for the CG and FG samples. The tensile results on similar microstructures are those of Radovic et al. [57, 58]. At low stress the n of FG Ti_3SiC_2 is 1.9, at high stress the value of n increases to 3.7, clearly indicating a change in the creep mechanism(s). The activation energy of FG Ti_3SiC_2 in compression is comparable with tensile results, but the activation energy of CG Ti_3SiC_2 is much higher compared with the tensile results (Table 5).

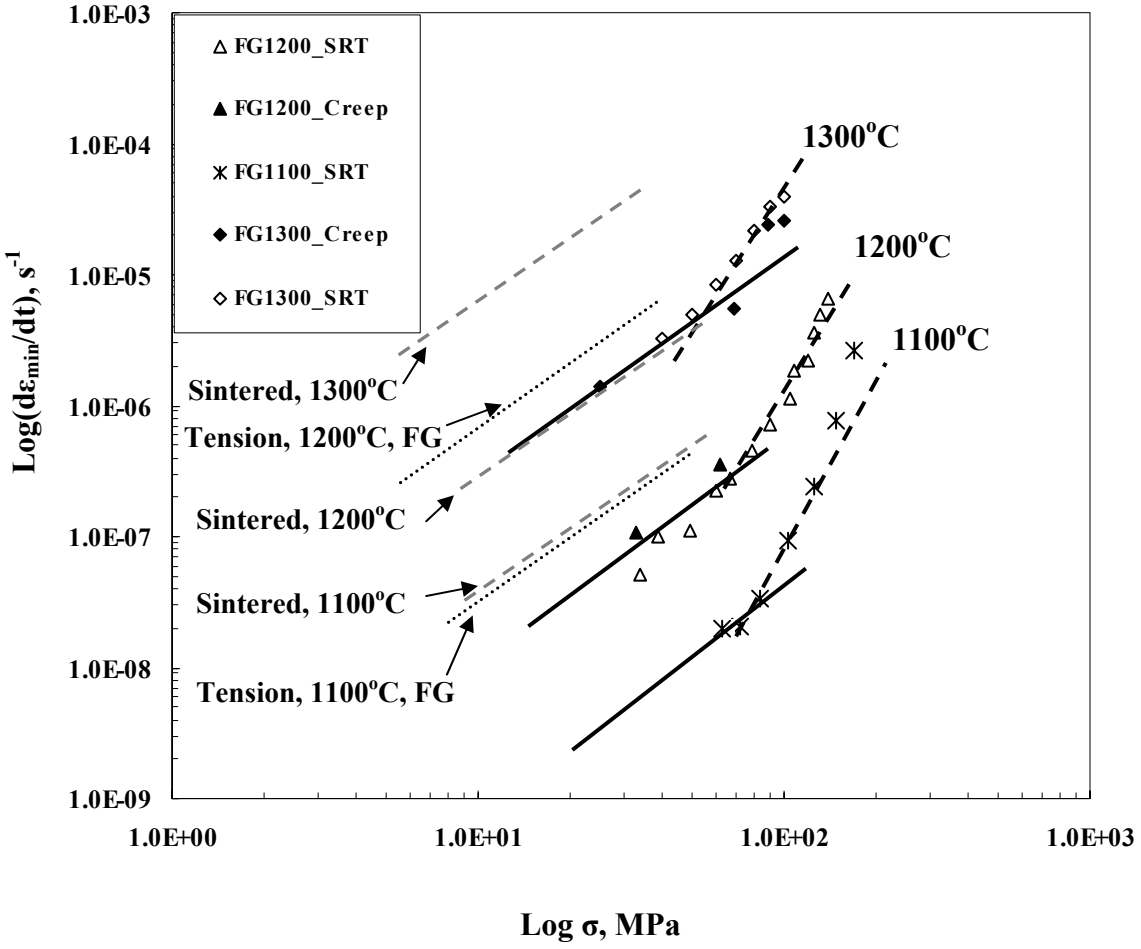

Fig. 25 Log-log plot of $\dot{\varepsilon}_{min}$ vs. σ as a function of T and testing technique of FG Ti_3SiC_2. Solid black lines are results of a bilinear regression for low stress regime. The dashed black lines are results a bilinear regression for high stress regime. The dotted gray lines are results of tensile tests at 1100 ^oC and 1200 ^oC. The dashed gray lines are SRT results of sintered Ti_3SiC_2 at 1100 ^oC, 1200 ^oC and 1300 ^oC in compression.

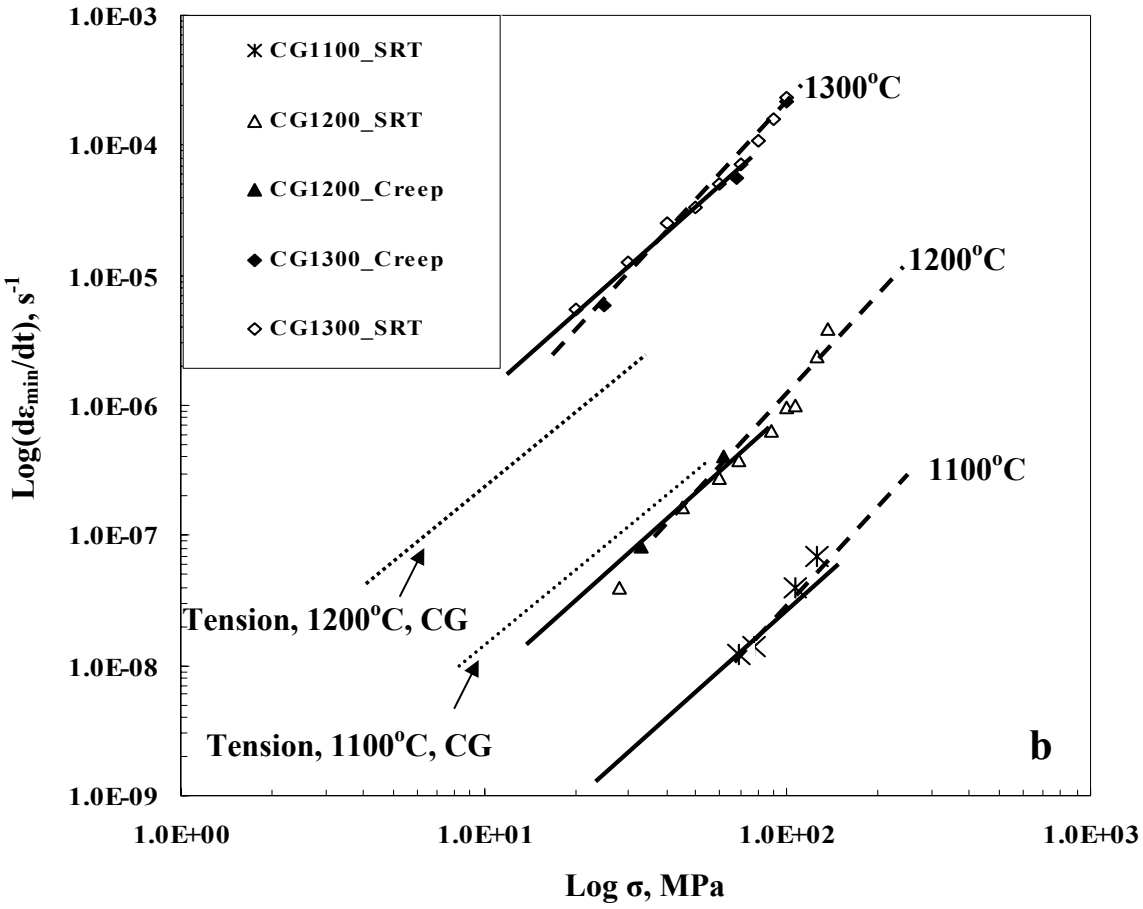

Fig. 26 Log-log plot of $\dot{\varepsilon}_{min}$ vs. σ as a function of T and testing technique of CG Ti_3SiC_2. Solid black lines are results of a bilinear regression for low stress regime. The dashed black lines are results a bilinear regression for high stress regime. The dotted lines are results of tensile tests at 1100 ^{o}C and 1200 ^{o}C.

Table 5: Summary of creep results for Ti_3SiC_2.

	ln A		n		Q (kJ/mol)		$\dot{\varepsilon}_{min}$ (s)$^{-1}$ at 1200 °C and 50 MPa	Ref.
	σ<70 MPa	σ>70 MPa	σ<70 MPa	σ>70 MPa	σ<70 MPa	σ>70 MPa		
Compression CG	44	42	2.1	2.5	835±39	812±49	2.3 x 10^{-7}	This work
Compression FG	20	12	1.9	3.7	537±31	518±47	2.2 x 10^{-7}	This work
Tensile CG	17		2.0		458±12		3.5 x 10^{-6}	Ref. 18
Tensile FG	19		1.5		445±10		1.0 x 10^{-5}	Ref. 16

The SRT results from 170 MPa - for both microstructures - at 1100 °C and 1200 °C are shown in Figs. 27 and 28, respectively. These results clearly show that the instantaneous strains of the FG samples upon loading are smaller than those of the CG samples. The stress relaxations rates for both microstructures are slower at 1100 °C (Fig. 27) than at 1200 °C (Fig. 28). At 1100°C, the σ vs. t curves are almost superimposable and thus appears to be independent of microstructure (Fig. 27). At 1200 °C, the stress relaxation of the CG sample, while initially faster than the FG one, is ultimately slower, but not by much (Fig. 28). The effect of temperature, however, is more important on the shape of the curves than the microstructure.

The strain rates and corresponding stresses obtained from the SRT at 1200 °C are plotted in Figs. 25 and 26 for the FG and CG samples, respectively. At low strain

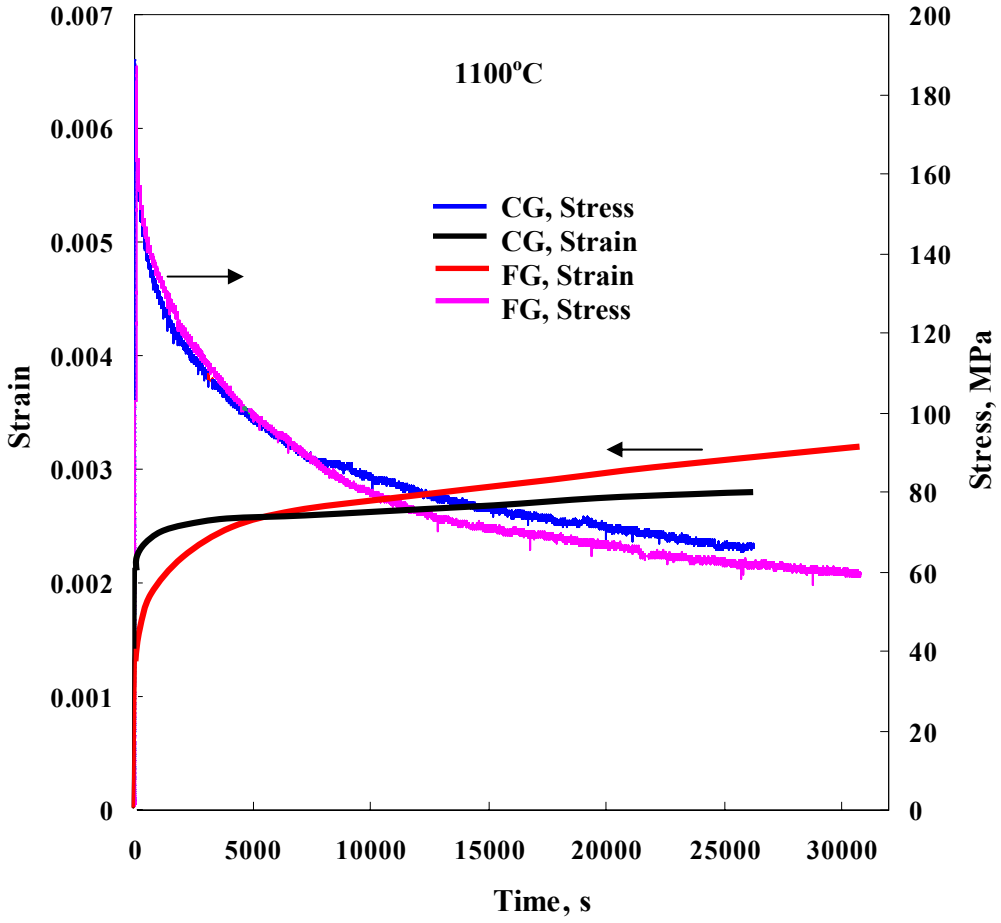

Fig. 27 Strain and stress versus time curves of SRT tests at 1100 °C for both CG and FG Ti_3SiC_2.

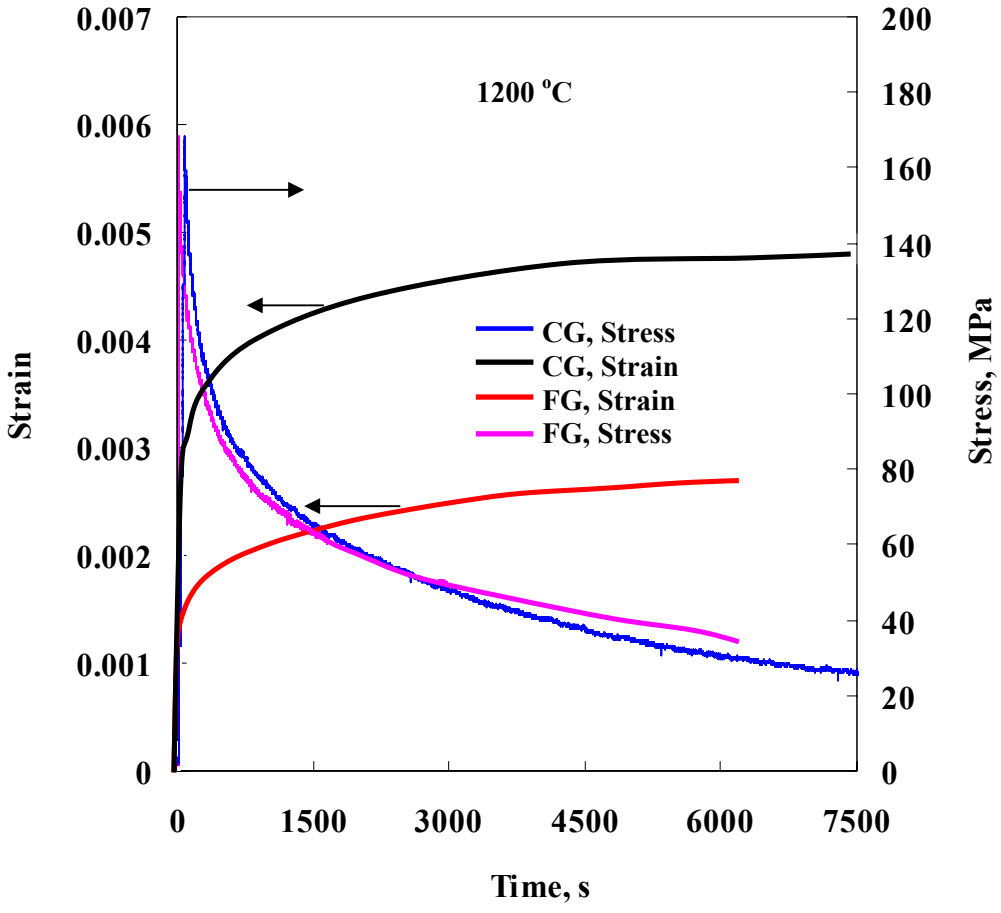

Fig. 28 Strain and stress versus time curves of SRT tests at 1200°C for both CG and FG Ti_3SiC_2.

rates, the compressive SRT results are in good agreement with the creep results. At $\sigma > 70$ MPa, however, the strain rates increase much more rapidly with stress than at the lower stresses, especially for FG samples.

Stress-strain curves of initial loading part of creep tests for CG and FG samples at 1200 °C and 1300 °C at different stresses are shown in Fig. 29. Here again, the initial or instantaneous strains of the FG samples are smaller than their CG counterparts. This is especially true at higher temperatures and higher stresses (Fig. 30a). Based on these results, there is little doubt that at high temperature and/or high stresses, the FG samples are *more* deformation resistant than the CG ones. For example at 100 MPa and 1300 °C, CG Ti_3SiC_2 failed after 70 s (Fig. 30a); the failure strain was ≈ 4.3%. Under the same conditions, the FG sample was still in the secondary creep stage after more than 600 s at which time the strain was < 2% (Fig. 30a).

Select but typical creep curves for the CG and FG Ti_3SiC_2 at 1200 °C and 1300 °C are shown in Figs. 30a, 30b, 30c and 30d. Clearly, at higher temperatures and /or higher stresses, the $\dot{\varepsilon}_{\min}$ of FG sample's is much smaller than the CG's. As the temperatures and stresses are reduced, the creep response of both microstructures becomes quite comparable (Figs. 30c and 30d). At 1200 °C and 33 MPa, after nearly 10 hours test, the creep curves of the FG and CG samples are almost superimposable; after that the strain of the FG sample is higher (Fig. 30d). Compare

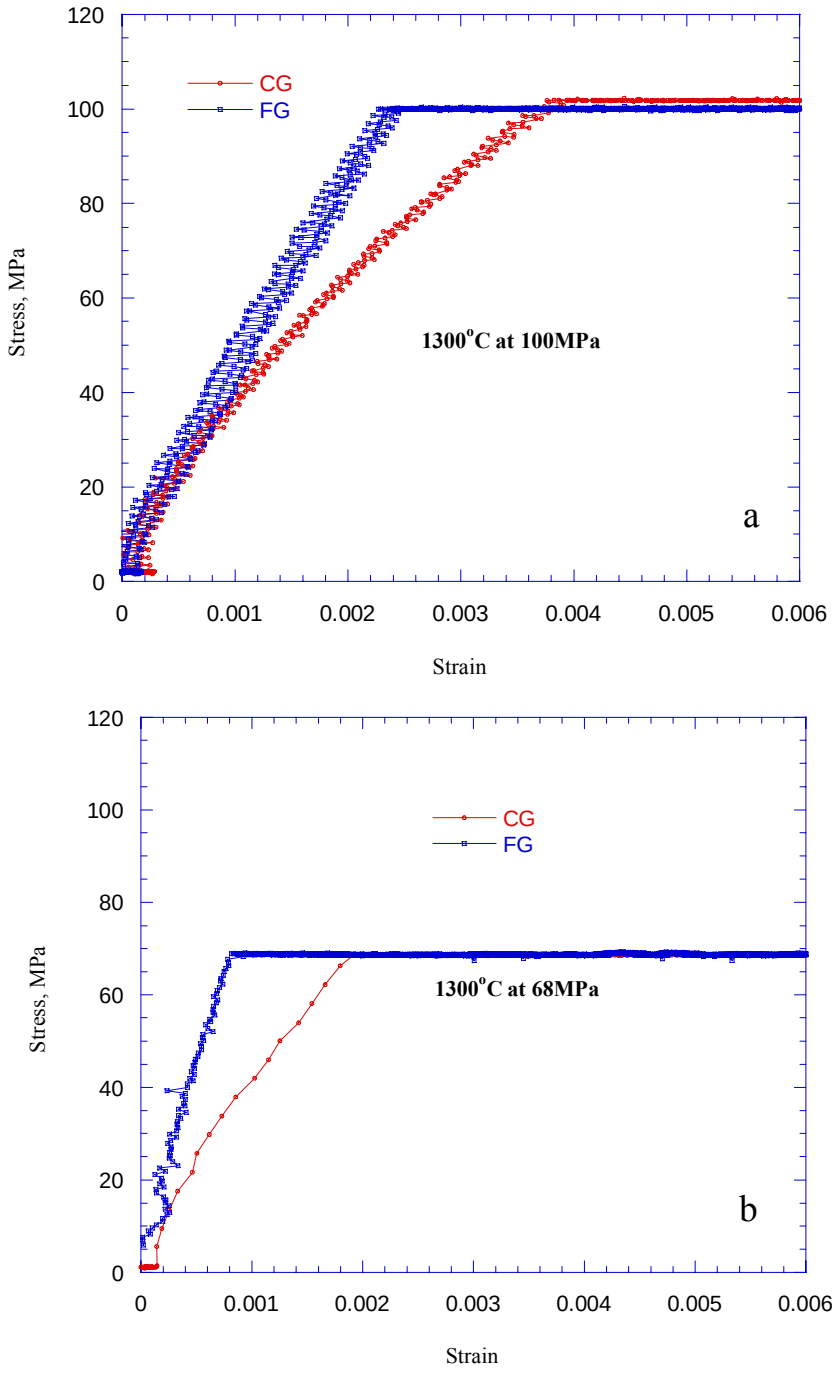

Fig. 29 Stress-strain curves of initial loading part of creep tests for CG and FG samples. a) At 1300 °C and 100 MPa for CG and FG samples. b) 1300 °C and 68 MPa.

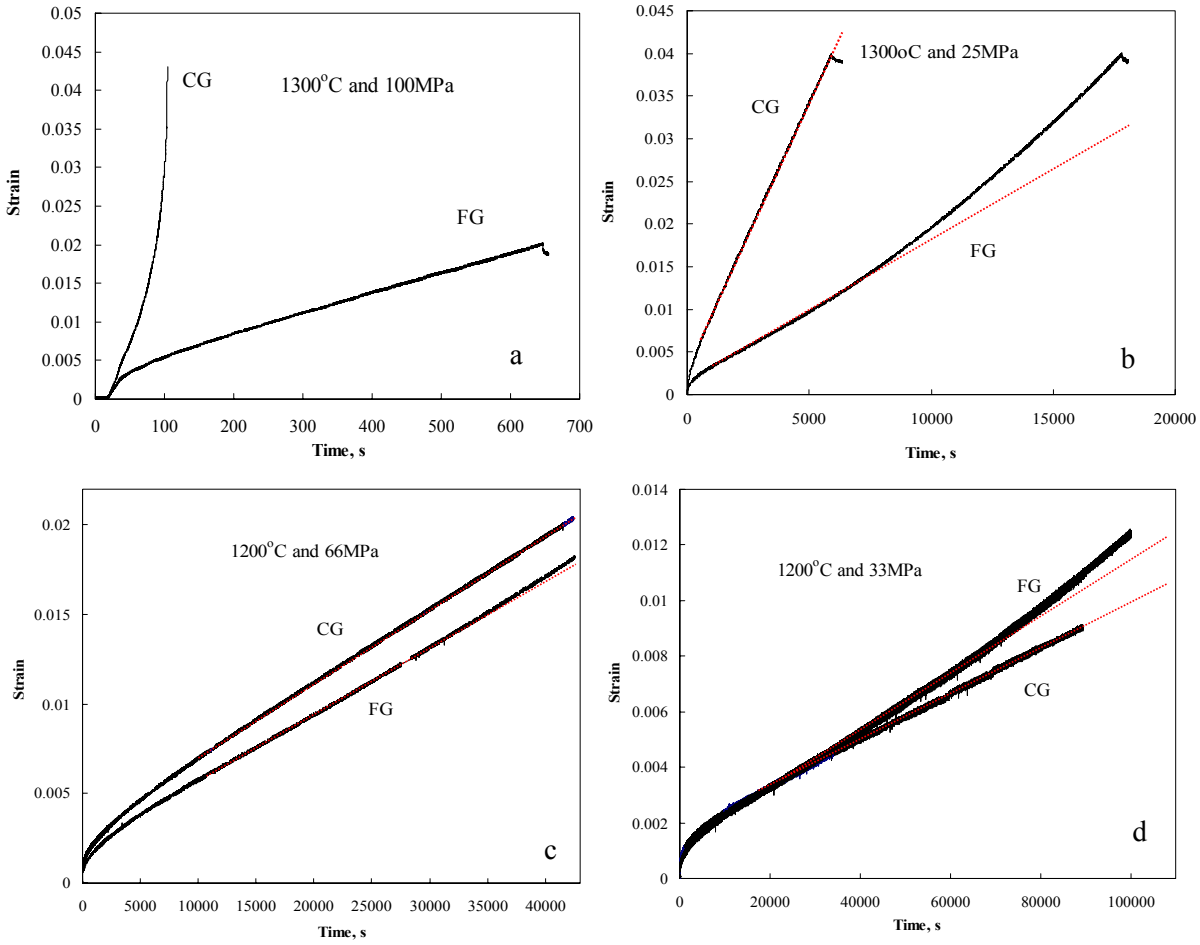

Fig. 30 Strain versus time at different temperature and creep stress for CG and FG samples. a) At 1300 °C and 100 MPa for CG and FG samples. b) 1300 °C and 25 MPa. c) 1200 °C and 62 MPa. d) 1200 °C and 32 MPa. The slope of dotted line in (b), (c) and (d) represent the minimum creep rate $\dot{\varepsilon}_{\min}$

the dotted line superimposed with the strain versus time curves in Fig. 30b, 30c and 30d, the slope of the dotted line means the secondary creep rate or $\dot{\varepsilon}_{min}$ of the correspondent creep test. It clearly shows the FG samples enter the tertiary creep regime at relatively smaller strain than CG's. At 1200 °C and 62 MPa, after 10 hours compressive creep, the FG sample starts the tertiary creep with 1.5 % deformation, but the CG sample is still in secondary creep regime after 12 hours test and > 2 % deformation. It clearly shows that at the lower stresses, the CG Ti_3SiC_2 can accommodate more deformation than FG Ti_3SiC_2 before entering the tertiary creep (Fig. 30b, 30c and 30d).

3.4 Discussion

The most important results of this work are the strong dependence of $\dot{\varepsilon}_{min}$ on stress state, processing method and the obvious change in deformation mechanism at σ's > 70 MPa. Figures 25 and 26 clearly show the $\dot{\varepsilon}_{min}$ in compression are more than an order of magnitude lower than in tension. At 1200°C and 50 MPa, $\dot{\varepsilon}_{min}$ for the FG samples in tension is ≈ 1 x10^{-5} s^{-1}; the corresponding $\dot{\varepsilon}_{min}$ in compression 3.5 x 10^{-7} s^{-1}. In other words, Ti_3SiC_2 is more creep resistant in compression than in tension. This conclusion is valid despite the fact that we believe that in both cases the creep mechanism must be dislocation creep. The main reasons for the latter conclusion are: i) the similar values of n obtained for each of the microstructures in tension and compression (Table 5). ii) the weak dependence of $\dot{\varepsilon}_{min}$ on grain size. This is best

seen in Figs. 30c and 30d and Table 5; at 50 MPa and 1200 °C, $\dot{\varepsilon}_{min}$ is *not* a function of grain size.

Based on our previous work on the high temperature deformation of Ti_3SiC_2 [10, 57, 58] it was concluded that: (i) dislocations play a dominant role at room and elevated temperatures; (ii) large internal stress develop due to the lack of five independent slip systems; (iii) at higher temperatures, these internal stresses can be dissipated more readily, especially at lower loads; (iv) modest deformations can result in the formation of domains, that effectively reduce the grain size [10]. These domains are believed to be due to the formation of kink bands. (v) in addition of dislocation creep other mechanism, preliminarily identified to be delamination and grain boundary decohesion are believed to be occurring in tandem with dislocation creep (see below work).

The results presented here are not only in complete agreement with the above conclusions, but more important supply strong evidence for their validity at lower stresses (< 70 MPa). The most important outcome of this work is the observed change in deformation mechanism at about 70 MPa that has never been reported before. Here, we will focus on the deformation mechanism controlling the compressive creep in low and high stress ranges.

3.4.1 Deformation Mechanism

3.4.1.1 Initial stage

Almost all crystalline solids will respond to stress in a linear elastic manner before yielding or fracturing. This elastic response is also typically not a function of microstructure - particularly grain size. The results shown herein (Fig. 29) clearly show that the initial deformation of the FG samples are less than their CG counterparts, in other words the FG samples are stiffer than CG samples at room (Ch. 2) and higher temperatures (Figs. 29a, 29b, 29c and 29d). As important, both microstructures are softer than the Young's moduli measured by the resonant ultrasound spectroscopy (RUS) at testing temperatures (Ch. 5). This is consistent with the physical model proposed in the previous chapter, i.e. the formation of IKBs and KBs at relatively lower stresses at higher temperatures. In other words, Ti_3SiC_2 would rather behave anelastically than linearly elastic. This comes about because the stress needed to initiate IKBs is inversely proportional to grain size (Eq. 2). This causes the FG sample to smaller initial strains than their CG counterpart at the same testing conditions.

3.4.1.2 Mechanisms controlling the quasi-steady state creep

Since the sample size is large, the reduction of the cross-section area caused by oxidation is less than 2% in all tests, it is quite safely to neglect the oxidation effect on $\dot{\varepsilon}_{\min}$ in this work. From our previous work on the tensile creep [57, 58], it was shown that the mechanical response of Ti_3SiC_2, like that of ice [56, 59], is determined by a competition between the internal stresses generation and their dissipation. If the rate of stress dissipation is higher than stress generation (or build up), both solids can exhibit considerable ductility; if not, fast fracture occurs. These conclusions are also true in compression. Note that this was true in ice in compression - very few studies on ice are in tension. Since Ti_3SiC_2 has two and only two independent basal slip systems operating at all temperatures, at relatively low stresses, due to high plastic anisotropy of Ti_3SiC_2, localized internal stress generation and the recovery (stress dissipation) processes control its creep behavior during the steady state.

3.4.1.2.1 Dislocation creep

The two competing processes, stress generation and stress relaxation, are strongly dependent on creep stress (creep rate), temperature, grain size and stress state. At lower stresses and/or lower temperatures, since the $\dot{\varepsilon}_{\min}$ is relatively low, it is easy for the internal stress to be relaxed by dislocation based deformation, such as forming KBs, sub-domains within single grain, etc., (Figs. 31a and 32a). At the same time, due to the lack of 5 independent slip systems, this kind of relaxation will cause

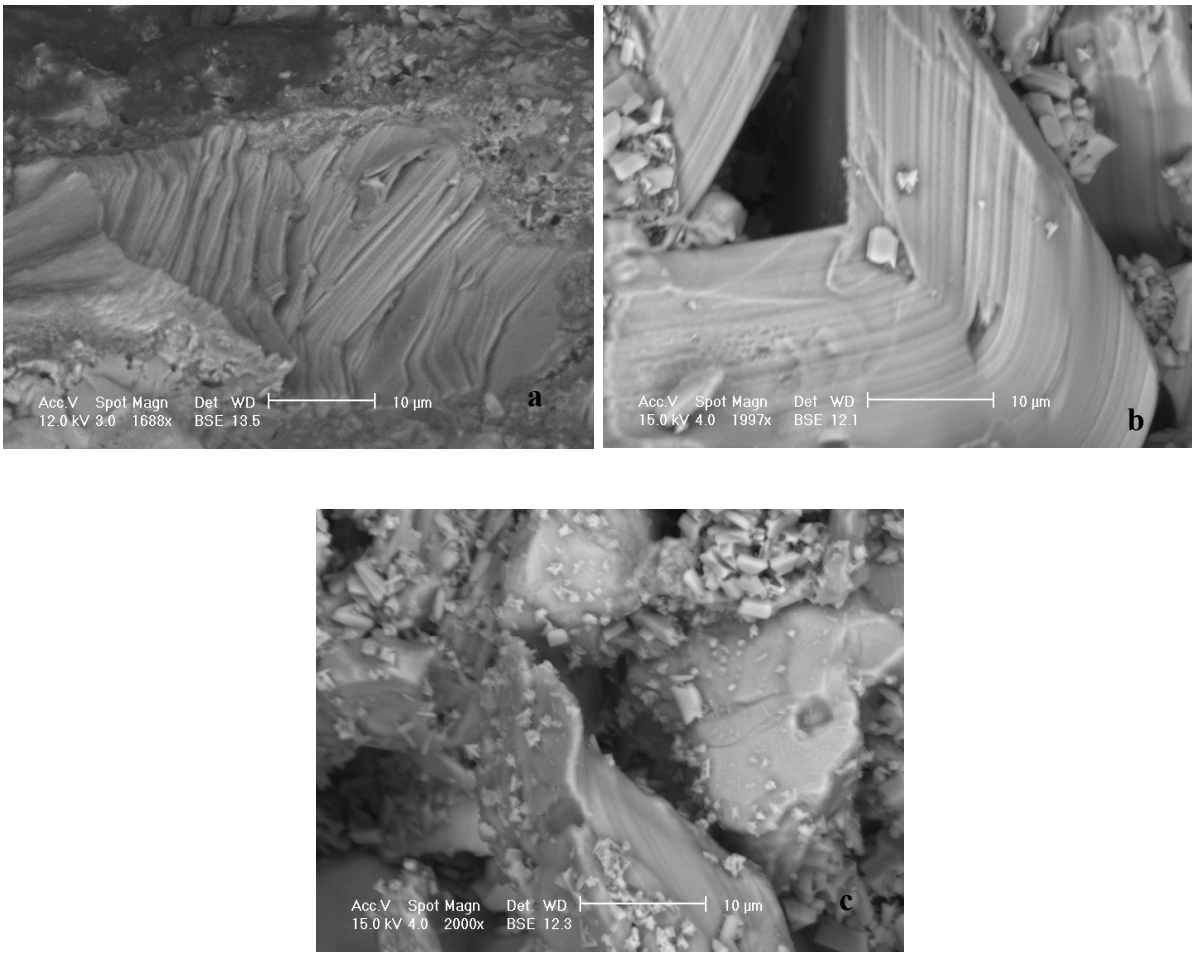

Fig. 31 FESEM of fracture surface of CG sample tested at 1300 ^{o}C and 100 MPa with 4 % of failure strain. a) grain kinking. b) grain kinking and delamination. c). bent grain. Note due to sample was broken at 1300 ^{o}C in air, the fracture surface was oxidized.

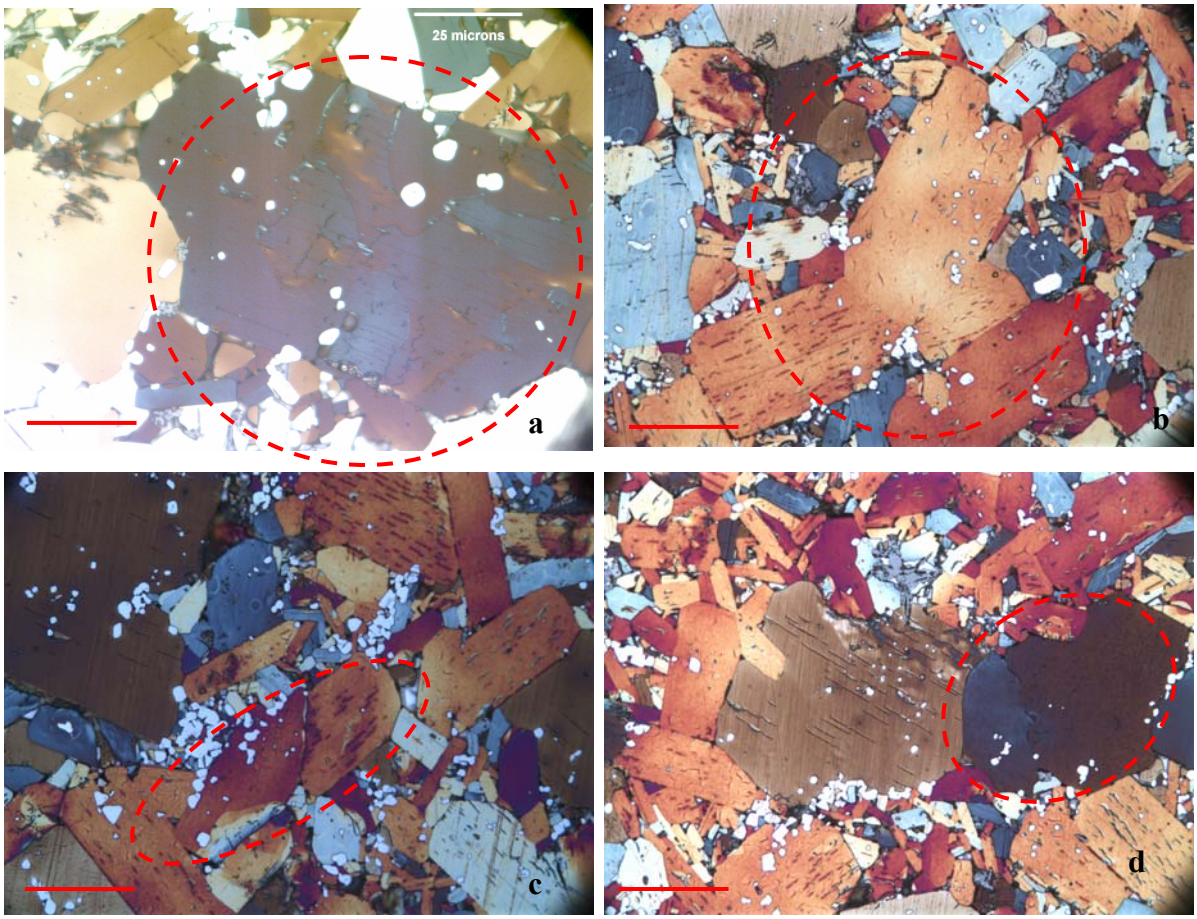

Fig. 32 OM of polished and etched gage surfaces of CG tested at 1300 ^{o}C and 25 MPa, the test was stopped at 4 % strain. a) sub-domain formation. b) bent grain. c) and d) broken grain. The scale bar in (a) equal to 25 μm, in (b), (c) and (d) equal to 50 μm.

some localized damages, such as broken grains, grain boundary decohesion and triple point cavitations. At relatively low creep rate, the damage accumulation rate is low and the damage can be confined locally without growing and linking before reaching a certain damage density (Figs. 32c and 32d). Also the CG samples are more damage tolerant than the FG samples at relatively low deformation/damage accumulation rates in compression. In other words, the CG samples can accommodate more deformation than the FG samples before reaching the tertiary stage (Fig. 30d).

This conclusion is confirmed by the OM micrographs shown in Fig. 33. In Fig. 33, we compare the OM micrographs of two samples tested at 1300 °C and 25 MPa (Fig. 28b). In both the total deformation was 4% strain. It is clear that the density of localized damage in the FG sample is higher than in CG sample.

Similarly the creep curves, of the FG samples reach the tertiary regime, i.e. deviation from the dotted line (Fig. 30), at smaller strains than CG counterparts (Figs. 30c and 30d). But to reach the same deformation, 4%, the FG samples needs more time than the CG samples. This is why after long time creep tests at relatively low stress/temperature, the creep curves of FG and CG microstructure cross each other (Fig. 30d), since the FG sample has higher damage accumulation rate than the CG sample. At this regime, since the creep stress/rate is relatively low, the creep is controlled by dislocation based deformation.

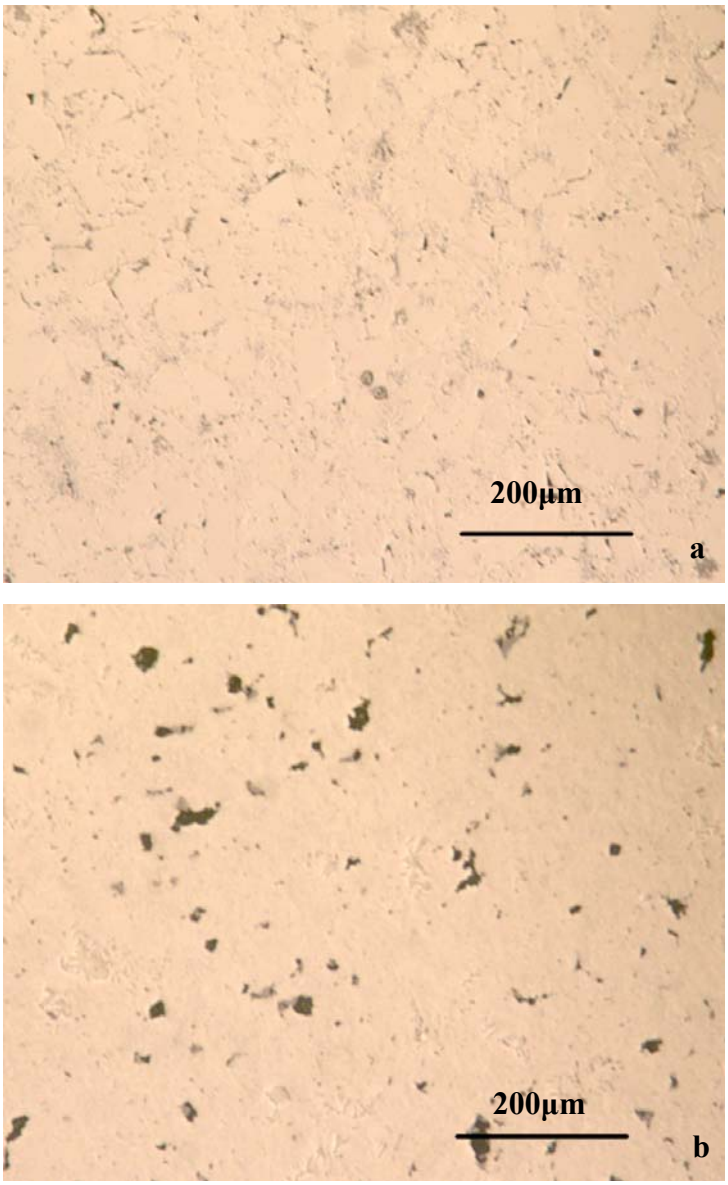

Fig. 33 OM of polished and unetched gage surfaces of CG and FG samples tested at 1300C and 25MPa, both microstructures have the same strain, 4 %. a) CG. b) FG. Note for CG sample, after 4% deformation there are no obvious pores, but for FG sample, there are lots of localized damage.

3.4.1.2.2 Grain boundary decohesion creep

At higher stresses and/or temperatures, the large internal stresses and relatively high creep rates make it is easier to initiate damage and, as important, to link the damage, forming subcritical cracks due to the grain boundary decohesioin (GBD). In other words, at high stresses the time is insufficient for the relaxation of the internal stresses to occur just by a dislocation based-deformation. This will increase the damage accumulation rate and form the damage zone along the fracture surface before failure (Fig. 34). Compare Figs. 34 and 33a, both were CG samples, and have almost the same deformation, ≈ 4% strain, but arrived at that deformation in two quite different paths; shown in Figs. 30a and 30b. Based on these micrographs, there is no doubt that damage accumulation rate at high stresses is significantly higher than that at low stress, even though the samples have the same deformation; the difference of the damage accumulation between those two samples is obvious. In this regime, since GBD rate is the controlling rate and FG sample is more deformation resistant than CG sample [11]. This cause why FG sample is more creep resistant than CG sample at higher creep stresses and/or rates (Fig. 30a and 30b).

On the other hand, CG Ti_3SiC_2 is more damage tolerant than FG Ti_3SiC_2 [43]. In other words, it is easier for FG Ti_3SiC_2 to initiate and link the localized damage. In this regime, the forming of GBD will dramatically affect the $\dot{\varepsilon}_{min}$ of FG Ti_3SiC_2. This is the reason why the n of FG Ti_3SiC_2 in Eq. 14 will increase

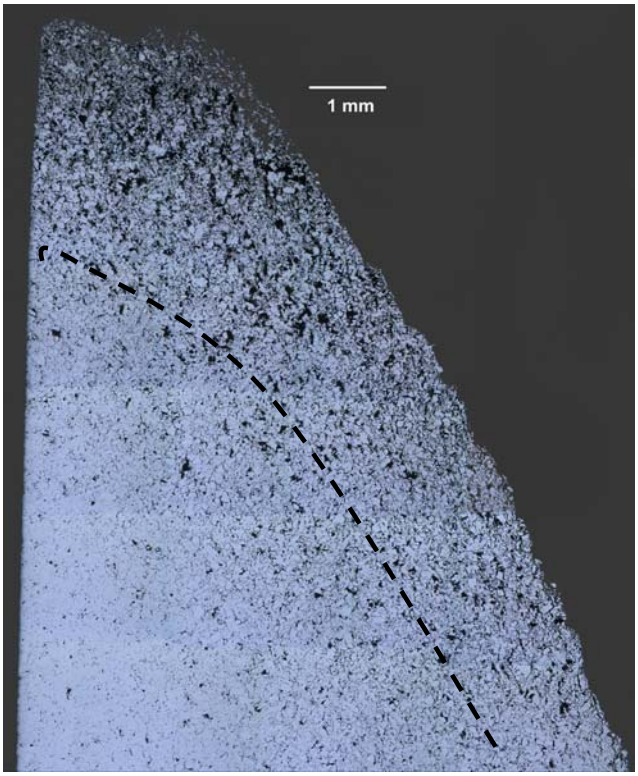

Fig. 34 Composite OM of polished surfaces of broken CG sample tested at 1300 ^{o}C and 100 MPa, with 4.3% failure strain. Above the dotted line is relatively highly damaged zone.

dramatically at high creep stress/rate. As for CG Ti_3SiC_2, since it can accommodate more damage than FG Ti_3SiC_2, the effect is not as obvious as in the FG material.

Also compare with the tensile creep (Figs. 25 and 26), the compressive creep has much lower $\dot{\varepsilon}_{min}$ than tensile creep. This is most probably due to it is easy for damage propagate in tension than in compression.

3.5 Conclusions

The compressive creep of FG and CG Ti_3SiC_2 over a range of testing temperatures (1100-1300°C) is characterized by three regimes, a primary, quasi-steady state and a tertiary. At lower stresses and/or creep rates, the CG samples are more creep resistant than their FG counterparts. The stress exponents are relatively low and close to those measured in tension, viz. 1.9 and 2.2 for the FG and CG samples, respectively. In this regime, the minimum creep rates in compression are roughly an order of magnitude lower than those in tension. At relatively high stresses and/or creep rates, the stress exponents of the FG samples increase dramatically and, yet surprisingly, in some cases the FG samples are more resistant to deformation and failure than the CG ones, suggesting a change of mechanism from dislocation creep to possibly sub-critical crack growth. This conclusion is bolstered by post-deformation microstructural analysis that shows the strong evidence of sub-critical crack growth.

The compressive creep occurs by a combination of plastic deformation and damage accumulation. The latter most probably occurs by a combination of grain breakage, triple point cavitation, delamination and grain boundary decohesion. As in tension, the creep response is characterized by the presence of large internal stresses. The overall creep response thus depends on the rate of generation and dissipation of these internal stresses.

4. Effect of Temperature, Strain Rate and Grain Size on Mechanical Response of Ti_3SiC_2 in Compression

4.1 Introduction

This chapter is a continuation of our work to understand the mechanical response of KNE solids in general, and the compressive response of Ti_3SiC_2 as function of temperature, strain rate and grain size in particular. Based on our results to date the mechanical response of Ti_3SiC_2, and by extension the other MAX phases, is characterized by high fatigue resistance [32] and damage tolerance [34,38] and a relatively high fracture toughness (8-12 MPa $m^{1/2}$) with R-curve behavior in which the fracture toughness can reach 16 MPa $m^{1/2}$. Furthermore, a brittle-to-ductile transition, BDT, occurs between 1100 and 1200 °C. The strain rate sensitivity of ≈ 0.55 (i.e. a stress exponent of 1.8) is relatively high for crystalline solids [60]. When loaded slowly, the stress-strain curves in tension reach a broad maximum in stress. The plateau stress is a function of strain rate and is lower for lower strain rates [10, 60]. Conversely, if loaded rapidly, the stress does not peak, but instead the material fails on the rising part of the stress-strain curves, i.e. the response is more brittle [10, 60].

Most of the mechanical properties of the MAX phases, including Ti_3SiC_2 described in this work, can be traced to the following three facts: (i) Basal slip, and only basal slip, is operative at all temperatures. The Burgers vector in the basal plane

is 1.5 Å; any nonbasal dislocation would have to have a Burgers vector > 17 Å [35, 36]. In other words, they lack the 5 independent slip systems required for ductility. They do, however, possess more operative slip systems than ceramics, which is why they are more damage tolerant, thermal shock resistant and softer [32, 34, 38]. If the grains are oriented and large, Ti_3SiC_2 is ductile even at room temperature [38]. (ii) Because of their high c/a ratios, twinning is unlikely [49], and has never been observed. Instead, these compounds deform by the formation of kink bands within individual grains [37 - 39]. Kink bands are of paramount importance to this work and are discussed in much more detail below. (iii) Because they are confined to the basal planes, the dislocations arrange themselves either in arrays (pileups) on the same slip plane, or in walls (low or high angle grain boundaries) normal to the arrays [35, 36]. The only interactions possible between dislocations are those where the arrays intersect the walls. This does not allow for the formation of forests of dislocations for example and the concomitant work hardening. Hence, dislocations can move back and forth reversibly and extensively.

Li et al. [46] were the first to report on the non-linear response of Ti_3SiC_2, in bending at room temperature; an observation they ascribed to a combination of microcracking and deformation. The effect was small and the hysteresis loops obtained were open. Radovic et al. [10] cycled fine-grained Ti_3SiC_2 samples in tension and were the first to report closed hysteresis loops in the narrow stress range between 120 and 200 MPa.

In chapter 2 we have shown that macroscopic polycrystalline Ti_3SiC_2 cylinders can be compressed at room temperature to stresses of up to 1 GPa and fully recover upon the removal of the load. The stress-strain curves at room temperature are non-linear, outline fully reversible reproducible closed loops whose size and shape depend on grain size, but not strain rate. The loss factors for Ti_3SiC_2 are higher than most woods and comparable to polypropylene and nylon. Furthermore, the energy dissipated per cycle, $W_{d,}$ was found to scale with the square of the applied stress, σ. This phenomenon was attributed to the formation and annihilation of fully reversible incipient kink bands (IKBs) [11], defined to be thin plates of sheared material bounded by near parallel dislocation walls of opposite polarity that remain attached, and are thus attracted to each other. Removal of the load allows the walls to collapse and the IKB to be totally eliminated. Recent nanoindentation experiments on Ti_3SiC_2, graphite and mica have shown that all three solids behave in a similar way [12 - 14]. Apparently at higher stresses the IKBs dissociate into mobile walls that in turn coalesce to form regular kink bands (KBs) that are no longer reversible. In other words, the KBs that from essentially reduce the domain size, which in turn leads to hardening.[11-14]

The effect of temperature, grain size and strain rate on the mechanical response of Ti_3SiC_2 in compression is considered in this chapter. The discussion is focused on both, fine (3-5 μm) and coarse (100-300 μm) grained microstructures.

4.2 Experimental Procedure

The processing details can be found elsewhere [40]. Briefly, the specimens were produced by reactive hot isostatic pressing (HIPing) a stoichiometric powder mixtures of titanium (-325 mesh, 99.5%, Alfa Aesar, Ward Hill, MA), silicon carbide (- 400 mesh, 99.5%, Atlantic Engineering Equipment, Bergenfield, NJ) and graphite (- 300 mesh, 99%, Alfa Aesar, Ward Hill, MA). HIPing at 1450 °C at a pressure of 40 MPa for 4h resulted in a fine-grained (FG) microstructure; HIPing at 1600°C , 40 MPa for 6h resulted in a coarse-grained , CG, microstructure.

Tests were performed using cylindrical shaped specimens (9.8 mm in diameter and 30 mm in height), with a gauge length of 25 mm. They were electro-discharge machined (EDM) and tested with no further surface preparation.

All the tests were performed in air using a hydraulic MTS 810 testing machine, which was supplied with a controller (Microconsoler 458.20) that allowed tests to be run in displacement or load control mode. In all tests, there was 1 ~ 2 MPa preload to keep the sample aligned. Strains were measured by a high-temperature capacitance MTS extensometer, with 5% capacity; the force was measured using a load cell with 100 a kN capacity.

4.3 Results

4.3.1 Temperature effect on cyclic response

Typical loading-unloading stress-strain curves for CG and FG Ti_3SiC_2 cylinders loaded in compression at different temperatures are shown in Figs. 35 and 36, respectively. These results clearly demonstrate that:

i. The hysteresis loops at high temperatures are open for both microstructures (Figs. 35 and 36). Unlike the fully reversible room temperature behavior, the response of both microstructures becomes irreversible; i.e., the deformation is permanent at high temperature regime.

ii. The material becomes softer as the temperature increases for both the FG and CG samples. The effect is more pronounced for CG microstructure, however.

iii. The loop areas increase dramatically as the temperatures increase, indicating material can dissipate more energy at higher temperatures.

iv. The loading-unloading stress-strain curves of the CG sample (Fig. 35) are open at temperatures as low as 500^{o}C. In contradistinction, for the FG samples the response is still comparable to RT behavior, i.e. fully reversible, even at 900^{o}C.

Figure 37a compares the 1200 °C stress-strain curves for the FG and CG microstructures subjected to the same loading-unloading conditions (Fig. 37b). Here

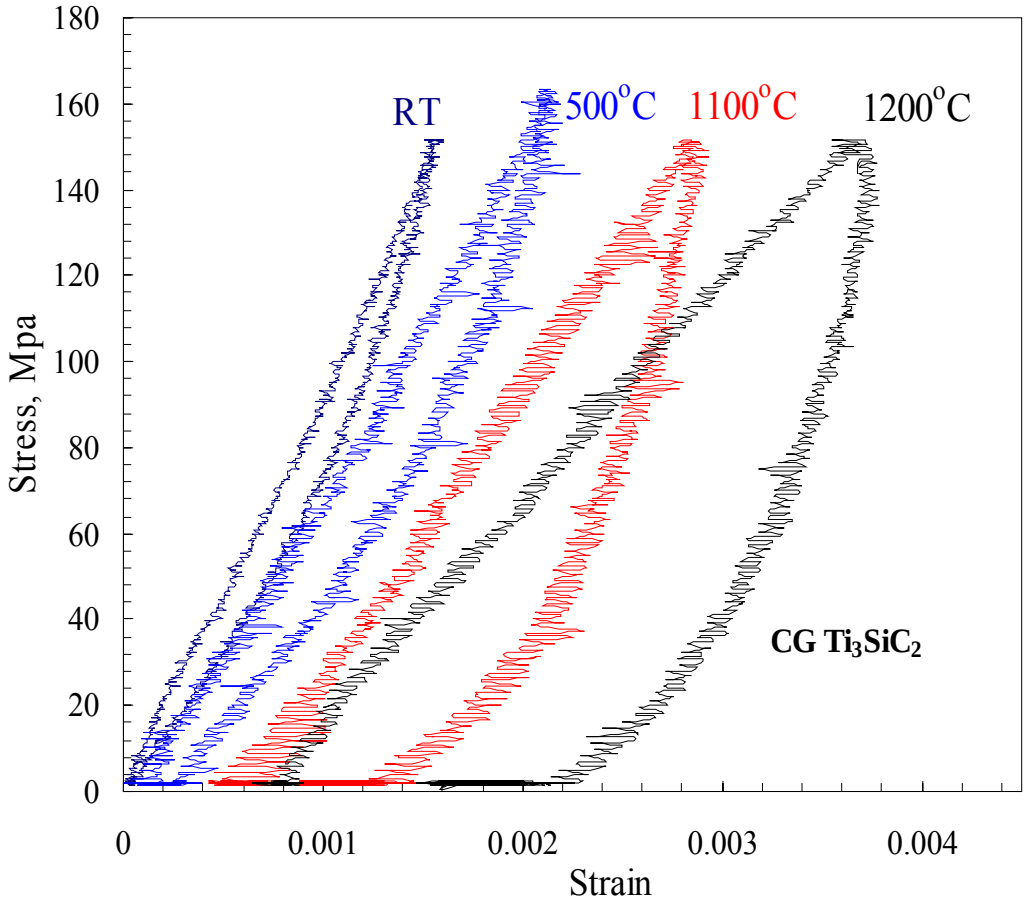

Fig. 35 Compressive loading-unloading stress-strain curves of coarse-grained Ti_3SiC_2 cylinders loaded at room temperature, 500, 1100 and 1200°°C. The 1100°°C result was shifted to the right 0.00075 for clarity. The initial strain at 1200°°C results from two low load pre-cycles. (see Fig. 40 for detail).

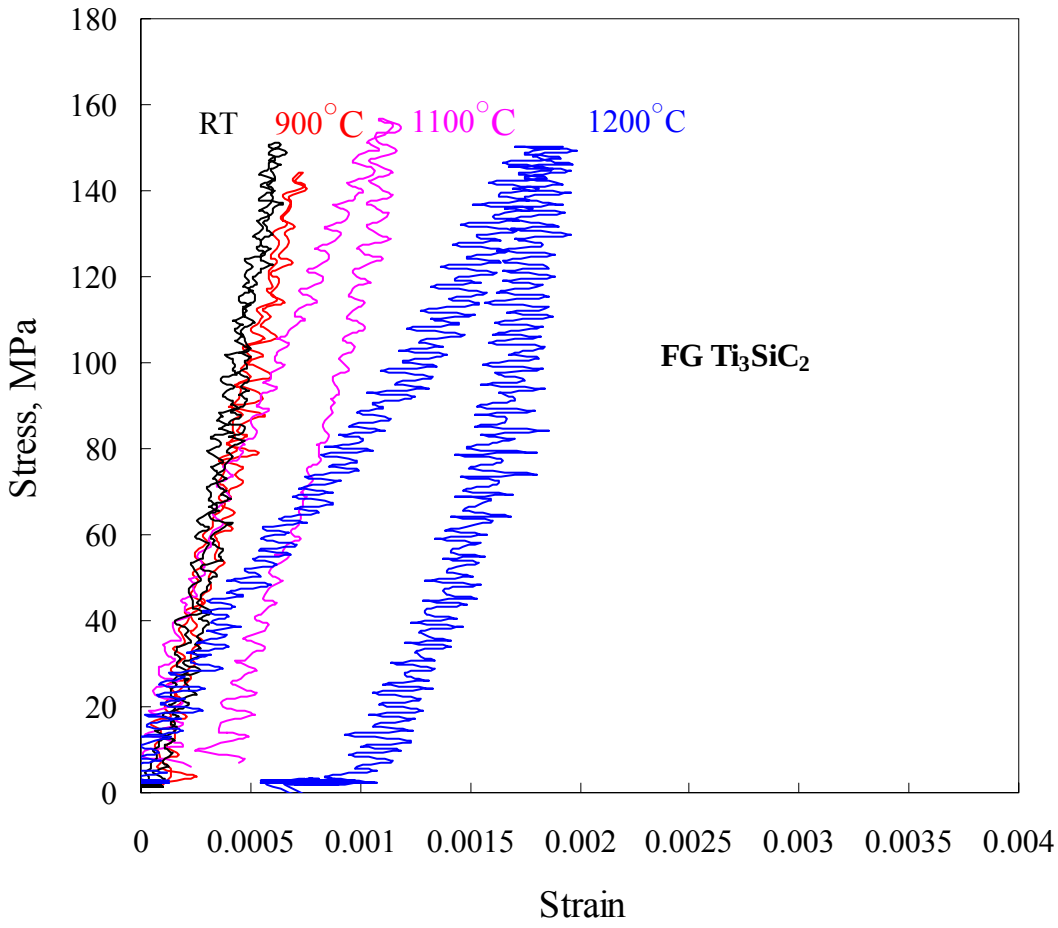

Fig. 36 Compressive loading-unloading stress-strain curves of fine-grained Ti_3SiC_2 Cylinders loaded at room temperature, 900, 1100 and 1200°C.

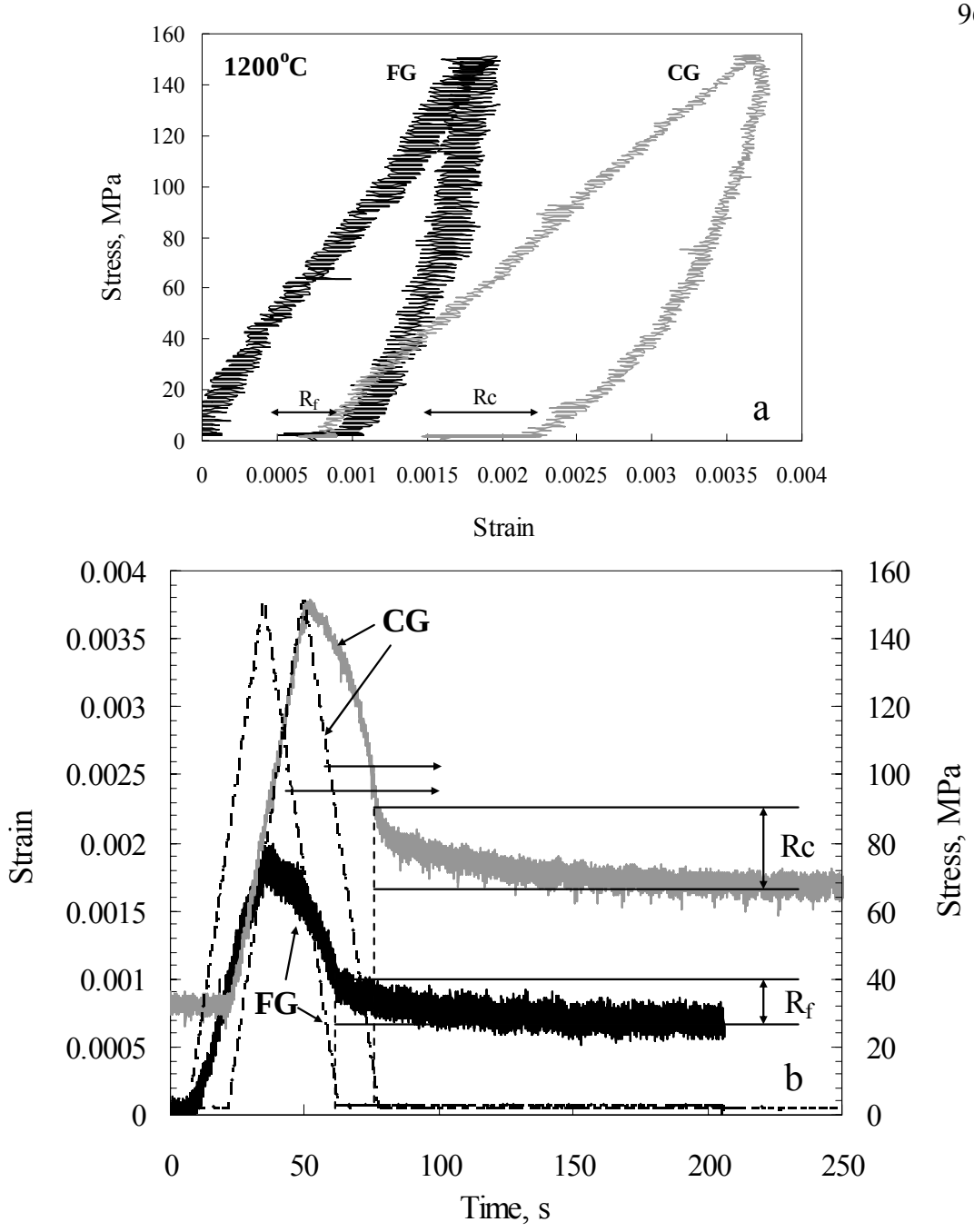

Fig. 37 Loading-unloading compressive behavior of FG and CG Ti_3SiC_2 at 1200°C. a) Stress-strain curves; b) Time dependencies of stress and strain. R_c and R_f represent the expansions of the CG and FG samples after complete unloading, respectively.

again, the FG samples are stiffer and result in smaller areas per cycle. A remarkable feature of the high temperature deformation is the continued and significant shrinkage after unloading, denoted by R_c and R_f in Fig. 37a for CG and FG samples respectively. This is best seen in Fig. 37b in which the time dependencies of the stresses and strains are plotted. There is no doubt that the samples keep shrinking for a relatively long time after the load is removed. Such time dependent behavior is in good agreement with the anelastic strain recovery observed in the tensile tests of this material [35, 36]. Note after a recovery time range of ≈ 150 s, the anelastic strain of the CG sample, R_c, is almost the twice that of the FG (Fig. 37b) microstructure, R_f. This implies that the recovery rate of the CG samples is higher than the FG one (Fig. 35). This may due to the higher internal stresses in the CG sample.

The unloading recovery is unambiguous evidence for the presence of large internal stresses. Such behavior is typical of viscoelastic materials [61, 62] and is strongly dependent on time and loading history. The result here is also consistent with the stress relaxation results in both tension [35, 36] and compression (see Ch. 3). Since the recovery rate of the CG samples is higher than that of FG samples under similar loading conditions, this implies that the internal stress is also dependent on the microstructure; the larger the grain size, the higher the internal stresses.

4.3.2 Strain rate effect at high temperature

Figures 38 and 39 show the compressive loading-unloading stress-strain curves of FG and CG samples at 1200°C. Note the unloading rates in Figs. 38b and 39b are ten times slower than the loading rates. Here the bow out during unloading is clear (Figs. 38a and 39a). The bow out comes about because the stress and strain are not in phase at the beginning of the unloading (Figs. 38b and 39b). Both FG and CG samples continue to shrink upon unloading up to certain stress level, after which they expand (Figs. 38b and 39b). This response, clearly observable in Figs. 38b and 39b, is usually referred to as viscoplastic [61, 62]. Compared with the lack of a strain rate effect at the room temperature (Figs. 15 and 16), it is clear the high temperature compressive mechanical response of Ti_3SiC_2 is highly dependent on the deformation rate for both the FG and CG microstructures. In other words the mechanical response is strongly dependent on time and loading history.

4.3.3 Cyclic loading-unloading at 1200^{o}C

Cyclic stress-strain curves obtained at 1200 °C on CG samples with increasing stress amplitude are shown in Fig.40. It should be noted here after each loading-unloading test, the sample was held for enough time until the recovery rate was less than $10^{-5}s^{-1}$. The results show that:

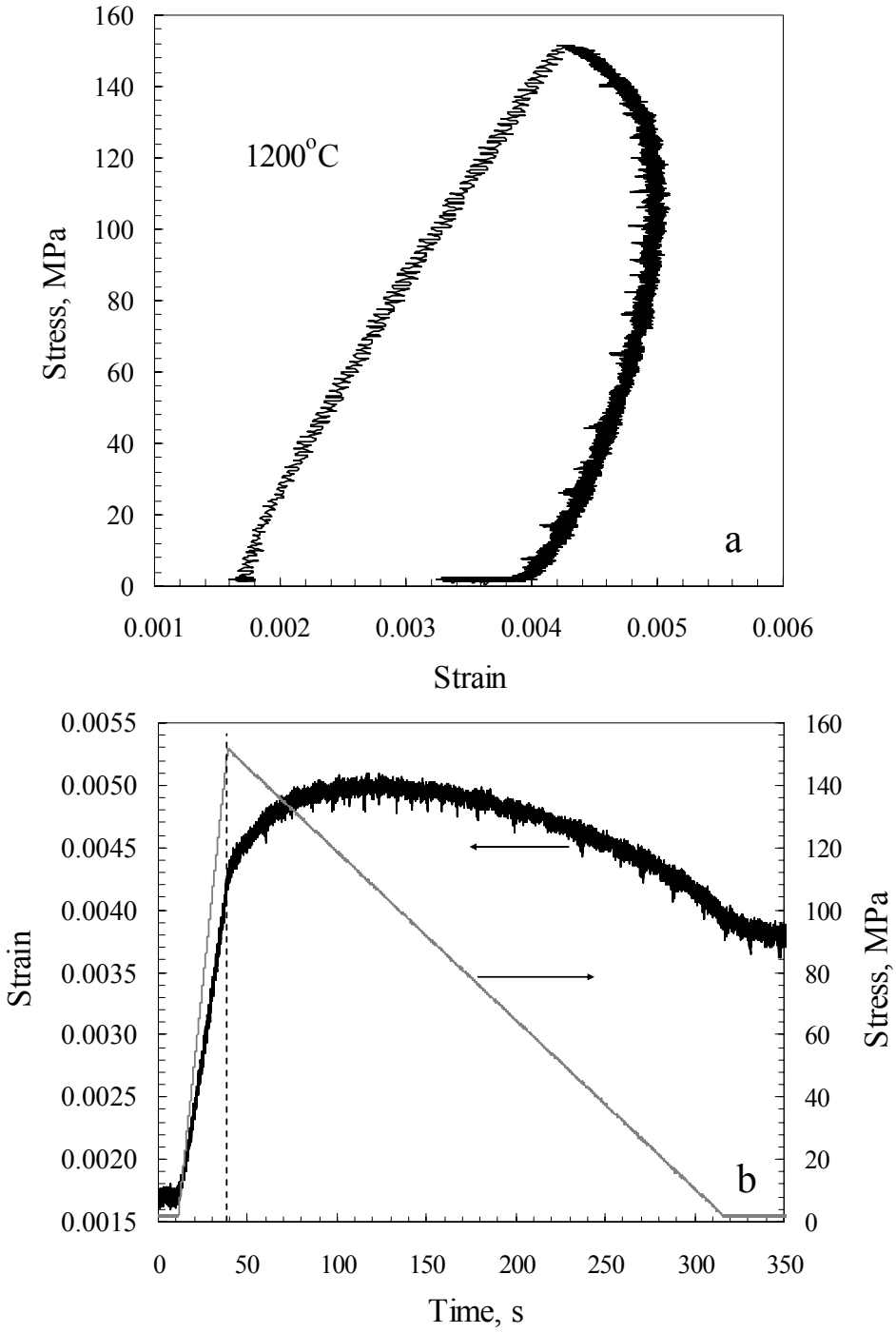

Fig. 38 Compressive loading-unloading compressive behavior of CG Ti_3SiC_2 cylinders loaded at 1200 ^oC. a). Stress-strain curves. b). Time dependencies of stress and strain. Note the unloading rate is 10 times slower than loading rate. The dashed line indicates the starting point of unloading.

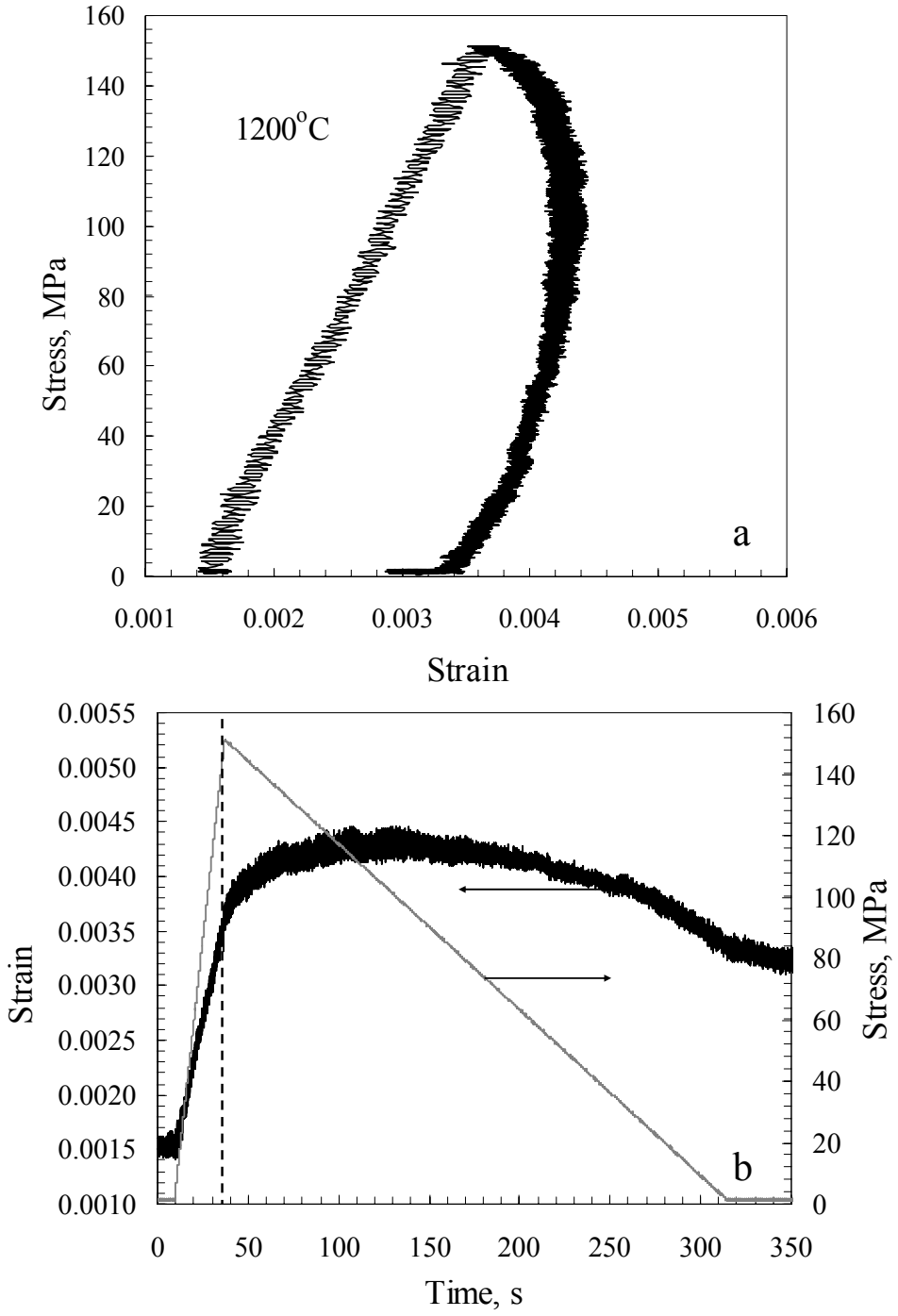

Fig. 39 Compressive loading-unloading compressive behavior of FG Ti_3SiC_2 cylinders loaded at 1200 °C. a). Stress-strain curves. b). Time dependencies of stress and strain. Note the unloading rate is 10 times slower than loading rate. The dashed line indicates the starting point of unloading.

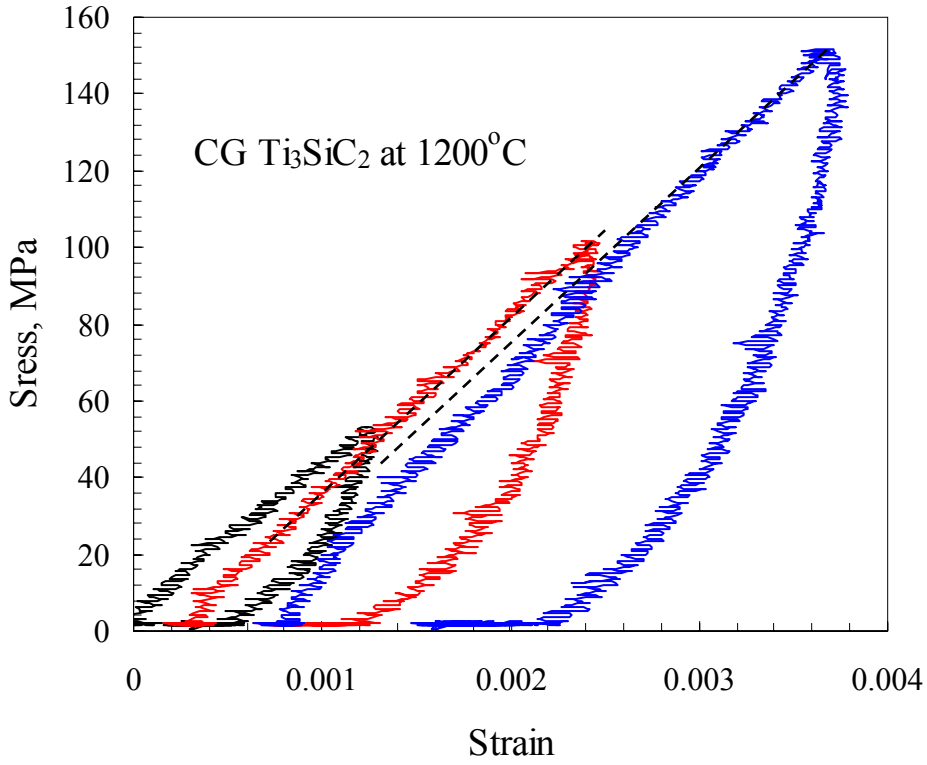

Fig. 40 Compressive stress-strain curves obtained during cyclic loading-unloading of CG Ti_3SiC_2 cylinder loaded at 1200°C, for increasing stresses amplitude. Note after each cycle there is the recovery stage, i.e. the sample continues expand after completely unloading. The successive cycles were started when the recovery rate was < 10^{-5} s^{-1}.

i. As the stress increases, the area of the loops increase dramatically, indicating the energy dissipation is strongly dependent on the maximum loading stress.

ii. The recovery effect is more pronounced after high stress cyclic loading. For example the strain recovered after the 150 MPa cycle is more than the *total* deformation after the 50 MPa cycle.

iii. The loading curves during the 100 MPa and 150 MPa cycles in Fig. 40, it is clear the slope (dashed line in Fig. 40) of 150 MPa cycle at the same stress level is higher than that of the previous at 100MPa cycle. It indicates the materials become stiffer after pre-loading at lower stress levels.

Even clearer evidence for cyclic hardening effects at 1200^{o}C is presented in Figs. 41 and 42 for the CG and FG microstructures, respectively. Figures 41a and 42a show the totality of the cycles of the tests. Color-coded cycles are extracted from each microstructure and plotted starting from zero strain for comparison; the results are show in Figs. 41b and 42b for CG and FG Ti_3SiC_2, respectively. The hardening is manifested by both a reduction in the total areas enclosed by the successive cycles and the general stiffening. Note that it is only after the sample is cycled a few times that a clearly defined elastic response at low strain is observed. By the 21st cycle, the initial slope of the loop on loading ≈ 270 GPa, is almost identical to the value of Young's modulus, 288 GPa, obtained by resonance ultrasound spectroscopy (RUS, see Ch. 5 for detail) at 1200 °C for both microstructures.

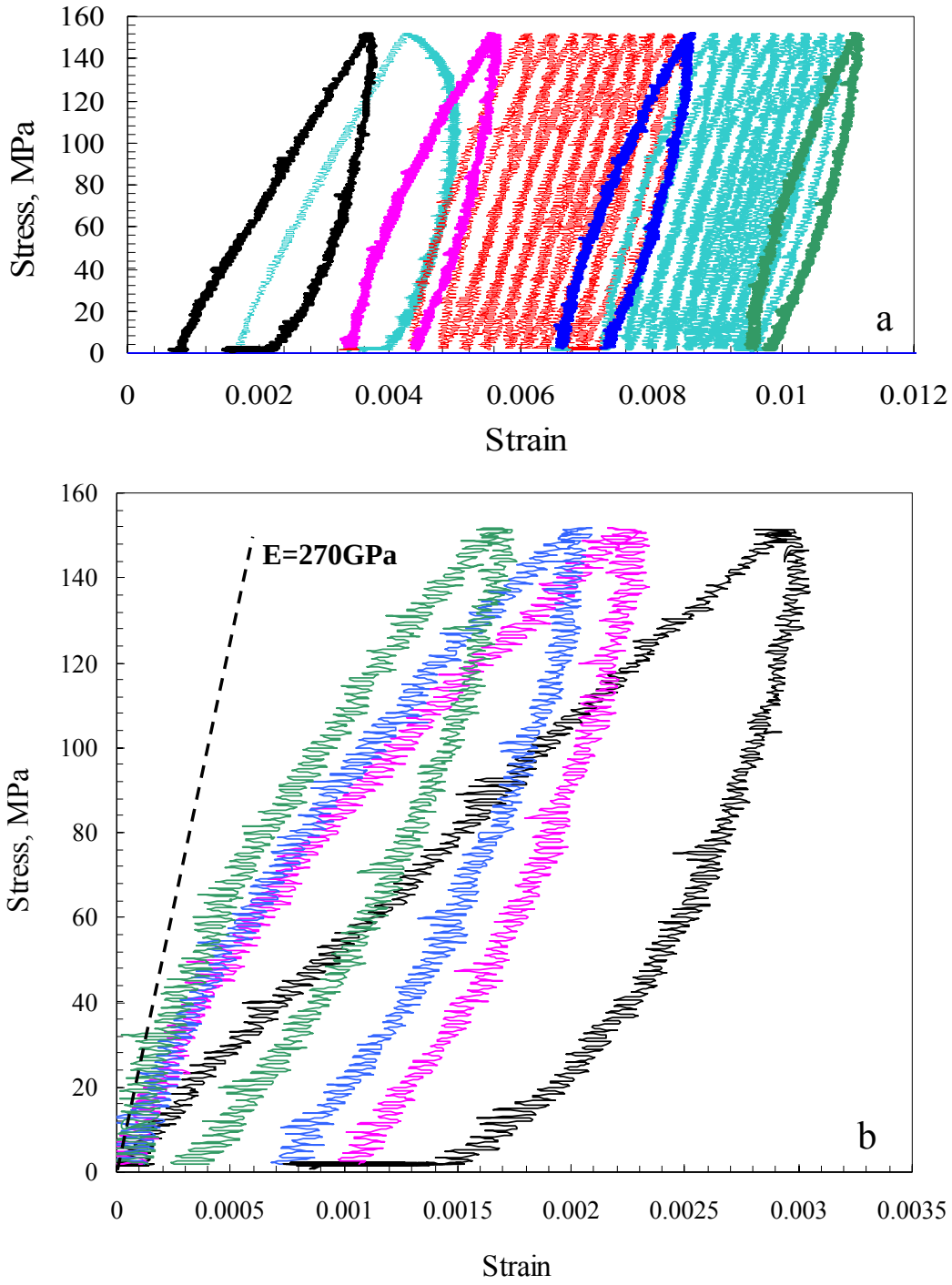

Fig. 41 Compressive cyclic loading for CG cylinder at 1200 °C. a) the totality of cycles; b). Select, color-coded cycles are extracted from a. The dashed line in b represents a Young's modulus E = 270 GPa.

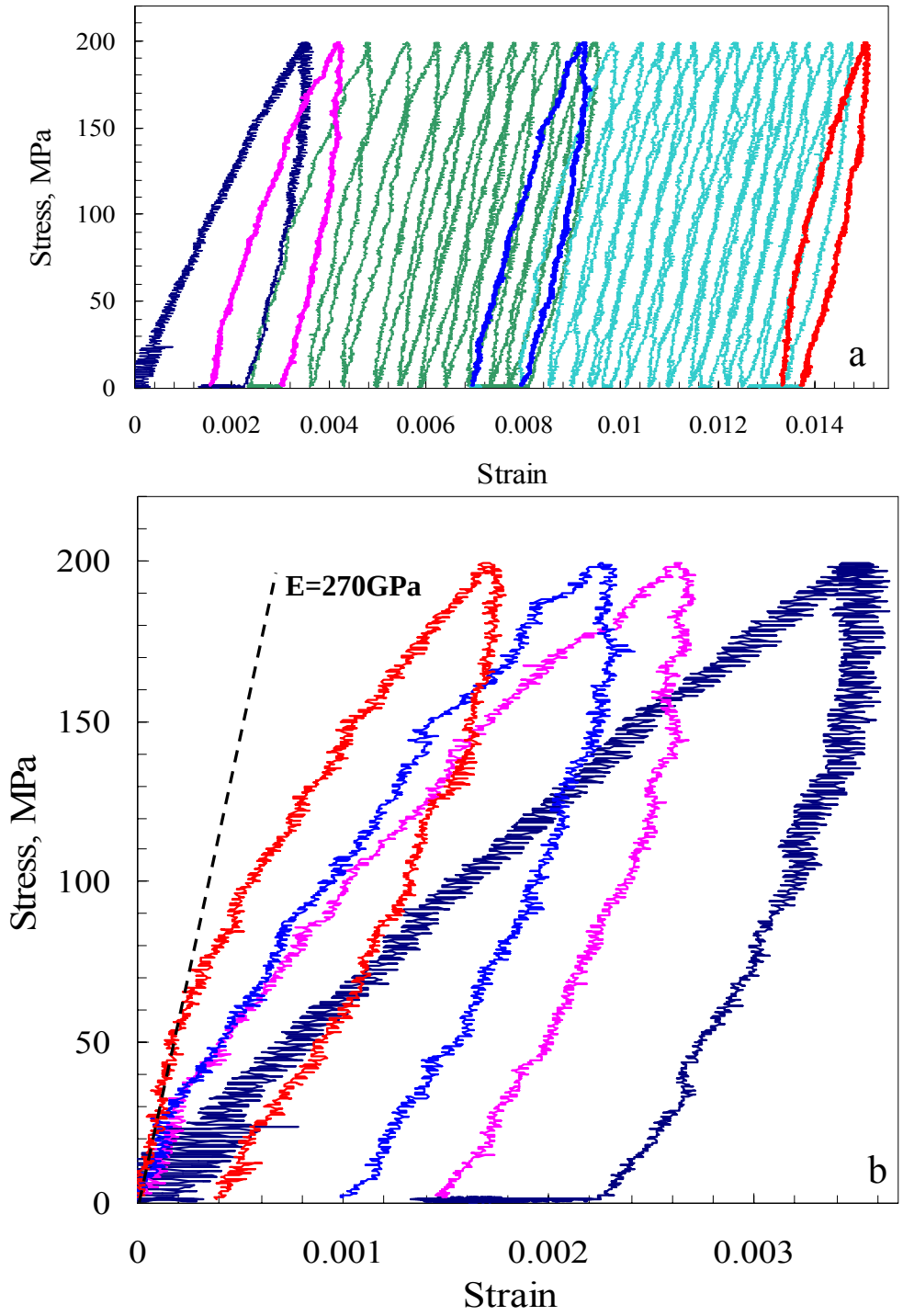

Fig. 42 Compressive cyclic loading for FG cylinder at 1200 ^{o}C. a) the totality of cycles; b). Select, color-coded cycles are extracted from a. The dashed line in b represents a Young's modulus E = 270 GPa.

4.3.4 Effect of high temperature deformation

Figure 43 compares the room temperature compressive loading-unloading stress-strains curves of a CG sample before, and after a 2% deformation at 1300 °C. The inset of Fig. 43 shows the high temperature deformation history. The high temperature deformation resulted in:

i) A general hardening on the structure when compared to the room temperature behavior of the same sample before deformation at 1300^{o}C.

ii) The first cycle after the high temperature test is open and has a larger enclosed area than the second cycle, which traces a very nearly closed loop.

4.3.5 Dissipated energy

The areas enclosed by the hysteresis loop represent the energy dissipated per unit volume per cycle, W_d. Figures 44, 45 and 46 show the dependence of W_d on stress and temperature of both CG and FG microstructures, in different plots. These results indicate that:

i) At the same loading condition, W_d is larger in the CG than the FG material (Figs. 44, 45 and 46). This is compelling, unambiguous evidence that grain

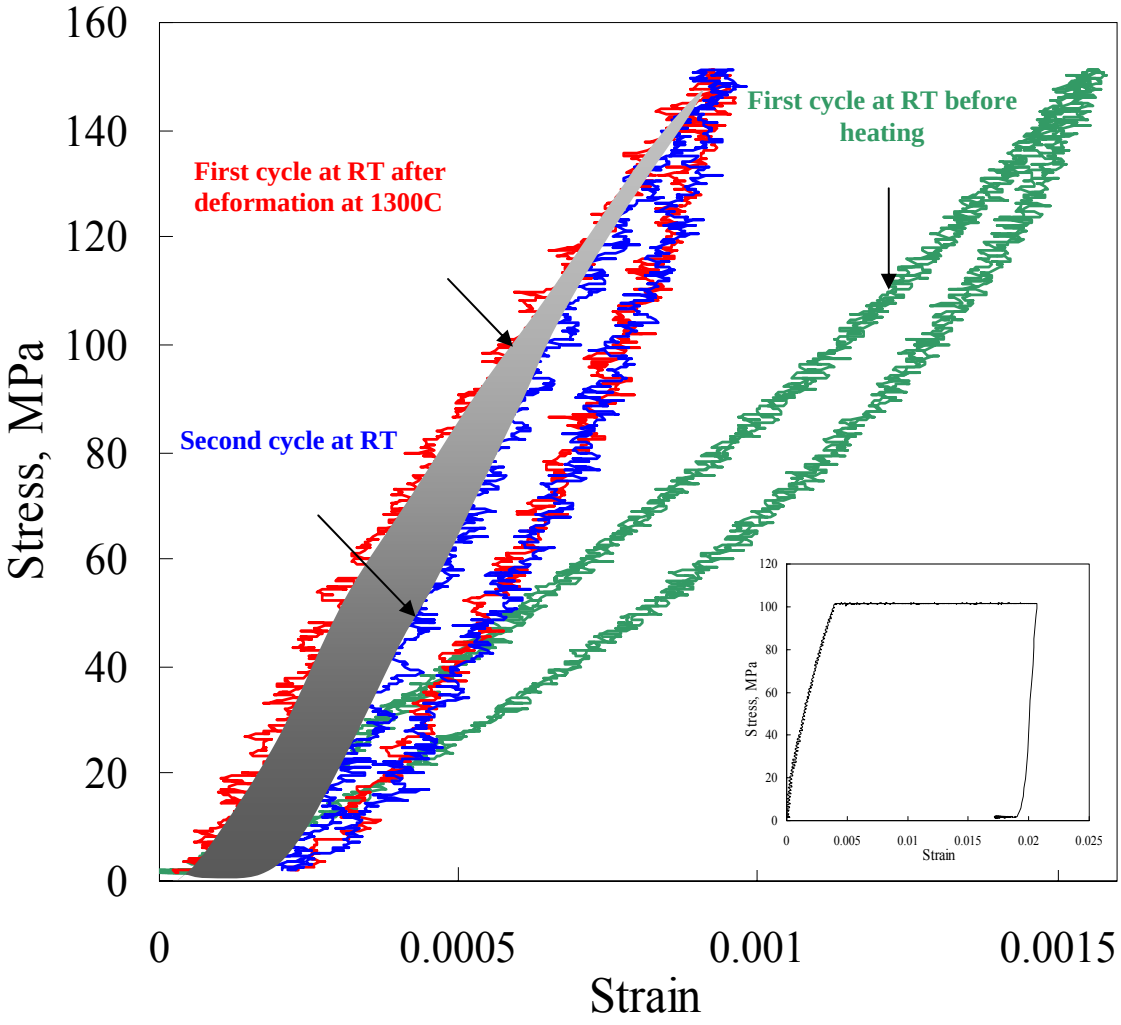

Fig. 43 Room temperature compressive stress strain curves of CG Ti_3SiC_2 cylinder at different stage. The green curve is the first cycle at room temperature before heating the sample. The red one is of the first cycle also at room temperature after 2% of deformation (compression) at 1300 ^oC. The blue curve is cycle following the red one. Inset shows the stress strain curve at 1300 ^oC for the same sample.

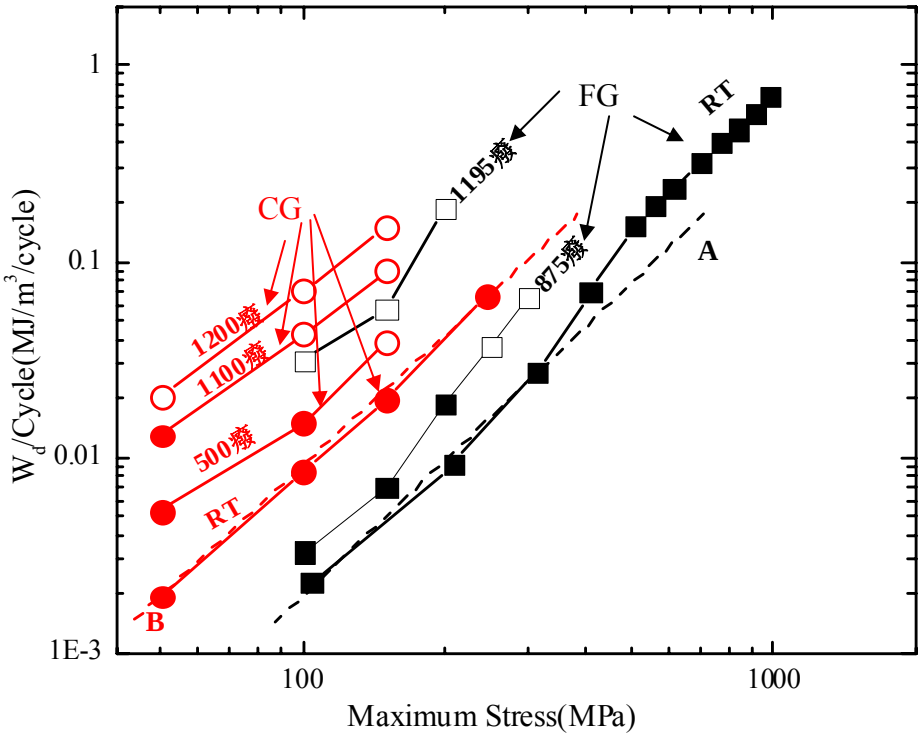

Fig. 44 The dependence of dissipated energy, W_d, on stress at different temperature for both the CG and FG microstructures, in a log-log plot. Black denotes FG and red CG samples. Least squares fit of the dashed lines A and B yield slopes of ~2.2,with values of $R^2 > 0.99$. Filled symbols imply the loops were closed, open symbols open loops.

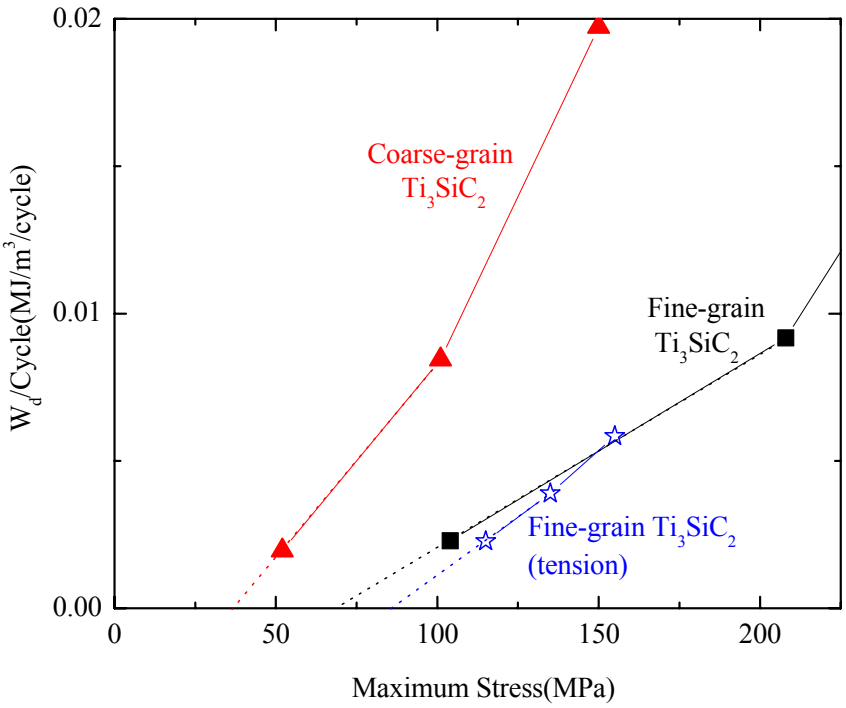

Fig. 45 The dependence of dissipated energy, W_d, on compressive stress at room temperature for both CG and FG microstructures at low stress levels, in a linear plot. Solid squares and triangles denote fine-grain and coarse-grain samples in compression respectively. The open stars denotes the fine-grain sample in tension.

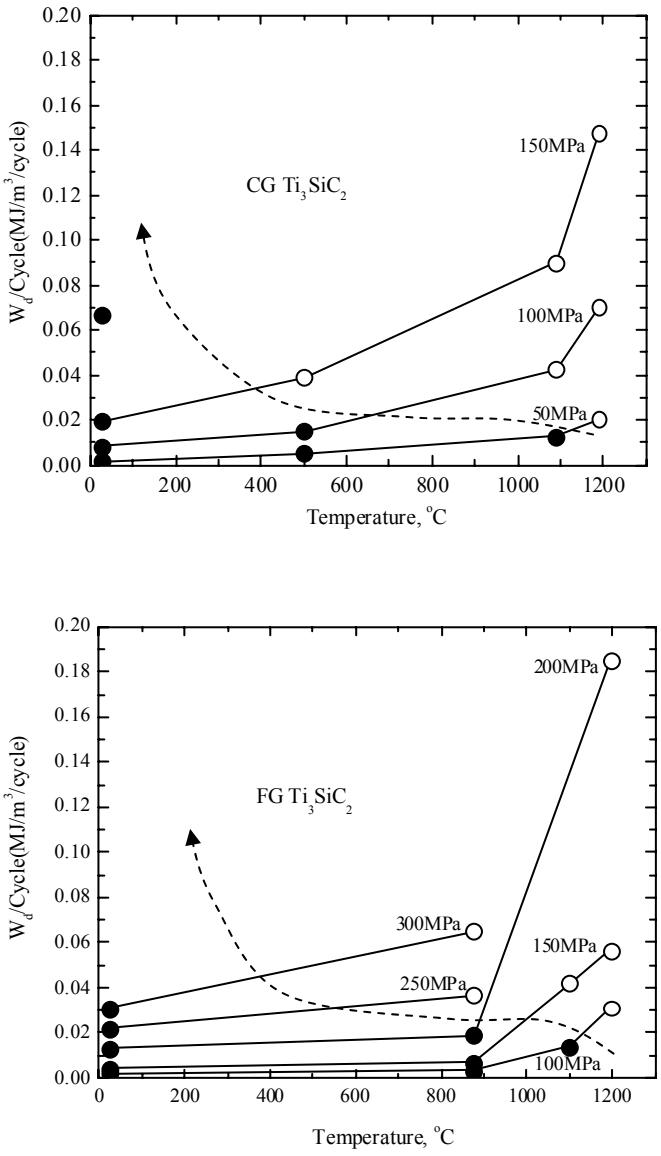

Fig. 46 The dependence of dissipated energy, W_d, temperature at different stresses. (a) CG Ti_3SiC_2. (b). FG Ti_3SiC_2. Filled symbols indicate the loops were closed, open symbols open loops.

boundaries are not the source of the hysteresis loop, since the grain boundary area is higher in the FG samples.

ii) Least square fits of the dashed lines A and B in Fig. 44 yield slopes of 2.2, with $R^2 > 0.99$ for both microstructures. The results obtained by Radovic et al. [10] on FG samples in tension are also in excellent agreement with the results obtained here (Fig. 45).

iii) At ≈ 38 MPa, the threshold for the initiation of IKB's in the CG samples are *lower* than the ≈ 70 MPa required for the FG samples (Fig. 45).

4.4 Discussion

The importance of kinking and in the deformation of Ti_3SiC_2 is now well established at all lengths scales – atomic [36], micro [38] and macro [39]. Direct high-resolution transmission electron microscopy evidence for the presence of dislocation walls *and* arrays also exists [36]. In these papers it was shown that a 15° misorientation was indeed accommodated by a dislocation wall, with dislocations more or less uniformly spaced with a D ≈ 6 Å. The close relationship between the deformation of Ti_3SiC_2 and ice, both highly plastically anisotropic solids has been established [56, 63]. The buildup of substantial internal stresses due to the dislocation pileups has also been documented in tensile and tensile creep experiments [57, 60]. And while in this work we have no direct evidence for the formation of subgrain boundaries - their low volume fraction and reversible nature being two good reasons

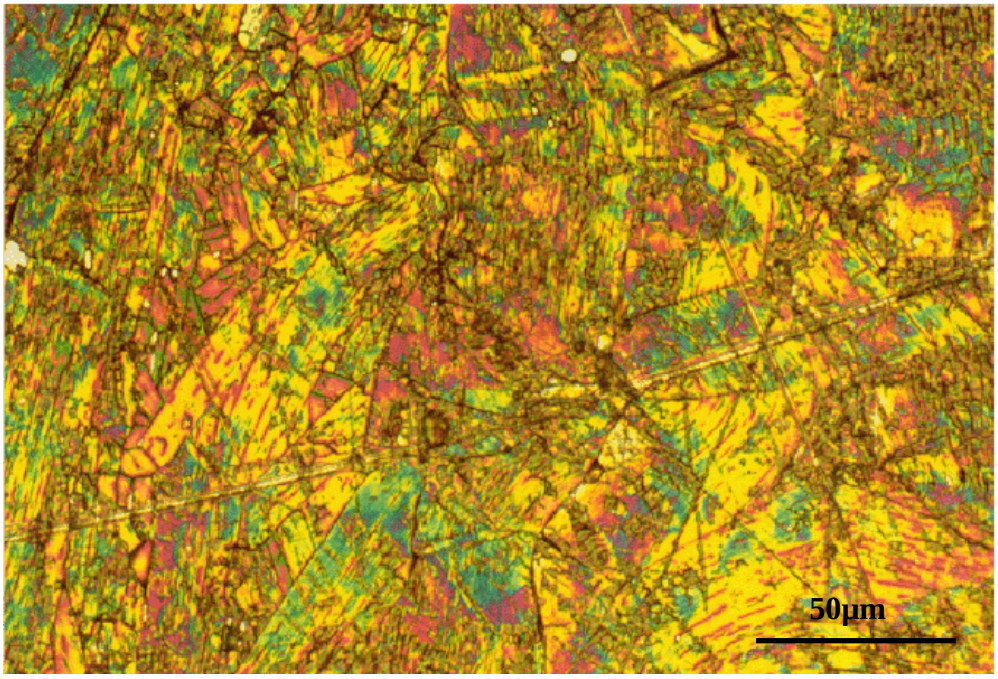

Fig. 47 Etched optical micrograph of a sample comprised of 1-2 mm grains after heavy deformation at 1300 °C in air. The field of view used to be a single large grain.

– it has repeatedly been shown that deformation of large-grained Ti_3SiC_2, both at room [39] and elevated temperatures [41], results in grain refinement. An extreme example is shown in Fig 47, where the extent of grain breakup and kink band formation is obvious.

Cyclic hardening categorically rules out microcracking as the origin of the hysteresis loops. This is especially true given that the hardening is occurring despite a total increase in the sample's plastic strain with the number of cycles (Figs. 41 and 42). Based on our IKB model discussed in chapter 2 and compared with the room temperature properties of Ti_3SiC_2, we propose the following kink-based model to explain our observations in Ti_3SiC_2.

4.4.1 Fully reversible regime

In the fully reversible regime, the application of a load, as a direct result of having less than five independent slip systems and the strong mechanical anisotropy (i.e. the presence of only basal slip), the stress distributions within the solid rapidly become very uneven [56, 59]. Soft grains with basal planes favorably oriented to the applied stress will deform by glide, which will result in dislocation pileups at grain boundaries. These in turn, result in high local shear stresses, τ_{loc}. Hard grains, are those for which the basal planes are parallel to the applied load. To accommodate τ_{loc},

the hard grains will locally buckle or form IKBs. The IKBs grow to the width, w, of the grains but no further; the dislocation walls do not detach and the IKBs remain incipient, or reversible, as per our definition. With increasing load the density of IKBs increases and they start populating more grains. Furthermore, if more than one IKB exist in a grain, they remain non-interacting. Upon the removal of the applied load, the IKBs disappear and no permanent deformation is recorded, a process that can be repeated many times at very high stress levels in the range of 700 MPa - 1GPa.

The evidence for this model is multifold. The energy dissipated, W_{irr} results from the friction associated with the to and fro motion of the dislocations comprising the IKBs and pileups. Since the dislocations are confined to the basal planes and cannot readily interact, the distances over which they glide are of the order of the grain size; which explains both the high absolute values of W_d and why W_d is higher for the CG than the FG samples (Figs. 42, 43 and 44). In other words, because work hardening does *not* occur, the dislocations can move *reversibly* over relatively large distances. This point is crucial and fundamental: we submit that Ti_3SiC_2 is the only solid that can be loaded reversibly and repeatedly in compression up to 1 GPa and simultaneously be able to dissipate ≈ 25 % of the total mechanical energy.

4.4.2 Partially reversible regime

In the partially reversible regime, e.g. at higher temperatures, the grain boundaries are softer, and the IKBs can now presumably extend into them or detach Their attraction to each other is eliminated, and upon the removal of the load, part of the deformation is now plastic or irreversible. Furthermore, once the walls detach, the whole force is available to nucleate another IKB inside the now parallel, detached, mobile walls [48, 49]. As important, the coalescence of walls from the same or adjacent sources result in kink or subgrain boundaries. In other words, the large grains are broken up into smaller ones. Also such dislocation motion will form the dislocation pile up along the grain boundary. The stress concentration at the tip of the dislocation, σ_x, is given by [64]:

$$\sigma_x = C_0\left(\frac{L}{x}\right)^{1/2} \qquad (15)$$

where C_o is a constant and x is the distance from the tip. L is the length of the pileup, which is assumed to scale with the grain size. It thus follows that CG samples will have higher stress concentrations at the tip of the pileup than FG samples at the same applied stress level. This is why at the same testing condition the CG sample will deform more than their FG counterparts.

At higher temperatures, it is fair to assume that the grain boundaries soften, which would convert the IKBs to KBs (Fig. 5c), resulting in a permanent deformation manifested by the open loops. Note that at 1200 °C, the anelastic strains are

substantial after complet unloading (Figs. 35-42), which implies high temperature deformation induced internal stresses. Grain boundary sliding is also now possible.

Our interpretation also accounts for the substantial reductions in W_d and general stiffening - as compared to before high temperature cycling - observed for the CG samples (Fig. 43). This observation is key because it unambiguously proves that at higher temperatures some of the IKBs open up (Fig. 5c), creating glissile walls *and* that these walls in turn interact to form sub-boundaries (Fig. 5d). Once the boundaries are in place, higher stresses are required to initiate IKBs, and the volume over which they can sweep is limited; in essence the CG material becomes a FG one, and behaves accordingly (Fig. 43). Since, after similar cycling, the changes in a FG sample were much less severe, it is fair to conclude that under the loads applied the critical kink volume is of the order of the fine-grained material or 3-5 μm. As noted above, this does not imply subgrain boundaries do not form in the FG material, simply that it is more difficult and/or less prevalent. The main evidence for their formation is the cyclic hardening observed at 1200 °C (Fig. 42b). With increasing cycle numbers, the deformation cell size shrinks, shrinking the volume available for kinking. This in turn, increases the stress needed to initiate them, reducing W_d. The reduction in cell size also makes it impossible for the material to kink at low stresses, which is why the tangent modulus of the 25^{th} cycle (dashed line in Figs. 41b and 42b) at low stresses is indistinguishable from the modulus - 270 GPa - expected at 1200 °C had the response been linear elastic [Ch. 5].

4.5 Summary and conclusions

Compressive tests at room and higher temperatures on Ti_3SiC_2 reveal two distinct regimes of mechanical response:

Fully reversible, hysteric response at room temperature was observed even at 1GPa. The response depends on microstructure, not strain rate. This is attributed to the formation and annihilation of incipient kink bands. As long as the dislocation walls remain attached, the response is fully reversible. It clearly shows Ti_3SiC_2 is one of typical KNE solids as discussed in Ch. 2.

At higher temperatures, the loops are open and response becomes strain rate dependent. Cyclic hardening was observed even at 1200^{o}C for both FG and CG microstructure. This is attributed to the dissociation of the dislocation walls to cause significant hardening which occurs by the formation of deformation cells or polygonization.

The technological implications of the results discussed herein are far reaching. Anelastic phenomena are important factors in fatigue and fracture behavior. A materials' ability to absorb, and thus not transmit vibration, or noise, is related to its damping capacity. Mechanical vibrations in engineering structures can create severe

problems. Thus the ramifications of having a lightweight inexpensive, elastically stiff solid (with a specific stiffness almost 3 times that of Ti) machinable with a manual hack saw, with compressive strengths of ≈ 1 GPa, that can also damp a significant portion (25 % at 1 GPa) of the mechanical energy will not be inconsequential in applications and fields as diverse as precision machine tools, quiet, vibration free machinery and transportation equipment, industrial robots, the performance of electronic and MEMS devices, the wobble of disc drives or low density armor, among others.

In metals, high damping capacity is generally observed in materials that exhibit poor mechanical properties such as low hardnesses or yield stresses [65]. Thus, the strategies for developing high loss metals are ones where the microscopic mechanisms that control the mechanical properties are *decoupled* from those responsible for the dissipation of mechanical energy [65]. Here the situation is fundamentally different because the applied loads create the kinks, responsible for the energy losses. From a practical point of view this is a crucial difference because the damping is now active at useful stresses. This conclusion is also consistent with the fact that the high losses observed here are observed in ultrasound measurements on Ti_3SiC_2 at high temperature (see Ch. 5 for detail).

It is important to place the results obtained here in perspective. The loss factors for Ti_3SiC_2 are higher than most woods and comparable to polypropylene and nylon (Fig. 48). Most important the damping properties of Ti_3SiC_2 are orders of

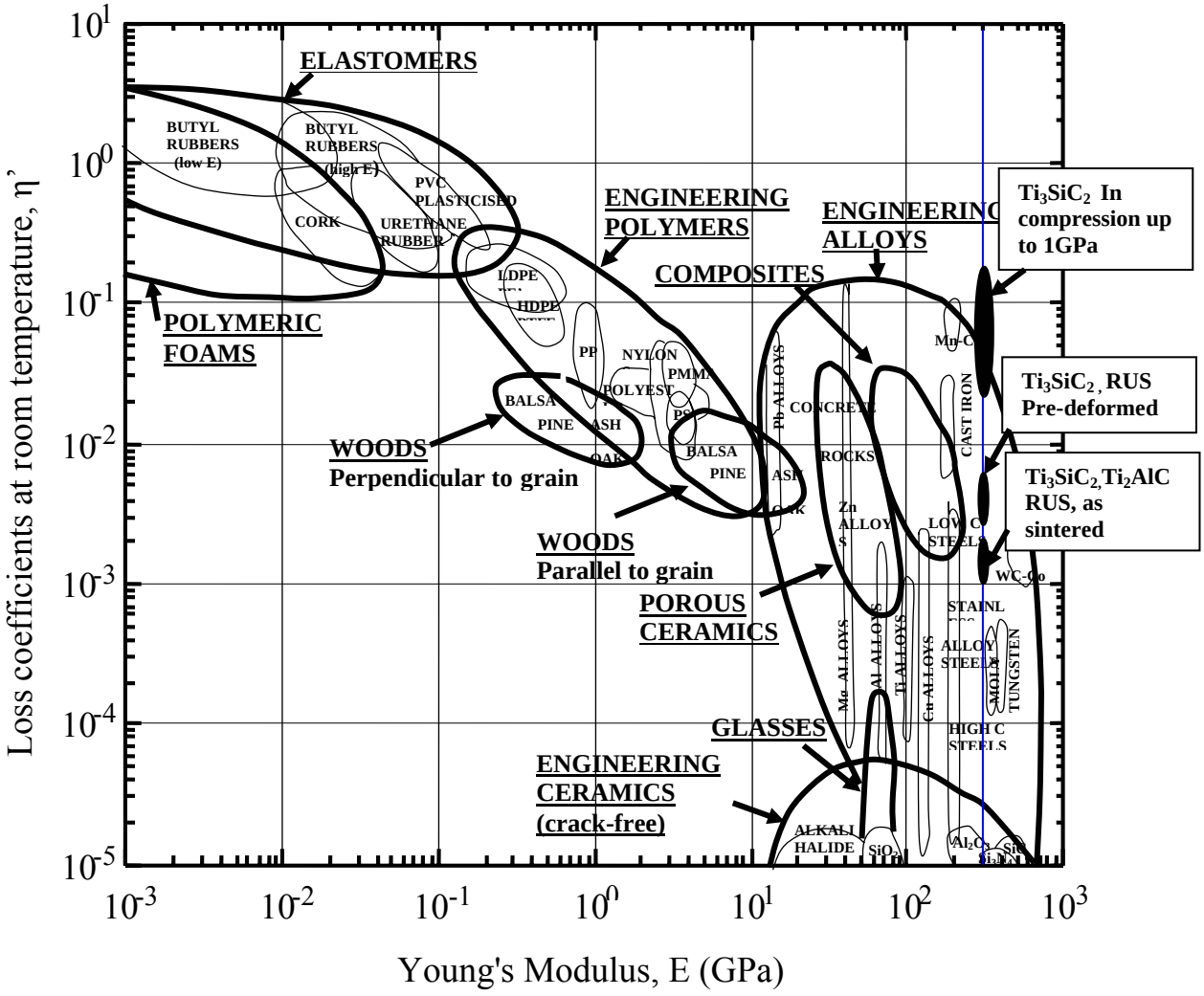

Fig. 48 Ashby map [79] of loss coefficient vs. Young's Modulus.

magnitude higher than those of other structural ceramics (Fig. 48). As noted above, as far as we are aware, the *reversible* energy absorbed per cycle, 0.7 MJ/m^3, at 1 GPa, is probably a record for a crystalline solid. For comparison, the losses in elastomers are of the order of 10 MJ/m^3; values that arise as a result of large strains [66]. As some level, it is not unreasonable to think of Ti_3SiC_2 as a stiff, strong ceramic rubber that can be used at high temperatures. This is even true at higher temperatures, i.e. at 1200^{o}C, more than 50% of input mechanical energy will be dissipated at stresses ≈ 150 MPa for both the FG and CG microstructures (Figs. 39 and 40) and at the same time resulting in cyclic hardening.

Three concluding remarks. First, we fully appreciate that dislocation pileups (arrays) must play an important role; at the very least they probably trigger the kinking. Other than that, our results do not permit further speculation at this time; we are currently exploring the problem. Second, and despite the results shown herein, we are not claiming that the response is 100 % reversible; nothing is. Preliminary evidence we have obtained has shown that cycling reduces the ultimate strengths. Furthermore, the range of stresses over which this phenomenon is applicable in tension is much smaller. These comments notwithstanding, it is fair to say that, within the resolution of our extensometer, the process is indeed reversible. It is also fair to conclude that if a solid can withstand 100 cycles at 700 MPa, its fatigue properties at lower stresses should be excellent. It has already been shown that the long crack fatigue properties of Ti_3SiC_2 are exceptional [32].

Third, even in the unlikely eventuality that the physical phenomenon described herein does not blossom into new applications, its study should greatly enhance our understanding of plastic deformation in other solids. These polycrystalline nanolaminates are almost ideal model materials for the study of dislocation dynamics and interactions of walls or pileups with grain boundaries, and other obstacles, without complicating factors, such a twinning, and work hardening, formation of forests, etc., that have dogged metallurgists and material scientists, almost from the inception of the field. The further prospect of studying dislocation dynamics on more than 50 MAX phases that exist, and the innumerable combinations of solid solutions, is a wonderful one indeed, and one that should prove to be of immense importance and benefit.

5. Elastic Properties of Ti_3SiC_2 and Ti_2AlC at 298-1573K Temperature Range

5.1 Introduction

The ternary carbides with the general formula, $M_{n+1}AX_n$ (where n=1 to 3, M is an early transition metal, A is A-group element, and X is C and/or N) are now referred to as MAX phases in the literature [37, 67-69]. In Ch. 2 we showed that macroscopic polycrystalline Ti_3SiC_2 cylinders can be compressed, at room temperature, to stresses up to 1 GPa, and fully recover upon the removal of the load [11]. This phenomenon was attributed to the fully reversible formation and annihilation of incipient kink bands, IKBs, defined as near parallel dislocation walls of opposite polarity that remain attached, and are thus attracted to each other. Removal of the load allows the walls to collapse and the IKB to be totally eliminated. It is obvious that Ti_3SiC_2 does not behave in a linear elastic fashion, therefore even at room temperature in both simple tensile and compressive tests [10, 11]. Note that Young's modulus, E, is a function of grain size in compressive tests. To investigate the elastic properties of the MAX phases and by extension to all the KNE solids, other techniques should be explored other than by mechanical testing.

Resonance ultrasound spectroscopy (RUS) is a relatively novel ultrasonic technique, developed by Migliori et al. [73, 74] for determining the complete set of elastic moduli of a solid by measuring the free-body resonances of the sample. This

method can determine all the moduli simultaneously in a single measurement with unprecedented absolute and relative accuracy from cryogenic to elevated temperatures. The basic principle of this technique is that the mechanical resonances of a solid depend on its shape, density and moduli in a way sufficiently complex that a measurement of the resonant frequencies of a carefully made sample can be used to determine the full elastic tensor. For isotropic polycrystalline solids there are two elastic moduli, Young's, E, and shear, G.

Finkel et al. reported on Young's, E, and shear, G, moduli of Ti_3SiC_2 measured using an ultrasonic echo-pulse technique in the 20-300K temperature range [75, 76]. At room temperature the Young's, E_{RT}, and shear, G_{RT}, moduli were reported to be 339±2 and 142±2 GPa, respectively. Poisson's ratio was 0.2. Both moduli were weak functions of temperature and plateau out at temperatures below ≈ 125K. The moduli were also not a function of grain size. Bao et al.[77] evaluated the elastic moduli of Ti_3SiC_2 and Ti_3AlC_2 using cyclic loading-unloading three points bending tests in 20-1200^{o}C temperatures range. They found that the elastic moduli of Ti_3SiC_2 were nearly constant in the temperature range from 20-1000^{o}C and then dramatically decline with further increase in temperature.

The goal of this chapter is two fold. First, to discuss the temperature behavior of the elastic constants of Ti_3SiC_2 and Ti_2AlC in the 298-1573 K temperature range as measured by RUS. Second, to investigate the ultrasonic attenuation as a function of temperature and deformation history.

5.2 Experimental Procedure

The processing details have been presented elsewhere [37, 40]. Briefly, the Ti_3SiC_2 sample were produced by reactive hot isostatic pressing (HIPing) a stoichiometric powder mixtures of titanium (-325 mesh, 99.5%, Alfa Aesar, Ward Hill, MA), silicon carbide (- 400 mesh, 99.5%, Atlantic Engineering Equipment, Bergenfield, NJ) and graphite (- 300 mesh, 99%, Alfa Aesar, Ward Hill, MA). HIPing at 1600 °C, 40 MPa for 6 h resulted in a coarse-grained (42 ±39μm), CG, microstructure. Two different shaped Ti_3SiC_2 samples were used for this work. One is a disk shaped specimen (25.4 mm in diameter and 3.08 mm in thickness) and the other is a rectangular bar specimen (16.5 x 9.8 x 1.2 mm, cut from a cylinder shaped specimen which was deformed 4 % at 1300^{o}C under stress of 25 MPa). The Ti_2AlC sample was provided by S. Gupta, special thanks to Gupta to allow the author to use his sample.

A schematic of the experimental tripod setup for RUS is shown in Fig. 49. The specimens were in the form of thin discs supported by three piezoelectric transducers. One transducer (transmitting transducer) is used to generate an elastic wave of constant amplitude and varying frequency, whereas the other two transducers are used to detect the resulting signals. The spectrum obtained cannot be deconvoluted to deduce the elastic constants [73, 74]. Instead, an approximate

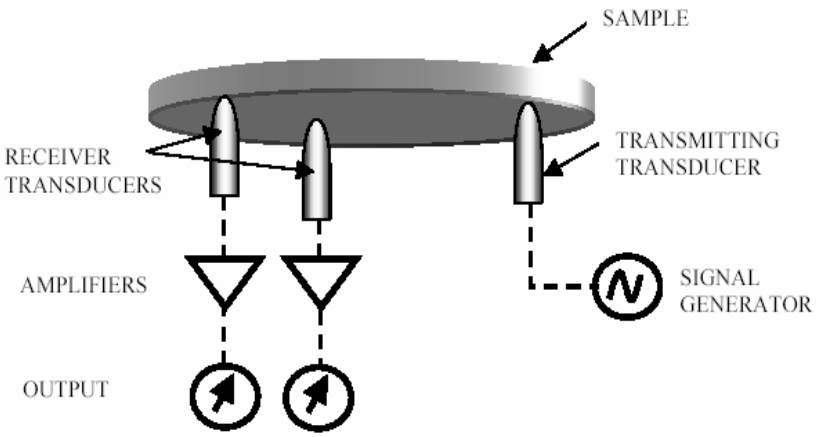

Fig. 49 Schematic of the tripod experimental setup for Resonant Ultrasound Spectroscopy.

spectrum is calculated from the known sample dimensions, density and a set of "guessed" elastic constants. A multidimensional algorithm to minimize the root-mean-square (RMS) error between the measured and calculated resonant peaks enables the estimation of the elastic constants of the solid from a single frequency scan.

In this work the first 40 resonance peaks were fitted for both Ti_3SiC_2 and Ti_2AlC assuming elastic isotropic (two independent elastic constants, Young's and

shear moduli). The measurements were performed for both compositions in the 0-450 KHz frequency range with a 0.03 KHz frequency resolution. The temperature was monitored by two thermocouples, one right above, and the other right below the sample. The temperature difference between the two thermocouples was $\leq 1^{o}C$. At each temperature, before a measurement was taken, the sample was held for 15 minutes, to reduce any temperature gradients in the sample. To avoid oxidation, the high temperature tests were carried out in an Ar environment. The oxygen concentration at high temperatures was monitored by an oxygen analyzer and was less than 100 ppm for all runs.

5.3 Results and Discussion

5.3.1 Elastic property

Typical RUS spectra obtained for coarse-grained Ti_3SiC_2 at $25^{o}C$ and $1200^{o}C$ are shown in Figs. 50a and 50b, respectively. The black crosses indicate the peak frequencies obtained by fitting the measured spectrum. The results for Ti_2AlC (Fig. 51a and 51b) are similar to the ones shown in Fig. 50. Note the significant widening of the peaks observed at 1200°C for Ti_3SiC_2 and 1300°C Ti_2AlC (Figs 50b and 51b). Agreement between experiment and computation was higher than 99.4 % after a best fit to the moduli for both Ti_3SiC_2 and Ti_2AlC tests at all temperatures.

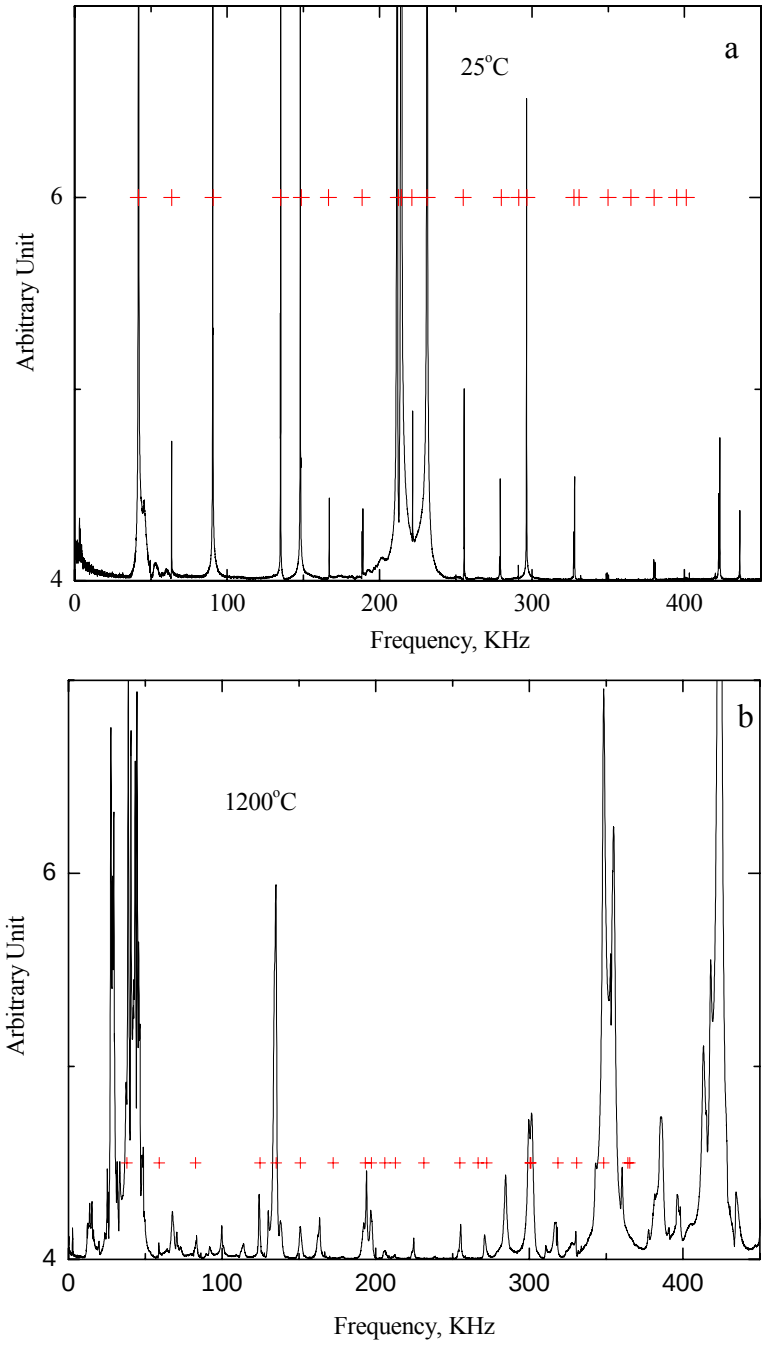

Fig. 50 Typical RUS spectra obtained for Ti_3SiC_2. a.) at 25 °C. b.) at 1200 °C. red crosses indicate the peak frequencies obtained by fitting the measured spectrum.

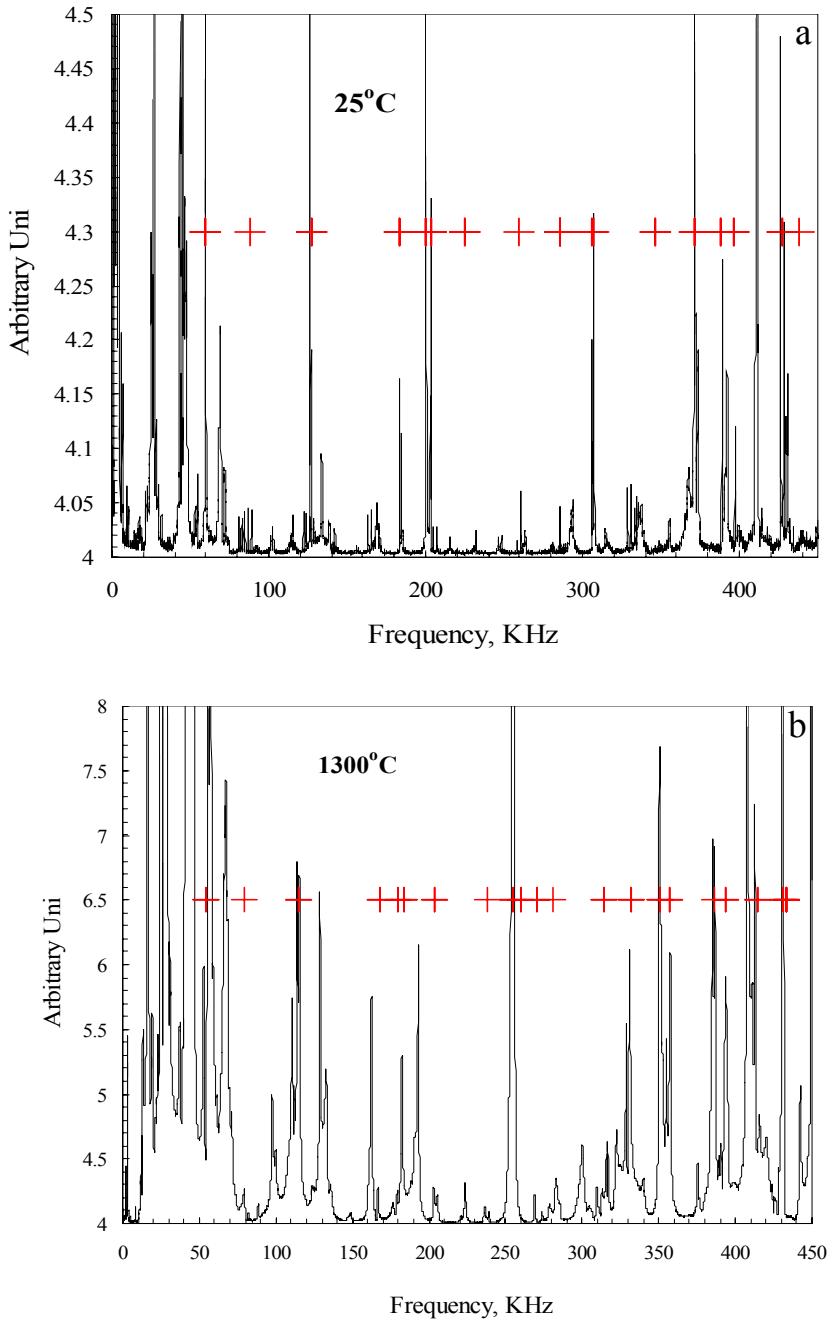

Fig. 51 Typical RUS spectra obtained for Ti_2AlC. a) at 25 °C; b) at 1300 °C. Red crosses indicate the peak frequencies obtained by fitting the measured spectra.

The temperature dependencies of Young's moduli of Ti_3SiC_2 and Ti_2AlC are plotted in Fig. 52 and summarized in Table6. The corresponding values for the shear moduli and Poisson's ratio are shown in Figs. 53 and 54, respectively. A least squares fit of the shear moduli results yields

$$\frac{G}{G_{RT}} = 1 - 1.56\text{x}10^{-4}(T - 298) \quad (16)$$

$$\frac{G}{G_{RT}} = 1 - 1.59\times10^{-4}(T - 298) \quad (17)$$

for Ti_3SiC_2 (Eq. 16) and Ti_2AlC (Eq. 17), respectively. where T is given in degree Kelvin. The temperature dependencies of the shear moduli of the two compounds are also comparable (Table 6).

The room temperature Young's and shear moduli of Ti_3SiC_2 obtained in this work are ≈1% higher than previous results [75, 76]. The slopes, $d(G/G_{RT})/dT$, however, are almost identical (Table 6), the changing rate of shear moduli as function of temperature is comparable at both low (150 – 250K) and high temperature (300 – 1489 K) region. But the changing rate of Young's moduli as function of temperature ($d(E/E_{RT})/dT$) is slightly higher in the high temperature region than at cryogenic temperatures. The Poisson's ratio is in good agreement (4%) between this work and previous work (Fig. 54)

The Debye temperature can also be estimated from the following expression:

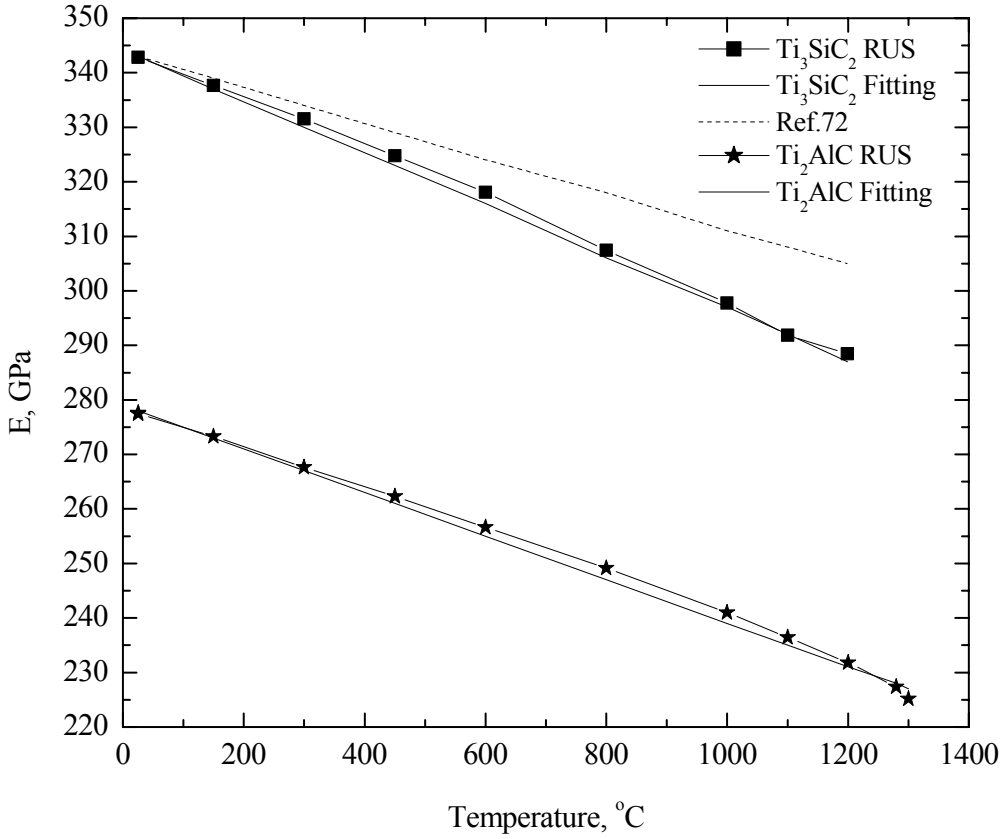

Fig. 52 Temperature dependence of Young's moduli, E, of Ti_3SiC_2 and Ti_2AlC.

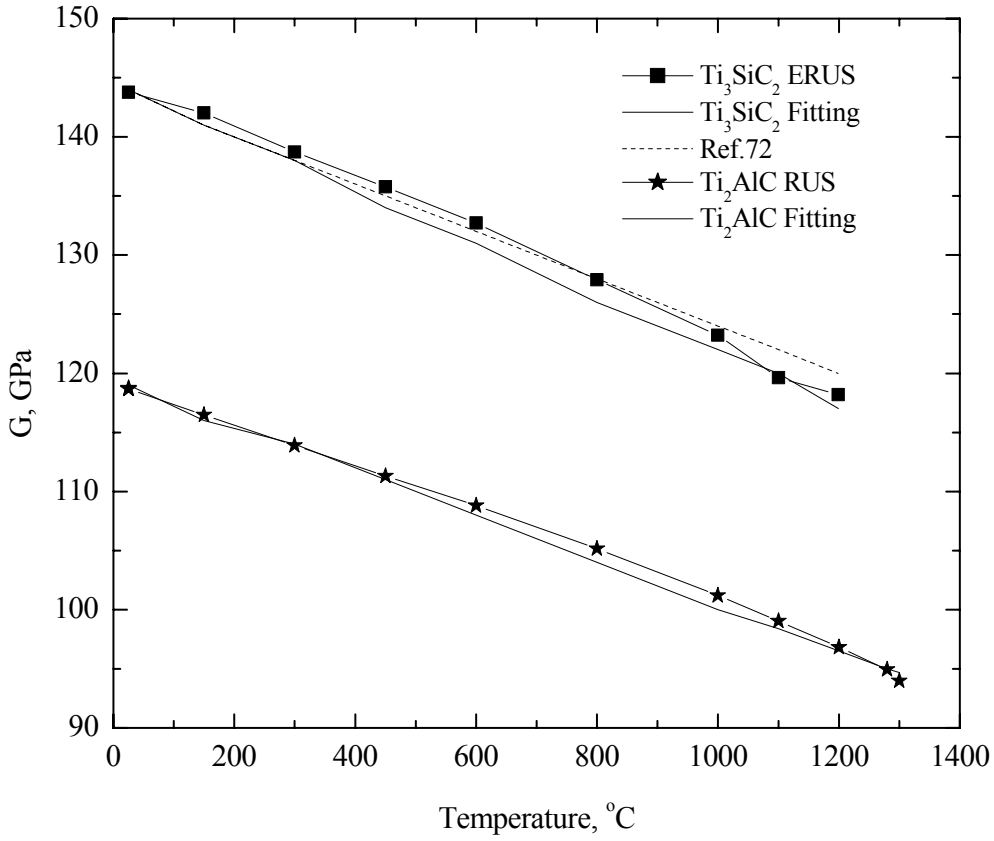

Fig. 53 Temperature dependence of shear moduli, G, of Ti_3SiC_2 and Ti_2AlC.

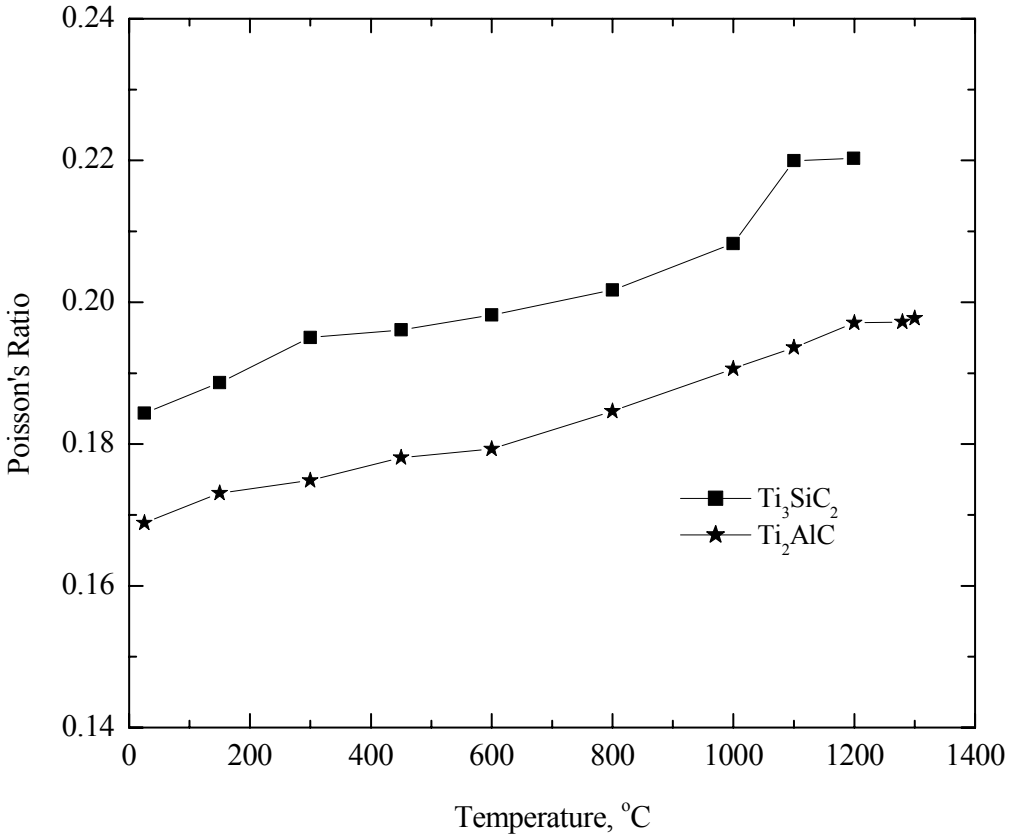

Fig. 54 Temperature dependence of Possion's ratio of Ti_3SiC_2 and Ti_2AlC.

Table 6. Summary of RUS results obtained in this work. Also listed are our previous results on Ti_3SiC_2.

	Ti_3SiC_2	Ti_2AlC
Room temperature Longitudinal velocity, m/s	9185[a] 9142 [75]	8590
Room temperature shear velocity, m/s	5670[a] 5613 [75]	5423
Room temperature mean velocity v_m, m/s	6255 [a] 6195 [75]	5967
Measure density, g/cm^3	4.5[a] 4.5[75]	4.0
Room temperature Young's modulus, GPa	342.8±0.8 [a] 339±2 [75]	277.6±0.7
Room temperature shear modulus, GPa	143.8±0.3 [a] 142±2 [75]	118.8±0.3
Room temperature bulk modulus, GPa	185.6±0.4 [a] 187 [75]	139.6±0.3
Poisson's ratio	0.1921±0.0004 [a] 0.200±0.007 [75]	0.1687±0.0004
***d*(E/E$_{RT}$)/*d*T, (K^{-1})**	-1.38x10^{-4} [a] -0.75x10^{-4} [72]	-1.44x10^{-5}
***d*(G/G$_{RT}$)/*d*T, (K^{-1})**	-1.56x10^{-4} [a] -1.4x10^{-4} [75]	-1.59x10^{-5}
Debye Temperature, K		
RUS	813 [a]	741
Acoustic	784[75]	-
Thermal	715[78]	-

a. This work, coarse-grained sample.

$$\theta_D = \left(\frac{h}{k}\right)\left(\frac{3\lambda\rho N_{AV}}{4\pi m}\right)^{1/3} V_m \qquad (17)$$

where h=Plank's constant, k=Boltzmann's constant, ρ=density, λ=number of atoms per molecule, N_{AV}=Avogadro's number, m=molecular weight, V_m= mean sound velocity defined as

$$V_m = \left[\frac{3(V_s V_l)^3}{2V_l^3 + V_s^3}\right]^{1/3} \qquad (18)$$

where V_l and V_s are the longitudinal and shear velocities, respectively. Based on the room temperature, the values of V_m, θ_D for Ti_3SiC_2 is calculated to be 813 K, which is about 4% higher than the previous value of 784 K [76]. Similarly, θ_D for Ti_2AlC is calculated to be 741K.

The Young's moduli of Ti_3SiC_2 from RUS are comparable with those obtained from mechanical tests at temperatures lower than 1000°C [10, 77]. At room temperature, the Young's moduli measured from tensile [10] and three-point bending [77] tests are close to 310 GPa. This value is roughly 10 % lower than the 342 GPa measured in this work. In compression tests (Ch. 2), the initial slope of unloading stress strain curve at room temperature is close to 320 GPa. At temperatures higher than 1000°C, the dramatically drop in moduli was reported in both tensile [10] and

three-point bending [77] tests. However, cyclic hardening was observed even at 1200^{o}C for both fine and coarse grained Ti_3SiC_2 in compressive tests (Figs. 41 and 42). The highest initial slope of loading curve is close to 270 GPa, which is ≈ 7% of the correspondent Young's moduli (288GPa) measured at 1200^{o}C in this work. We believe cyclic hardening is attributed to the refinement of microstructure due to formation of kink bands. Since at high temperature it is easy for the IKB to dissociate and form KBs, this will reduce the volume available for IKB and increase the initiation stress of IKB. Thus the material behaves cyclic hardening and the initial stress strain curve will approach linear elastic. It also indicates the dropping of moduli at high temperatures [10, 77] is most probably due to the significant increasing of anelastic deformation, not due to the dropping of the strength of atom bonding of the material.

5.3.2 Ultrasonic Attenuation.

One of the most attractive features of RUS is the ability to measure the ultrasonic attenuation, Q, of a resonance, defined by:

$$Q= \omega_o/ \Delta\omega. \qquad (19)$$

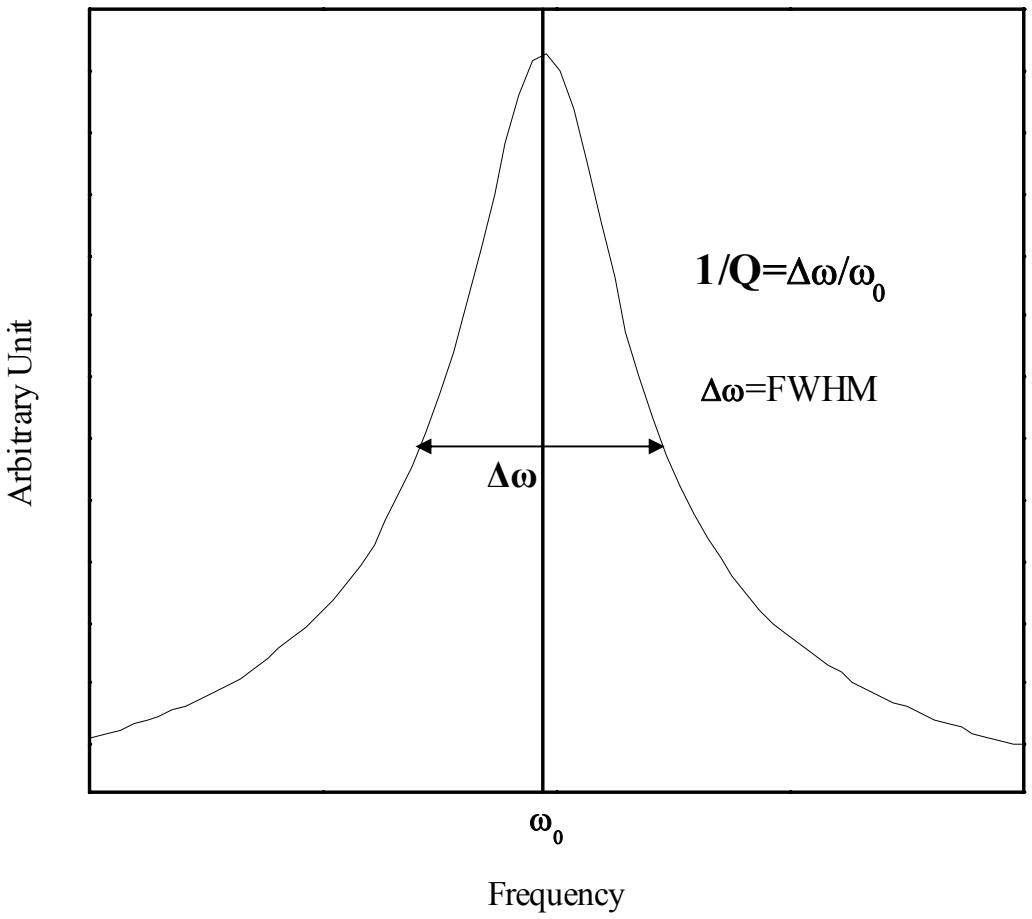

Fig. 55 Schematic depicting how to obtain 1/Q from ω_0 and $\Delta\omega$.

where ω_o is the center frequency and $\Delta\omega$ is the full width at half maximum (FWHM) of the correspondent resonance mode (Fig. 55). It is common practice to express the loss in terms of 1/Q. Thus we have, as a measure of the loss [74],

$$1/Q = \frac{\Delta\omega}{\omega_0} \tag{20}$$

5.3.2.1 Effect of pre-deformation

Figure 56 shows 1/Q dependence of frequency of virgin and pre-deformed (4 % of deformation at 1300^{o}C and 25MPa creep test) coarse-grained Ti_3SiC_2 samples at room temperature. It is obvious that 1/Q of the deformed Ti_3SiC_2 sample is significantly higher value than the virgin sample. This unique property implies the 1/Q of Ti_3SiC_2 depends on its deformation history. It is most probably due to the unique dislocation configuration of Ti_3SiC_2: Since only basal slip operates. Dislocation interactions, other than orthogonal, are difficult and unlikely to occur. Hence dislocations can move back and forth reversibly and extensively. Unlike metals there are no dislocation entanglement and the formation of dislocations forests causing the reduction of the free dislocation loop length during the plastic deformation. The deformation of Ti_3SiC_2 will not reduce the free dislocations loop length. On the contrary it will increase the dislocation density and the length of the loops. These dislocations can move like vibrating strings and dissipated ultrasonic energy. This process dramatically increases the 1/Q of deformed samples.

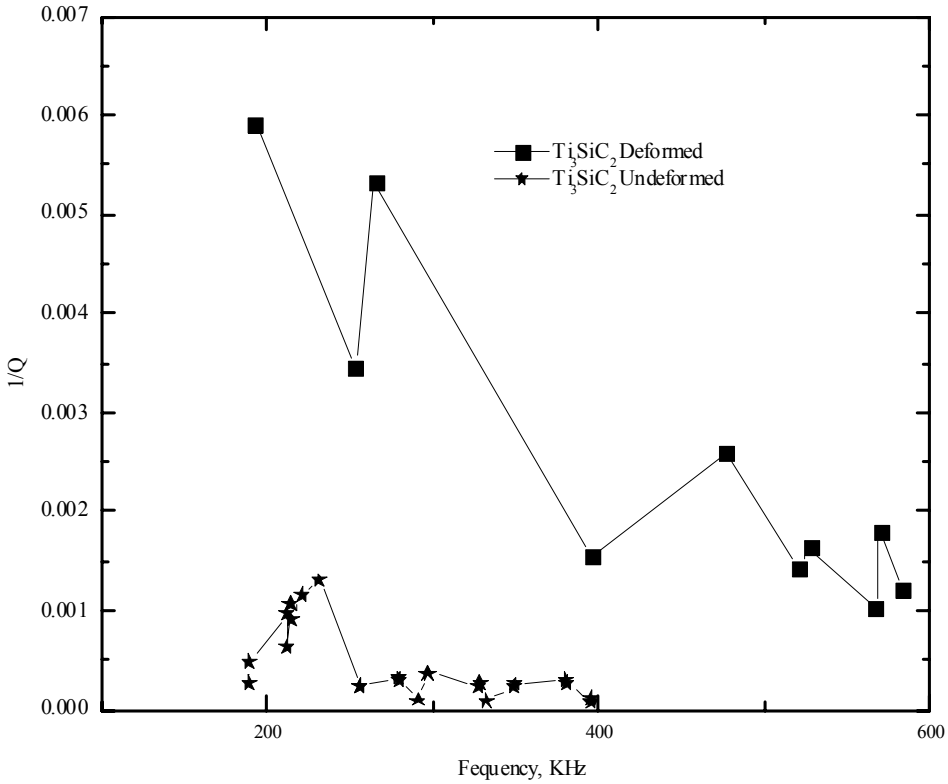

Fig. 56 1/Q as function of resonant frequencies at room temperature of deformed and undeformed Ti_3SiC_2 samples. The deformed sample was cut from a cylinder that was deformed 4 % at 1300 ^{o}C. The sample was a rectangular bar (16.5 x 9.8 x 1.2 mm). The undeformed sample was a disk shaped specimen (25.4 mm in diameter and 3.08 mm in thickness).

5.3.2.2 Effect of temperature

Figure 57 shows 1/Q as function of frequency at room and 1200 ^{o}C temperature of undeformed Ti_3SiC_2 sample. It clearly shows the value of 1/Q at 1200^{o}C is much higher than the value at room temperature of all the tested frequencies. Figure 58 shows the temperature dependence of 1/Q for measured resonance frequencies of Ti_3SiC_2 and Ti_2AlC. It clearly demonstrates that there is a transition of 1/Q around 1100 ^{o}C for both materials, above 1100 ^{o}C 1/Q increased dramatically. This is consistent with our compressive cyclic results in Ch. 4; The dissipated energy per cycle increases dramatically around 1100^{o}C for both the FG and CG Ti_3SiC_2 samples (Figs. 46a and 46b). The reason for this increase in 1/Q is not clear at this time and being further investigated.

5.3.2.3 Effect of drive level at 1200 ^{o}C

Two different resonance modes of coarse-grain Ti_3SiC_2 as function of drive level are shown in Figs 59a and 59b. There is one order of magnitude difference in drive levels between each resonant peak. The results clearly show:

i) The resonance frequency shifts left as the drive level increases. For example the resonant peak of 150 KHz (Fig. 59a) shifts about 400Hz when the drivel level is increased from 0.01 to 1; whereas the 255 KHz (Fig. 59b) peak shifts

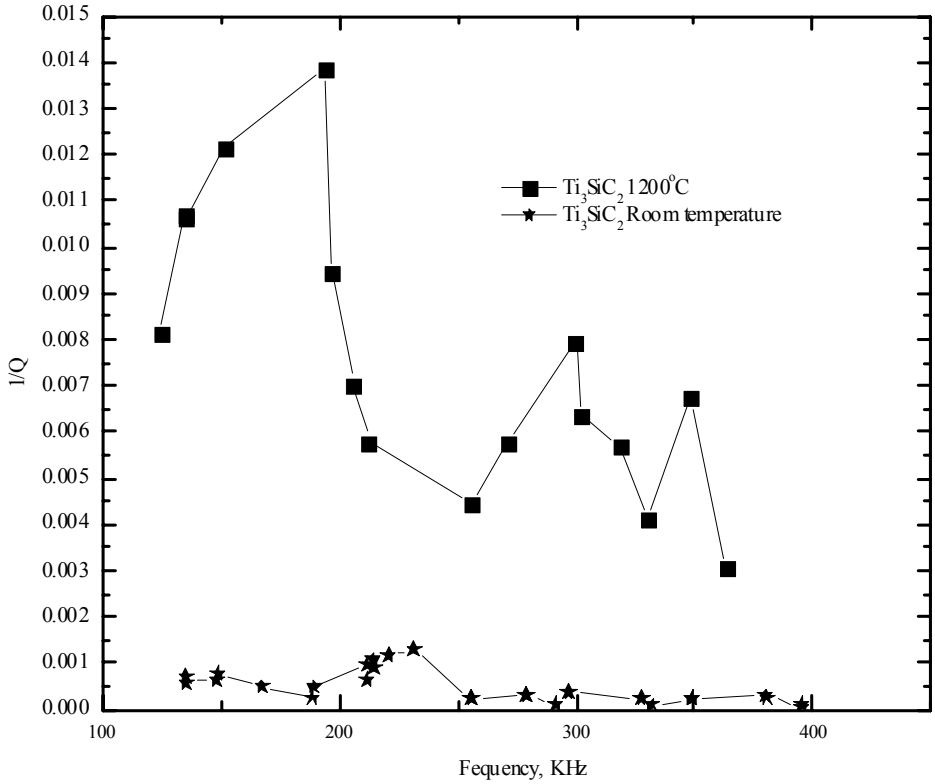

Fig. 57 1/Q as function of frequency at room and 1200 ^{o}C.

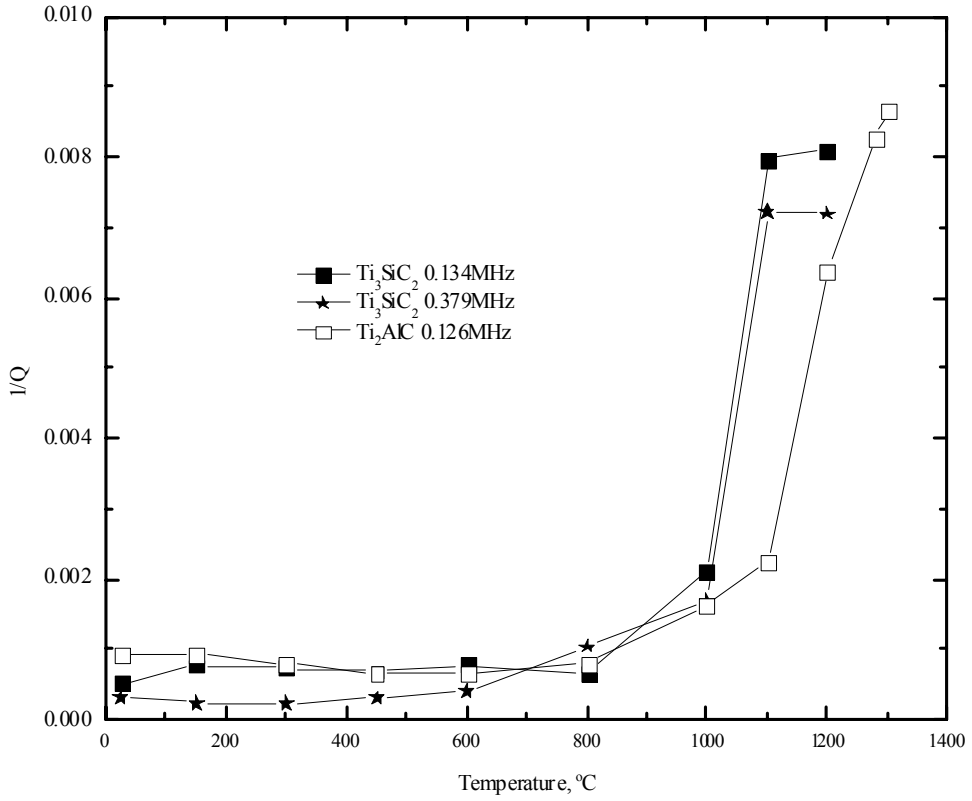

Fig. 58 Effect of temperature on 1/Q at 3 different resonant frequencies for Ti_3SiC_2 and Ti_2AlC.

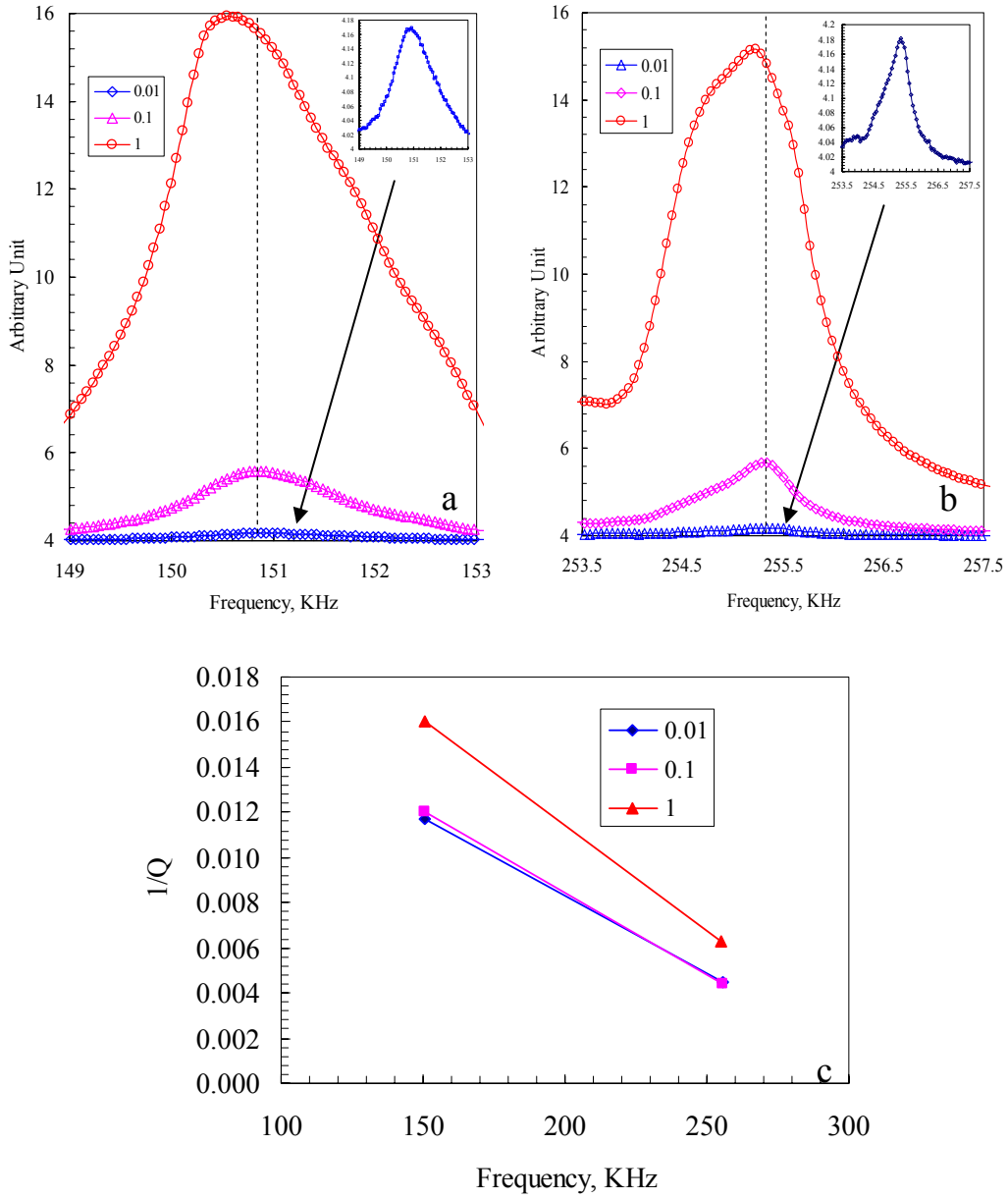

Fig. 59 Drive level (0.01, 0.1 and 1) effect on the resonance peak. a) 150 KHz resonance peak; b) 255 KHz resonance peak; c) 1/Q dependence of drive level of resonance peaks shown in a and b. The insets in a and b are the enlarged curves of the resonance peaks of the lowest drive level (0.01).

about 200 Hz for the same testing condition. From RUS theory, the left shift of same resonant mode implies a decrease in the stiffness of material.

ii) With increasing drive level, the resonant peaks of the same mode become broad (Figs. 59a and 59b), indicates that 1/Q increase as the drive level increases. (Fig. 59c).

5.4 Summary and Conclusions

The elastic properties of Ti_3SiC_2 and Ti_2AlC were measured by RUS in the 298-1573 K temperature range clearly shows both Young's and shear moduli decrease slowly with increasing temperature within the all testing temperature range. There is no dropping of moduli at high temperatures.

Ultrasonic attenuation is also investigated in this work. It shows the 1/Q is strongly influenced by the pre-deformation history, drive level and temperature. The pre-deformation dramatically increases the value of 1/Q. Also increasing the drive level will increase 1/Q at 1200 ^{o}C.

6. Summary, Conclusions and Future work

6.1 Summary and conclusions

In this thesis, we report our recent progress on the understanding of the mechanical response of KNE solids in general, and Ti_3SiC_2 in particular. A kinking-based model that explains the response of polycrystalline KNE samples to mechanical stress. The model also can account for many aspects of the deformation, i.e. nonlinear, hysteresis and discrete memory. The key to the model is the identification of a fully reversible hysteretic element – labeled incipient kink bands - comprised of near parallel dislocation walls that are strongly attractive. As long as the stress level is insufficient to sunder the IKBs the mechanical response is characterized by fully reversible hysteretic loops.

The microscale considerations based on Frank and Stroh's theory of kinking provide reasonable predictions for the volume fraction of the material transformed to IKBs in two different KNE solids. These estimates were obtained using two completely different strategies. The fact that these estimates were consistent with each other significantly strengthens our assertion that the nonlinear, fully reversible,

rate-independent, hysteretic, and shape-memory characteristics of KNE solids are indeed attributable to the formation and annihilation of incipient kink bands.

It has also been demonstrated that the elastic response of KNE solids can be captured by a simple phenomenological description that contains only three parameters. Of these three parameters, the values of two can be established from microscale considerations of the theory of kinking, and only one needs to be established using the measured stress-strain response in monotonic loading. Once these parameters are established, the model can provide reliable predictions of the stress-strain response of the KNE solids in any complex loading history comprising of arbitrary loading and unloading segments.

As a typical KNE solid, the mechanical behavior of Ti_3SiC_2 was systematically investigated through this work. Compressive creep and compressive properties of Ti_3SiC_2 were studied as function of temperature, grain size and strain rate.

Some of the more important conclusions drawn during this investigation are:

(i) A new class of materials, kinking nonlinear elastic (KNE) solids was identified and characterized in this work. The KNE solids include layered ternary carbides, nitrides, oxides and semiconductors, graphite and other layered phases, such as mica, present in NME solids.

(ii) The loading-unloading stress-strain curves of KNE solids in the elastic regime outline nonlinear, fully reversible, reproducible, rate-independent, closed hysteresis loops whose shape and extent of energy dissipated are strongly influenced by grain size with the energy dissipated being significantly larger in the coarse-grained material.

(iii) The microscale considerations based on Frank and Stroh theory of kinking provide reasonable predictions for the volume fraction of the material transformed to IKBs in three different KNE solids.

(iv) It has also been demonstrated that the elastic response of KNE solids can be captured by a simple phenomenological description that contains only three parameters. Of these three parameters, the values of two can be established from microscale considerations of the theory of kinking, and only one needs to be established using the measured stress-strain response in monotonic loading.

(v) At higher temperatures/stresses, the loops are open and the response becomes strain rate dependent. Cyclic hardening was observed even at 1200^{o}C for both FG and CG Ti_3SiC_2. This is attributed to the dissociation of the dislocation walls to cause significant hardening which occurs by the formation of deformation cells or polygonization.

(vi) The compressive creep of Ti_3SiC_2 occurs by a combination of plastic deformation and damage accumulation. The creep response is characterized by the presence of large internal stresses. The overall creep

response thus depends on the rate of generation and dissipation of these internal stresses.

(vii) The damping properties of KNE solids are strain amplitude and microstructure dependent.

(viii) The loss factors for Ti_3SiC_2 are higher than most woods and comparable to polypropylene and nylon at room temperature. Most important the damping properties of Ti_3SiC_2 are orders of magnitude higher than those of other structural ceramics and increase with increasing stress.

(ix) The loss factors for Ti_3SiC_2 are temperature dependent. Above 1000^oC the damping properties increase dramatically. And most important, this is also accompanied by good mechanical properties at high temperature, i.e. 1200^oC.

(x) At room temperature, the loss factors for Ti_3SiC_2 are stress, and deformation history dependent. At higher stress (in compression up to 1 GPa), the loss factors are almost an order of magnitude higher than the RUS results. Also the pre-deformed sample has higher value of loss factor than the virgin sample (Fig. 48).

6.2 Future work

Based on the results obtained, we believe the following issue should be systematically investigated in order to supplement the understanding developed thus far on the mechanical behavior of KNE solids.

(i) At this stage, the exactly physical mechanism how the IKB are nucleated remains elusive. More theoretical and experimental work is needed.

(ii) The IKB model presented in this work is a two-dimensional model. It would be very helpful to understand this unique phenomenon by developing a three-dimensional model.

(iii) In our constitutive model we assume a uniform microstructure, this assumption works very well on narrowly distributed microstructure sample, but not on microstructure with wide distribution of grain sizes sample. More work need to be done here.

(iv) We believe dislocation pileups (arrays) play an important role; at the very least they probably trigger the kinking. Other than that, our results do not permit further speculation at this time; we are currently exploring the problem.

(v) It is hereby acknowledged that the high temperature atomistic nature of the plastic and anelastic parts of the deformation are not

clear at this time. More work is needed to better understand physical original of these properties.

List of References

1. Curry, L.M., Hamister, V.C. and McPherson, H.G. Proc. Int. Conf. On the Peaceful Use of Atomic Energy, Vol. 8, UNO, Geneva (1955).

2. Davidson, H. Losty, H.H.W. and Ross, A.M. Proc. First SCI Conference on Industrial Carbons and Graphites, SCI, London, p.551 (1958).

3. Losty H.H.W., Sc. B., and Orchard J.S. The Strength of Graphite. Proc. Fifth Biennial Carbon Conference; 1963; 1p; 519-532.

4. R. A. Guyer & P. A. Johnson, "Nonlinear Mesoscopic Elasticity: Evidence for a New Class of Solids", Physics Today, April (1999).

5. R. A. Guyer, K. R. McCall & G. N. Boitnott, "Hystersis, Discrete Memory and Non-linear Wave Propagation in Rock: A New Paradigm", Phys. Rev. Letters, 74, 3491 (1995).

6. D. J. Holcomb, "Memory, Relaxation and Microfracturing in Dilatant Rock", J. Geophys. Res. 86, 6235 (1981).

7. T. B. Anderson, "Kink Bands and Related Geologic Structures", Nature, 202, 272 (1964).

8. M. S. Paterson & L. E. Weiss, "Experimental Folding in Rocks", Nature, 195, 1046 (1962).

9. M. S. Paterson & L. E. Weiss, "Experimental Deformation and Folding in Phyllite", Geolg. Soc. Am. Bull., 77, 343 (1966).

10. M. Radovic, M. W. Barsoum, T. El-Raghy, S. Wiederhorn, W. Luecke, Effect of temperature, strain rate and grain size on the mechanical response of Ti_3SiC_2 in tension. *Acta Mater.* **50** 1297-1306 (2002).

11. Barsoum MW, Zhen T, Kalidindi S, Radovic M, Murugaiah A. Dislocation based fully reversible compression of Ti_3SiC_2 up to 1 GPa. Nature Materials 2003; 2: 107-111.

12. Murugaiah A, Barsoum MW, Kalidindi SR, Zhen T. Spherical nanoindentations in Ti_3SiC_2. Submitted for publication in J. of Mat. Res.

13. Barsoum MW, Murugaiah A, Kalidindi SR, Zhen T. Kinking Nonlinear Elastic Solids, Nanoindentations and Geology. Submitted for publication.

14. Barsoum MW, Murugaiah A, Kalidindi SR, Zhen T. and Gogotsi Y. “Nanoindentations and Kink Bands in Single Crystal Graphite”, Submitted for publication to Carbon.

15. E. Orowan, Nature, “A Type of Plastic Deformation New In Metals”, 149, 463-464 (1942).

16. Kelly BT. Physics of Graphite. Applied Science Publishers, London, 1981.

17. Freise, E.J. and Kelly, A. Phil.Mag., 8, 1519, 1963.

18. Eshelby, J.D. Phil. Mag., 40, 503, 1949.

19. Friedel, J. Phil. Mag., 44, 444, 1953.

20. Mott, N. F. Phil. Mag., 43, 1151, 1952.

21. Kelly, B. T. Phil. Mag., 9, 721, 1964.

22. Reynolds, W. N. Phil. Mag., 11, 357, 1965.

23. Jenkins, G. M. Brit. J. Applied Physics, 13, 30, 1962.

24. Jenkins, G. M., Williamson, G. K. and Barnett, J. T. Carbon, 3, 1, 1965.

25. Woolley, R. L. Phil. Mag., 11, 799, 1965.

26. Hesketh, R. V. J. Applied Physics, 35, 3604, 1964.

27. A. Meike, Am. Mineral. **74**, 780 (1989).

28. T. B. Anderson, Nature, **202**, 272 (1964).

29. F. A. Donath, Am. Geophys. Union Trans., **45**, 103 (1964).

30. M. S. Paterson & L. E. Weiss, Nature, **195**, 1046 (1962).

31. M. S. Paterson & L. E. Weiss, Geolg. Soc. Am. Bull., **77**, 343 (1966).

32. C .J. Gilbert, D.R. Bloyer, M.W. Barsoum, T. El-Raghy, A.P. Tomsia, R.O. Ritchie, Fatigue-crack growth and fracture properties of coarse and fine-grained Ti_3SiC_2 , Scripta Mater. 42 (2000) 761–767.

33. K . Shirato, D. Chen, M.W. Barsoum, T. El-Raghy, R.O. Ritchie, High-temp cyclic fatigue-crack growth in monolithic Ti_3SiC_2 , J. Am. Ceram. Soc. (in press).

34. M. W. Barsoum, T. El-Raghy, Synthesis and characterization of a remarkable ceramic: Ti_3SiC_2. *J. Amer. Cer. Soc.* **79**, [7] 1953-56 (1996).

35. L. Farber, M.W. Barsoum, A. Zavaliangos, T. El-Raghy, Dislocations and stacking faults in Ti_3SiC_2, J. Am. Ceram. Soc. 84 (1998) 1677–1681.

36. L. Farber, I. Levin and M. W. Barsoum, "HRTEM Study of a Low-Angle Boundary in Plastically Deformed Ti_3SiC_2", Phil. Mag. Letters., **79**, 4103–4112. (1999).

37. M. W. Barsoum, The $M_{N+1}AX_N$ phases: A new class of solids: thermodynamically stable nanolaminates. *Prog. Sol. State Chem.* **28,** 201-281 (2000).

38. M. W. Barsoum, L. Farber, T. El-Raghy, Dislocations, kink banks and room temperature plasticity of Ti_3SiC_2. *Met. Mat. Trans.* **30A,** 1727-1738 (1999). **21a**

39. M. W. Barsoum, T. El-Raghy, Room temperature ductile carbides. *Met. Mater. Trans.* **30A,** 363-369 (1999). **22a**

40. T. El-Raghy, M. W. Barsoum, Processing and mechanical properties of Ti_3SiC_2: part I: reaction path and microstructure evolution. *J. Amer. Cer. Soc.* **82,** 2849-54 (1999).

41. T. El-Raghy, M. W. Barsoum, A. Zavaliangos, S. R. Kalidindi,, Processing and mechanical properties of Ti_3SiC_2: II, effect of grain size and deformation temperature. *J. Amer. Cer. Soc.* **82,** 2855-2860. **24a.**

42. M.W. Barsoum, T. El-Raghy, and C.J. Rawn, *J. Electrochem.Soc*., 1997, **144**, 2508

43. M. W. Barsoum, "The $M_{N+1}AX_N$ Phases: A New Class of Solids: Thermodynamically Stable Nanolaminates", Prog. Sol. State Chem., **28,** 201-281 (2000).

44. R. Von Mises, Z. Ang. Math. Meth. 8, 161 (1928).

45. G. I. Taylor, J. Inst. Met. 62, 307 (1938).

46. J–F. Li, W. Pan, F. Sato and R. Watanabe, “Mechanical Properties of Polycrystalline Ti_3SiC_2 at Ambient and Elevated Temperatures”, Acta. Mater., **49**, 937, (2001).

47. E. Orowan, Nature, “A Type of Plastic Deformation New In Metals”, 149, 463-464 (1942).

48. F.C. Frank, A.N. Stroh, “On the theory of kinking”, Proc. Phys. Soc., 65, 811-821 (1952).

49. J. B. Hess and C. S. Barrett, “Structure and Nature of Kink Bands in Zinc”, Trans. AIME, 185, 599-606 (1949).

50. A. Ganguly, T. Zhen and M. W. Barsoum, “Synthesis and Mechanical Properties of Ti_3GeC_2 and $Ti_3(Si_xGe_{1-x})C_2$ (x = 0.5, 0.75) Solid Solutions” *J. Alloys and compounds*, 2004

51. G. H. Beall, Ann. Rev. Mater. Sci, **22,** 91 (1992).

52. A. S. Nowick and B. S. Berry, Anelastic Relaxation in Crystalline Solids, Academic Press, NY 1972.

53. Mechanical Spectroscopy Q^{-1} 2001. Eds. R. Schaller, G. Fantozzi and G. Gremaud, Trans. Tech. Publications, Zurich, Switzerland.

54. J. M. Roberts and N. Brown, “Low Frequency Friction in Zinc Single Crystals”, Acta. Metall, **10**, 430-441 (1962).

55. J. Washburn and E. R. Roper, “Kinking in Zn Single Crystal Tension Specimens”, J. of Metals, 1076-1078 (1952).

56. Barsoum MW, Radovic M, Finkel P, El-Raghy T. Ti_3SiC_2 and Ice Appl. Phy, Lett. **79**, 479 (2001).

57. M. Radovic, M. W. Barsoum, T. El-Raghy, S. Wiederhorn, Tensile creep of fine-grained (3-5 μm) Ti_3SiC_2 in the 1000-1200 °C temperature range. *Acta Mater.* **49**, 4103-4112 (2001).

58. M. Radovic, M. W. Barsoum, T. El-Raghy, S. Wiederhorn, Tensile creep of coarse-grained Ti_3SiC_2 in the 1000-1200 °C temperature range. *J. Alloys and compounds*, 361, 299-312, 2003

59. D .L. Goldsby, D.L. Kohlstedt, Superplastic deformation of ice: experimental observations, J. Geophys. Res. 106 (2001) 11017– 11030.

60. Radovic M, Barsoum MW, El-Raghy T, Seidensticker J, Wiederhorn s. Tensile properties of Ti_3SiC_2 in the 25-1300 ^oC temperature range. Acta Mater. 2000;48:453-59.

61. Dowling NE. Mechanical behavior of metals. 2nd edition, Prentice Hall, Upper Saddle River NJ 1998.

62. Skrzypel JJ, Hetnarski RB. Plasticity and creep: Theory, examples, and problems, CRC Press, Boca Raton FL, 2000

63. P. Duval, M. F. Ashby and I. Anderman, "Rate Controlling Process in Creep of Polycrystalline Ice", J. Phys. Chem, **87** 4066-4076 (1983).

64. J. Weiss and E. M. Schulson, Philos. Mag. A **80**, 279, 2000.

65. R. Schaller in "High Damping Materials", in Mechanical Spectroscopy Q^{-1} 2001. p. 621-631Eds. R. Schaller, G. Fantozzi and G. Gremaud, Trans. Tech. Publications, 2001, Zurich, Switzerland.

66. Science and Technology of Rubber, Eds. J. Mark, B. Erman and F. Eirich, 2nd ed., Academic Press, NY, 1994

67. H. Nowotny, Struktuchemie einiger verbindungen der ubergangsmetalle mit den elementen C, Si, Ge, Sn. Prog. Solid State Chem., H. Reiss, Ed., p.27, (1970).

68. M. A. Pietzka, J. C. Schuster, Summary of constitution data of the system Al-C-Ti. J. Phase Equilibria 15, 392 (1994).

69. C. J. Rawn et al, Structure of Ti_4AlN_{3-x}- a layered $M_{n+1}AX_n$ Nitride. Mater. Res. Bull. 35, 1785 (2000).

70. T. Zhen, M. W. Barsoum, S. R. Kalidindi, Compressive Creep of Fine and Coarse-Grained T_3SiC_2 in Air in the 1100 to 1300 °C Temperature Range, in preparation.

71. T. Zhen, M. W. Barsoum, S. R. Kalidindi, On Modeling the Constitutive Response of Kinking Nonlinear Elastic Solids, in preparation.

72. T. Zhen, M. W. Barsoum, M. Radovic, Elastic Properties of Ti3SiC2 and Ti2AlC at 298-1573K Temperature Range, in preparation.

73. A. Migliori and J. L. Sarrao, Resonant Ultrasound Spectroscopy: Applications to Physics, Materials Measurements and Nondestructive Evaluation, John Wiley and Sons, New York, (1997)

74. Migliori, A. J.L. Sarrao, W. M. Visscher, T.M. Bell, M. Lei, et al. Resonant ultrasound spectroscopic techniques for measurements of the elastic moduli of solid. Physica B, 183, 1-24 (1993).

75. P. Finkel, M.W. Barsoum, T. El-Raghy, Low temperature dependencies of the elastic properties of Ti_4AlN_3, $Ti_3Al_{1.1}C_{1.8}$, and Ti_3SiC_2. J. Appl. Phys., 87, 1701(2000).

76. P. Finkel, M.W. Barsoum, T. El-Raghy, Low temperature dependence of the elastic properties of Ti_3SiC_2. J. Appl. Phys., 85, 7123(1999).

77. Y.W. Bao, Y.C. Zhou, Evaluating high-temperature modulus and elastic recovery of Ti_3SiC_2 and Ti_3AlC_2 ceramics, Materials Letters, 57, 4018 (2003).

78. J.C.Ho, H.H. Hirano, M.W.Barsoum and T. Tl-Raghy, J. Appl. Phys. 86, 3609 (1999)

79. M. F. Ashby, On the engineering properties materials, Acta. Metal. 37 (1989), p.1273-1293.

80. P. Scherrer, Göttinger Nachrichten, **2** (1918), S. 98.

Vita

TIEJUN ZHEN

DOB: 09/20/1971
Citizenship: P.R. China

Education

Ph.D. in Material Science & Engineering, Drexel University, Philadelphia, PA, June 2004.
M.Sc. in Mechanical Engineering, major in Solid Mechanics, Beijing University of Technology, Beijing, July 1998.
B.Sc. in Material engineering, Beijing University of Technology, Beijing, July 1994.

Experience

Research Assistant, Dept. of Materials Engineering Drexel University, Philadelphia, PA, April 2001- present.
Teaching Assistant, Dept. of Materials Engineering Drexel University, Philadelphia, PA, September 2000- April 2001.

Publications

Five journal papers.